UNIVERSIDADE FEDERAL DO CEARÁ
CENTRO DE TECNOLOGIA
DEPARTAMENTO DE ENGENHARIA DE TELEINFORMÁTICA
PROGRAMA DE PÓS-GRADUAÇÃO EM ENGENHARIA DE TELEINFORMÁTICA

BRUNO SOKAL

TENSOR-BASED SIGNAL PROCESSING WITH APPLICATIONS TO MIMO-OFDM SYSTEMS AND INTELLIGENT REFLECTING SURFACES

FORTALEZA
2022

BRUNO SOKAL

TENSOR-BASED SIGNAL PROCESSING WITH APPLICATIONS TO MIMO-OFDM SYSTEMS AND INTELLIGENT REFLECTING SURFACES

Tese apresentada ao Curso de Doutorado em Engenharia de Teleinformática da Universidade Federal do Ceará, como parte dos requisitos para obtenção do Título de Doutor em Engenharia de Teleinformática. Área de concentração: Sinais e Sistemas

Orientador: Prof. Dr. André Lima Ferrer de Almeida

Coorientador: Prof. Dr-Ing. Martin Haardt

FORTALEZA
2022

Dados Internacionais de Catalogação na Publicação
Universidade Federal do Ceará
Sistema de Bibliotecas
Gerada automaticamente pelo módulo Catalog, mediante os dados fornecidos pelo(a) autor(a)

S1t Sokal, Bruno.
Tensor-Based Signal Processing with Applications to MIMO-OFDM Systems and Intelligent Reflecting Surfaces / Bruno Sokal. – 2022.
123 f. : il. color.

Tese (doutorado) – Universidade Federal do Ceará, Centro de Tecnologia, Programa de Pós-Graduação em Engenharia de Teleinformática, Fortaleza, 2022.
Orientação: Prof. Dr. André Lima Férrer de Almeida.
Coorientação: Prof. Dr. Martin Haardt.

1. sistemas MIMO-OFDM. 2. IRS. 3. modelagem tensorial. 4. 5G. 5. PARAFAC. I. Título.
CDD 621.38

BRUNO SOKAL

TENSOR-BASED SIGNAL PROCESSING WITH APPLICATIONS TO MIMO-OFDM SYSTEMS AND INTELLIGENT REFLECTING SURFACES

Thesis presented to the Graduate Program in Teleinformatics Engineering of the Federal University of Ceará as a partial requisite to obtain the Ph.D. degree in Teleinformatics Engineering. Concentration Area: Signals and Systems.

Aproved on: 26/08/2022.

EXAMINING COMMITTEE

Prof. Dr. André Lima Ferrer de Almeida (Advisor)
Federal University of Ceará, Fortaleza, Brazil

Prof. Dr-Ing. Martin Haardt (Co-Advisor)
Technische Universität Ilmenau, Ilmenau, Germany

Prof. Dr. Walter da Cruz Freitas Júnior
Federal University of Ceará, Fortaleza, Brazil

Prof. Dr. Rémy Boyer
Université de Lille, Lille, France

Prof. Dr.-Ing. Gerald Schuller
Ilmenau University of Technology, Ilmenau, Germany

Prof. Dr.-Ing. Giovanni Del Galdo
Ilmenau University of Technology, Ilmenau, Germany

ACKNOWLEDGEMENTS

First of all, I would like to thank my advisor Prof. Dr. André Lima Férrer de Almeida which I as a friend. Thank you André for all the constructive suggestions, and comments a council over these years. I also would like to thank Prof. Dr.-Ing Martin Haardt for co-advising my Ph.D. and for all comments and suggestions which improve the quality and presentation of this work.

I also dedicate this document to my colleagues and friends from GTEL, Lucas, Alexandre, Asim, Gilderlan and Paulo, and my friends from the CRL, Khaled, Liana, Sepideh, and Damir. Thank you all for your support and the nice time we had on our discussions.

Special thanks to my family who without their support this document would not be possible.

Finally, I acknowledge the technical and financial support from Coordenação de Aperfeiçoamento de Pessoal de Nível Superior (CAPES)-Brazil, under finance code 001, and Ericsson Research, Sweden, and Ericsson Innovation Center, Brazil, under UFC.47 Technical Cooperation Contract Ericsson/UFC.

RESUMO

O uso de técnicas de álgebra tensorial em processamento de sinais têm crescido nas últimas décadas. Em aplicações como, processamento de imagens, processamento de sinais biomédicos, processamento de sinais em arranjos de sensores, e comunicações em geral, técnicas de processamento baseadas em tensores têm sido amplamente empregadas para problemas de estimação, recuperação, e classificação de sinais. Uma das principais razões de se usar técnicas baseadas em tensores para processamento de sinais é devido à sua capacidade de explorar efetivamente a estrutura multi dimensional dos sinais e também as propriedades de unicidade relativas às decomposições tensoriais. Por exemplo, em sistemas de comunicações sem-fio, um sinal possui diversas dimensões, como espaço (antenas), tempo, frequência, polarização, feixe, etc. Esta tese é divida em duas partes. Na primeira parte propomos a aplicação de algoritmos baseados em tensores para sistemas MIMO-OFDM (do inglês, multiple-input multiple-output orthogonal frequency division multiplex) considerando imperfeições do sistema como ruídos de fase. Mais especificamente, nós propomos um receptor de dois estágios, baseado em tensores, para a estimação conjunta de canal, ruído de fase, e dados. No primeiro estágio, nós mostramos que o sinal recebido nas portadoras piloto pode ser escrito como um modelo tensorial PARAFAC de terceira ordem. A partir deste modelo, é proposto dois algoritmos para estimação do ruído de fase e do canal nas portadoras piloto. No segundo estágio do receptor proposto os dados transmitidos são estimados. Para tal, propomos um receptor ZF (do inglês zero forcing) o qual capitaliza a estrutura tensorial do sinal recebido nas portadoras de dados usando o operador proposto SKP (do inglês selective Kronecker product). Resultados de simulação mostram que o receptor proposto atinge um desempenho superior em taxa de error de símbolo (SER, do inglês symbol error rate) e também NMSE (do inglês normalized mean squared error). Na segunda parte desta tese, focamos na aplicação da modelagem tensorial em sistemas MIMO assistidos por uma IRS (do inglês intelligent reconfigurable surface) para reduzir o gargalo de sinalização de controle. Para isto, uma aproximação de baixo rank é proposta para o vetor de fase ótimo de uma IRS. A principal ideia é representar o vetor de fase ótimo da IRS, em que pode possuir centenas ou milhares de elementos, usando um modelo tensorial de baixo rank, o qual é definido como uma combinação de Kronecker, com número de fatores, tamanho de cada fator, número de componentes pré-definidos. Resultados de simulação mostram que o modelo proposto reduz drasticamente a sinalização de controle requerida (em bits). Também é mostrado que, o modelo proposto é especialmente atrativo nos casos em que as componentes de linha de visada, dos canais de comunicação envolvidos, são consideravelmente fortes.

Keywords: 5G, 6G, sistemas MIMO-OFDM, estimação de ruído de fase, produto de Kronecker seletivo (SKP), IRS, sinalização de controle, aproximação de baixo rank, modelagem tensorial, decomposição PARAFAC, decomposição Tucker.

ABSTRACT

The use of tensor algebra techniques in signal processing has been growing over the last two decades. Applications like image processing, biomedical signal processing, radar, machine/deep learning, and communications in general, largely employ tensor-based techniques for recovery, estimating, and classifying signals. One of the main reasons for using tensor signal processing is the exploitation of the multidimensional structure of signals, while benefiting from the uniqueness properties of tensor decomposition. For example, in wireless communications, the signals can have several ”dimensions", e.g., space, time, frequency, polarization, beamspace, etc.. This thesis is divided into two parts, first, in the application of a tensor-based algorithm in multiple-input multiple-output (MIMO)-orthogonal frequency division multiplexing (OFDM) systems with the presence of phase-noise impairments. In this first part, we propose a two-stage tensor-based receiver for a joint channel, phase-noise, and data estimation in MIMO-OFDM systems. In the first stage, we show that the received signal at the pilot subcarriers can be modeled as a third-order PARAFAC tensor. Based on this model, we propose two algorithms for channel and phase-noise estimation at the pilot subcarriers. The second stage consists of data estimation, for which we propose a ZF receiver that capitalizes on the tensor structure of the received signal at the data subcarriers using the proposed SKP operator. Numerical simulations show that the proposed receivers achieves an improved performance compared to the state-of-art receivers in terms of symbol error rate (SER) and normalized mean square error (NMSE) of the estimated channel and phase-noise matrices. The second part of this thesis focuses on the application of tensor modeling to reduce the control signaling overhead in future wireless systems aided by intelligent reflecting surfaces (IRS). To this end, we propose a low-rank approximation of the near-optimal IRS phase-shifts, which would incur prohibitively high communication overhead on the BS-IRS controller links. The key idea is to represent the potentially large IRS phase-shift vector using a low-rank tensor model. This is achieved by factorizing a *tensorized* version of the IRS phase-shift vector, where each component is modeled as the Kronecker product of a predefined number of factors of smaller sizes, which can be obtained *via* tensor decomposition algorithms. We show that the proposed low-rank models drastically reduce the required feedback requirements associated with the BS-IRS control links. Simulation results indicate that the proposed method is especially attractive in scenarios with a strong line of sight component, in which case nearly the same spectral efficiency is reached as in the cases with near-optimal phase-shifts, but with a drastically reduced communication overhead.

Keywords: 5G, 6G, MIMO-OFDM systems, phase-noise estimation, selective Kronecker products, IRS, control signaling, low-rank approximation, tensor modeling, PARAFAC decomposition, Tucker decomposition.

ZUSAMMENFASSUNG

Der Einsatz von Tensor-Algebra-Techniken in der Signalverarbeitung hat in den letzten zwei Jahrzehnten zugenommen. Anwendungen wie Bildverarbeitung, biomedizinische Signalverarbeitung, radar, maschinelles Lernen, deep Learning und Kommunikation im Allgemeinen verwenden weitgehend tensorbasierte Verarbeitungstechniken zur Wiederherstellung, Schätzung und Klassifizierung von Signalen. Einer der Hauptgründe für den Einsatz der Tensorsignalverarbeitung ist die Ausnutzung der mehrdimensionalen Struktur von Signalen, wobei die Einzigartigkeitseigenschaften der Tensor-Zerlegung profitieren. Bei der drahtlosen Kommunikation beispielsweise können die Signale mehrere "Dimensionen" haben, wie Raum, Zeit, Frequenz, Polarisation, usw. Diese Arbeit ist in zwei Teile gegliedert. Im ersten Teil betrachten wir die Anwendung von Tensor-basierten Algorithmen für multiple-input multiple-output (MIMO) orthogonal frequency division multiplexing (OFDM) Systeme unter Berücksichtigung von Vorhandensein von Phasenrauschenstörungen. In diesem Teil schlagen wir einen zweistufigen tensorbasierten Empfänger für eine gemeinsame Kanal-, Phasenrausch- und Datenschätzung in MIMO-OFDM-Systemen vor. In der ersten Stufe zeigen wir, dass das empfangene Signal auf den Pilotunterträgern als PARAFAC-Tensor dritter Ordnung modelliert werden kann. Auf der Grundlage dieses Modells werden zwei Algorithmen für die Schätzung der Phasen- und Kanalrauschen in den Pilotton vorgeschlagen. In der zweiten Stufe werden die übertragenen Daten geschätzt. Zu diesem Zweck schlagen wir einen Zero Forcing (ZF)-Empfänger vor, der sich die Tensorstruktur des empfangenen Signals auf den Datenträgern zunutze macht, indem er den vorgeschlagenen selektiven Kronecker-Produkt-Operators (SKP) kapitalisiert. Die Simulationsergebnisse zeigen, dass der vorgeschlagene Empfänger sowohl bei der Symbolfehler rate als auch beim normalisierten mittleren quadratischen Fehler des geschätzten Kanal- und Phasenrauschmatrizen eine bessere Leistung im Vergleich zum Stand der Technik erzielt. Der zweite Teil dieser Arbeit befasst sich mit der Anwendung der Tensormodellierung zur Reduzierung des Kontrollsignalisierungsoverhead in zukünftigen drahtlosen Systemen, die durch intelligent reconfigurable surfaces (IRSs) unterstützt werden. Zu diesem Zweck schlagen wir eine Annäherung an die nahezu optimalen IRS-Phasenverschiebungen vor, die sonst einen prohibitiv hohen Kommunikationsoverhead auf den BS-IRS-Kontrollverbindungen verursachen würde. Die Hauptidee besteht darin, den optimalen Phasenvektor des IRSs, der Hunderte oder Tausende von Elementen haben kann, durch ein Tensormodell mit niedrigem Rang darzustellen. Dies wird erreicht durch Faktorisierung einer tensorisierten Version des IRS-Phasenverschiebungsvektors, wobei jede Komponente als Kronecker-Produkt einer vordefinierten Anzahl von Faktoren mit kleinerer Größe modelliert wird, die durch Tensor Zerlegungsalgorithmen erhaltet werden können. Wir zeigen, dass die vorgeschlagenen Low-Rank-Modelle die Rückkopplungsanforderungen für die BS-IRS-Kontrollverbindungen drastisch reduzieren. Die Simulationsergebnisse zeigen, dass die vorgeschlagene Methode besonders in Szenarien mit einer starken Sichtverbindung attraktiv sind. In diesem Fall wird fast die gleiche spektrale Effizienz erreicht wie in den Fällen mit nahezu

optimalen Phasenverschiebungen, jedoch mit einem drastisch reduzierten Kommunikations-Overhead.

Keywords: 5G, 6G, MIMO-OFDM-Systeme, Phasenrauschschätzung, selektives Kronecker-Produkt, IRS, Kontrollsignalisierung, Low-Rank-Approximation, Tensor-Modellierung, PARAFAC-Zerlegung, Tucker-Zerlegung.

LIST OF FIGURES

LIST OF TABLES

LIST OF ABBREVIATIONS AND ACRONYMS

3G	third-generation
3GPP	3rd Generation Partnership Project
4G	fourth-generation
5G	fifth-generation
5G-RANGE	Remote area Access Network for 5th GEneration
6G	sixth-generation
AF	amplify-and-forward
ALS	alternating least squares
AOA	angle of arrival
AOD	angle of departure
AP	access point
AWGN	additive white Gaussian noise
B5G	beyond fifth-generation
BALS	bilinear alternating least squares
BS	base station
CFO	carrier frequency offset
CONFAC	constrained factor
CPE	common phase error
CS	compressing sensing
CSI	channel state information
DF	decode-and-forward
DFT	discrete Fourier transform
DS-CDMA	direct sequence code division multiple access
EE	energy efficiency
EEG	electroencephalography
FR	frequency range
GHz	Giga-Hertz
HOSVD	higher-order singular value decomposition
I2I	indoor-to-indoor
I2O	indoor-to-outdoor
IAB	integrated access and backhaul
ICI	inter-carrier interference
IOS	intelligent omni-surface
IoT	Internet of Things
IRS	intelligent reflecting surfaces
KF	Kronecker factorization

kHz	kilo-Hertz
KRF	Khatri-Rao factorization
LIS	large intelligent surfaces
LOS	line-of-sight
LRA	low-rank approximation
LS	least squares
LSKP	least squares Kronecker product
LSKRF	least squares Khatri-Rao factorization
LTE	Long Term Evolution
MECG	multi-lead electrocardiogram
MEG	magnetoencephalography
MHz	Mega-Hertz
MIMO	multiple-input multiple-output
MISO	multiple-input single-output
mmWave	millimeter-wave
NLOS	non-line-of-sight
NMSE	normalized mean square error
NOMA	non-orthogonal multiple access
O2I	outdoor-to-indoor
O2O	outdoor-to-outdoor
OFDM	orthogonal frequency division multiplexing
PARAFAC	PARAllel FACtors
PIN	positive-intrinsic-negative
PN	phase-noise
RF	radio frequency
RIS	reconfigurable intelligent surface
RX	receiver
SE	spectral efficiency
SER	symbol error rate
SISO	single-input single-output
SKP	selective Kronecker product
SNR	signal-to-noise ratio
STAR	simultaneous transmitting and reflecting
SVD	singular value decomposition
THz	Tera-Hertz
TT	tensor train
TX	transmitter
UAV	unmanned aerial vehicle
UE	user equipment

ULA	uniform linear array
ZF	zero-forcing
ZFSKP	zero forcing selective Kronecker product

LIST OF SYMBOLS

$\underset{x\in\mathcal{A}}{\arg\min}\{f(x)\}$	Minimum argument $x \in \mathcal{A}$ of a function $f(x)$
$(\cdot)^{\mathrm{T}}$	Vector/Matrix transposition operator
$(\cdot)^{\mathrm{H}}$	Matrix Hermitian operator
$\lvert a\rvert$	Absolute value of a
$\lvert\lvert\cdot\rvert\rvert_{\mathrm{F}}$	Frobenius norm
$\lvert\lvert\cdot\rvert\rvert_{\mathrm{F}}$	Euclidean norm
$\mathbb{E}\{\cdot\}$	Expected value
$\mathcal{O}(\cdot)$	Complexity order
$\circ$	Outer product
$\otimes$	Kronecker product
$\diamond$	Khatri-Rao product
$\odot$	Hadamard product
$\oslash$	Vector/Matrix/Tensor element-wise division
$\times_n$	Tensor n-mode product
$\sqcup_N$	Vector/Matrix/Tensor concatenation at the N-th dimension
N_0	Noise spectral density
$\mathbf{1}_a$	Column vector with length a with all elements equal to 1

SUMMARY

1 INTRODUCTION

1.1 Motivation

The use of tensor algebra techniques in signal processing has been growing over the last two decades. Applications like image processing [1, 2, 3, 4], biomedical signal processing [5, 6, 7, 8], array processing [9, 10, 11, 12], machine/deep learning [13, 14, 15, 16], and communications [17, 18, 19, 20, 21, 22], in general, largely employ tensor-based techniques for recovery, estimating, and classifying signals. One of the main reasons for using tensor signal processing is the exploitation of the multidimensional structure of signals, where the information can be analyzed trough different dimensions. For example, in wireless communications, the signals can have several dimensions, e.g., space, time, frequency, polarization, beamspace, etc. In addition, tensor-based models, compared to matrix-based processing, benefits from a more flexible uniqueness properties, where uniqueness means that a tensor factor (or parameter) is unique estimated, under a scaling and/or permutation ambiguity if some mild conditions are satisfied [23, 24]. For example, for the PARAllel FACtors (PARAFAC) decomposition [25], uniqueness can be granted by satisfying the Kruskal conditions, while for the Tucker decomposition [26] if the core tensor is known *a priori*, the factors can be uniquely estimated under scaling ambiguities. Other tensor models that have appeared in the literature are the constrained factor (CONFAC) [18], PARATuck [27], Nested Tucker [28], and the Nested PARAFAC [29], which constitute different generalizations, or combinations, of the PARAFAC and Tucker decompositions. More recently, the tensor train (TT) decomposition [30] has attracted interest in large-scale tensor data processing [1, 31, 32, 33, 34].

As mentioned, tensor-based signal processing has application in several research areas. In image processing, the authors of [1] apply the TT decomposition to image and video recovery. In [2] and [4], the Tucker decomposition is proposed in hyperspectral image denoising, where in [2], the authors used a joint approach of the Tucker model and principal component analysis by exploiting the correlation among all data dimensions, while [4] accounts the spatial nonlocal similarity structures. In [3], the authors proposes a Tucker decomposition for lossy image compression by exploiting the sparsity of the images.

Regarding the biomedical research area, the work [8] proposes a PARAFAC model combining electroencephalography (EEG) and magnetoencephalography (MEG) data. In [7], a rank-one tensor model is used for dictionary learning in the context of spectral computed tomography reconstruction. The authors of [6] propose an online compression of multi-lead electrocardiogram (MECG) data using a PARAFAC model. Finally, a survey of tensor-based signal processing in biomedical signals is presented in [5].

In the array processing research, tensor-based processing is largely employed. The work [9], is a prior work where the authors show the link of PARAFAC model in sensor array

processing, exploiting its uniqueness property. In [10], the authors propose a spatial smoothing tensor-based method using the higher-order singular value decomposition (HOSVD) algorithm, improving signal subspace estimation. In [12], the authors proposed a tensor-based channel estimation method for dual-polarized antennas in massive multiple-input multiple-output (MIMO) systems. More specifically, they consider a low-rank PARAFAC model for the channel, due to the massive number of antennas at the transmitter and receiver sides. Finally, in [11], an overview of the applications of tensor-based methods in MIMO radar system is presented.

In wireless communication systems, several works employ tensor-based signal processing methods. The work of [17] was the first to link PARAFAC modeling to design blind receivers, where a direct sequence code division multiple access (DS-CDMA) communication system was considered. In [19], the authors propose a semi-blind receiver based on double Khatri-Rao space-time codes. In [20] a tensor-based framework for channel estimation in MIMO systems, namely TENCE, is proposed, where the authors show a performance improvement compared to matrix-based signal processing schemes. The works of [35, 36, 37] consider the application of tensor-based signal processing in MIMO-Orthogonal frequency division multiplexing (OFDM) systems. In [38], the authors propose to model the received signal as the double tensor contraction between the transmitted PARAFAC signal and the channel, allowing the receiver to fully exploit the received signal spatial and coding diversity. In [36] and [37], tensor-based channel estimation methods are considered. By assuming millimeter-wave (mmWave) channels the authors exploit the sparsity of the channel with compressing sensing (CS) tools. The work of [36] proposes a Tucker model framework for channel estimation, while [37] considers a low-rank PARAFAC modeling approach. Recently, the IRS topic emerges as a potential key technology for future fifth-generation (5G) and sixth-generation (6G) networks. In this context, the work of [22] proposes a tensor-based framework for channel estimation in MIMO IRS-assisted networks.

In summary, tensor-based signal processing has a major impact in many research areas. This thesis is divided into two parts. First, we develop new tensor-based signal processing receivers for MIMO-OFDM systems with the presence of phase-noise impairments. Second, we derive a low-rank tensor approximation model to reduce the control signal overhead in MIMO IRS-assisted communication system.

1.2 Major Contributions

The main contributions of this thesis can be listed in the following three research areas:

- Tensor algebra;
- MIMO-OFDM systems;
- IRS-aided systems.

Tensor Algebra: In this context, we propose a new operator, namely selective Kronecker product (SKP), that allows defining the spreading of the Kronecker product into specific dimensions,

while keeping the others fixed. As it is described in Chapter 2, the selective Kronecker product (SKP) is a middle-term operator, i.e., lies between the traditional Kronecker product and the outer product. This operator plays a key role in Chapter 4 allowing to model the received data signal using a structured Tucker model.

MIMO-OFDM systems: We derive a two-stage tensor-based receiver. In the first stage, the pilot received signal is modelled as a PARAFAC tensor. Then, two algorithms are proposed to jointly estimate the phase-noise impairments and the pilot channel matrix. The first algorithm is based on an iterative solution (BALS), while the second algorithm is based on a closed-form solution (LSKRF). In the second stage, based on the proposed SKP operator, the data received signal is modelled as a structured Tucker tensor, and the transmitted data is estimated all-at-once.

IRS-aided systems: We propose a low-rank approximation of the near-optimal IRS phase-shift vector to reduce IRS phase-shift feedback overhead. To this end, two tensor-based models, namely PARAFAC-IRS and Tucker-IRS, are proposed to factorize a *tensorized* version of the IRS phase-shift vector. In both models, each component is modeled as the Kronecker product of a predefined number of factors of smaller sizes, which can be obtained *via* tensor decomposition algorithms. The proposed method is especially attractive in scenarios with a strong line of sight component, in which case nearly the same spectral efficiency is reached as in the cases with near-optimal phase-shifts, but with a drastically reduced communication overhead.

1.3 Thesis Organization

This thesis is organized into six chapters, including this introductory. Figure 1.1 depicts the link between the chapters and their main topics. The rest of the chapters are briefly summarized as

Chapter 2: *Matrix and Tensor Algebra Preliminaries* details the matrix and tensor properties and operations, including the proposed SKP operator. We focus on the discussion of the PARAFAC and Tucker tensor decompositions where state-of-the-art algorithms are revisited. More especially, we present the alternating least squares (ALS), and the higher-order singular value decomposition (HOSVD) algorithms for tensor factor estimation. In addition, the least squares Khatri-Rao factorization (LSKRF) and the least squares Kronecker product (LSKP) factorizations are discussed in detail. This chapter contains the tools that are largely employed in the applications in Chapters 4 and 5.

Chapter 3: *Intelligent Reconfigurable Surfaces Overview* presents an overview of intelligent reflecting surfaces (IRS) technology, its benefits, and applications in future 5G and 6G networks. In addition, the channel estimation problem and the beamforming optimization methods are discussed. Finally, we emphasize the discussion over the IRS phase-shift feedback overhead problem where we present the current state-of-the-art model for IRS phase-shift overhead-aware feedback.

Figure 1.1 – Link between the chapters.

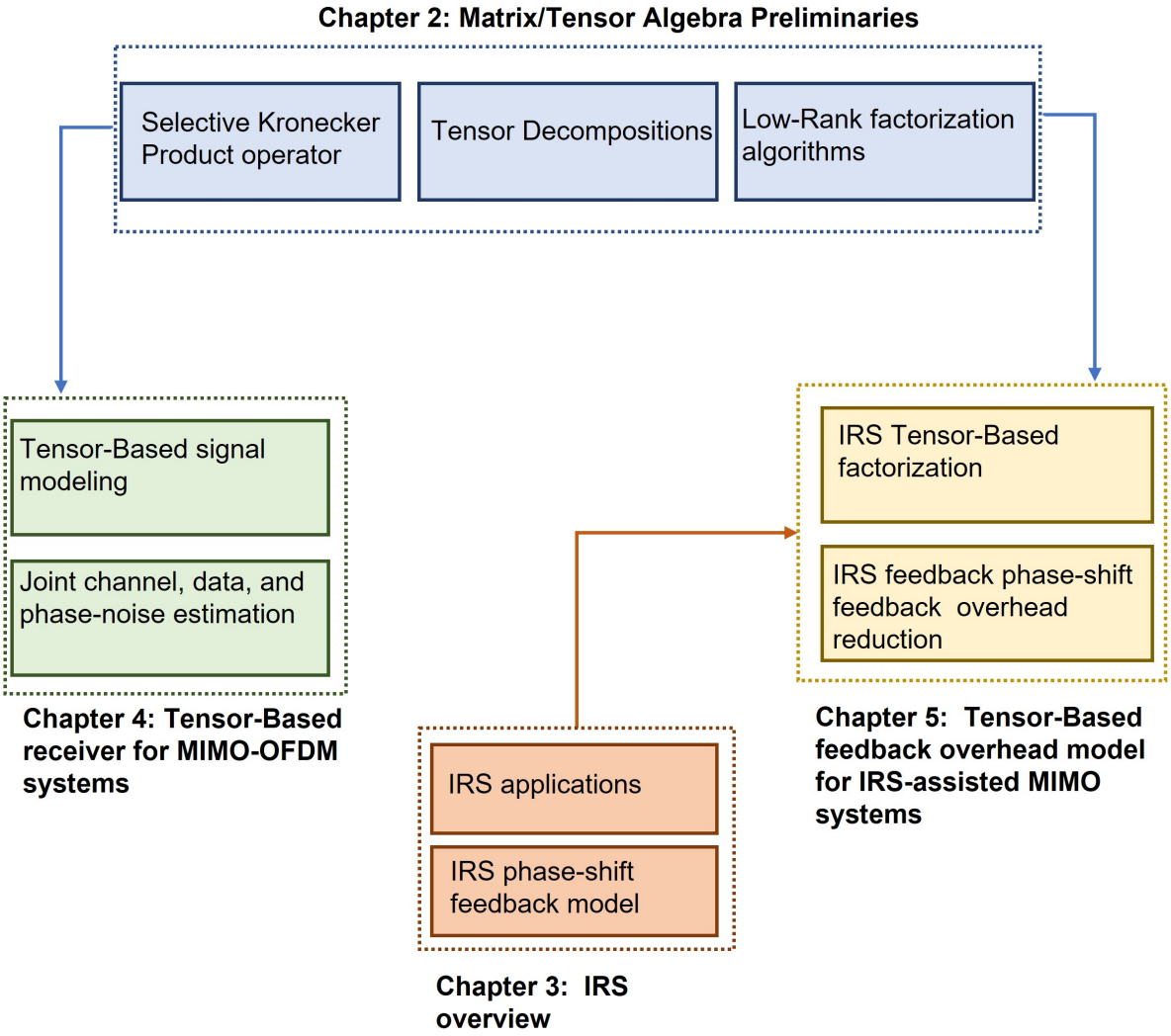

Source: Created by the author.

Chapter 4: *Tensor-Based Receiver for Parameter Estimation in MIMO-OFDM Systems*. In this chapter, we discuss the phase-noise impairment in MIMO-OFDM systems that leads to inter-carrier interference (ICI), causing a perturbation in the system that must be taken into account. To this end, we propose a tensor-based solution in which we derive a two-stage receiver. In the first stage, the pilot signal is modelled as a PARAFAC tensor, two algorithms are proposed to jointly estimate the phase-noise matrix and the pilot channel matrix. In the second stage, a zero forcing filter is derived to estimate the transmitted data, thanks to the proposed SKP operator.

Chapter 5: *Tensor-Based Method for Reducing the Control Signaling in IRS-assisted MIMO Systems*. In this chapter, we propose two tensor-based models, namely PARAFAC-IRS and Tucker-IRS, to reduce the IRS phase-shift feedback overhead in IRS-assisted MIMO systems. We show that in the proposed tensor-based models the total number of phase-shifts required to be conveyed to the IRS controller is drastically reduced compared to the state-of-the-art IRS phase-shift feedback overhead-aware method.

Chapter 6: *Conclusion and Future Perspectives*. In this chapter, we draw the final comments on the application of tensor-based methods in wireless communications, especially in MIMO-OFDM and IRS-assisted systems.

1.4 Main Scientific Production

The content of this thesis is published/submitted in the following journals and conferences:

1.4.1 Journal Papers

[J1] **SOKAL, B.**; GOMES, P. R. B.; de ALMEIDA, A. L. F.; HAARDT, M. "*Tensor-Based Receiver for Joint Channel, Data, and Phase-Noise Estimation in MIMO-OFDM Systems,*" Journal of Selected Topics in Signal Processing, vol. 15, no. 3, pp. 803-815, April 2021, doi: 10.1109/JSTSP.2021.3061917.

[J2] **SOKAL, B.**; GOMES, P. R. B.; de ALMEIDA, A. L. F.; MAKKI, B.; FODOR, G. "*Reducing the Control Overhead of Intelligent Reconfigurable Surfaces Via a Tensor-Based Low-Rank Factorization Approach,*" **submitted to:** IEEE Transactions on Wireless Communications

1.4.2 Conference Papers

[C1] **SOKAL, B.**; de ALMEIDA, A. L. F.; HAARDT, M. "*Semi-Blind Receiver for Two-Hop MIMO Relaying Systems via Selective Kronecker Product Modeling*". In: 2019 IEEE 8th International Workshop on Computational Advances in MultiSensor Adaptive Processing (CAMSAP), 2019, Le gosier.

[C2] **SOKAL, B.**; GOMES, P. R. B.; de ALMEIDA, A. L. F.; HAARDT, M. "*Joint Channel, Data, and Phase-Noise Estimation in MIMO-OFDM Systems Using a Tensor Modeling Approach,*" in Proceedings IEEE International Conference on Acoustics, Speech and Signal Processing (ICASSP), 2021, pp. 4460-4464, doi: 10.1109/ICASSP39728.2021.9414541.

[C3] **SOKAL, B.**; GOMES, P. R. B.; de ALMEIDA, A. L. F.; MAKKI, B.; FODOR, G. "*IRS Phase-Shift Feedback Overhead-Aware Model Based on Rank-One Tensor Approximation,*" **submitted to:** IEEE GLOBECOM 2022

1.4.3 Patent

[P1] **SOKAL, B.**; GOMES, P. R. B.; de ALMEIDA, A. L. F.; MAKKI, B.; FODOR, G. "*APROACH FOR CONTROL OF A RADIO REFLECTOR,*" P. number: 103277

It is important to mention that, the works [J1], [C1], and [C2] were part of the Ph.D. cotutelle program established between the UFC and the Technische Universität Ilmenau (TUI). In addition,

the works [J2], [C3], and [P1] were promoted under the project UFC.48 Technical Cooperation Contract Ericsson/UFC.

1.5 Other Scientific Production

During the Ph.D. duration, the author was also involved at the publication and of the following research papers

1.5.1 Journal Papers

[J3] **SOKAL, B.**; de ALMEIDA, A. L. F.; HAARDT, M. "*Semi-blind receivers for MIMO multi-relaying systems via rank-one tensor approximations,*" Signal Processing, Volume 166, January 2020, pp.107254, ISSN 0165-1684, doi: 10.1016 / j.sigpro.2019.107254.

[J4] PESSOA, A. M.; **SOKAL, B.**; SILVA, C. F. M.; MACIEL, T. F.; ALMEIDA, A. L. F.; CAVALCANTI, F. R. P. "*A CDL-based channel model with dual-polarized antennas for 5G MIMO systems in rural remote areas,*", in IEEE Access, vol. 8, pp. 163366-163379, Aug. 2020, doi: 10.1109/ACCESS

[J5] GOMES, P. R. B.; ARAÚJO G. T.; **SOKAL, B.**; de ALMEIDA, A. L. F.; MAKKI, B.; FODOR, G. "*Channel Estimation in RIS-Assisted MIMO Systems Operating Under Imperfections,*" **submitted to:** IEEE Transactions on Vehicular Technology

1.5.2 Conference Papers

[C4] **SOKAL, B.**; de ALMEIDA, A. L. F.; HAARDT, M. "*Rank-One Tensor Modeling Approach to Joint Channel and Symbol Estimation in Two-Hop MIMO Relaying Systems*". In: XXXV Simpósio Brasileiro de Telecomunicações e Processamento de Sinais, 2017, São Pedro - SP

[C5] RIBEIRO, L; **SOKAL, B.**; de ALMEIDA, A. L. F.; MOTA, João C. . "*Separable Least-Mean Squares Beamforming*". In: XXXVI Simpósio Brasileiro de Telecomunicações e Processamento de Sinais, 2018, Campina Grande - PB

[C6] PESSOA, A. M.; **SOKAL, B.**; SILVA, C. F. M.; MACIEL, T. F.; ALMEIDA, A. L. F.; SOUSA, D. A.; SILVA, Y. C. CAVALCANTI, F. R. P. "*CDL-based Channel Model for 5G MIMO Systems in Remote Rural Areas,*", In: 2019 16th International Symposium on Wireless Communication Systems (ISWCS), 2019, Oulu. 2019 16th International Symposium on Wireless Communication Systems (ISWCS), 2019. pp. 21-26, doi: 10.1109/ISWCS.2019.8877334.

- [C7] FERREIRA, A.; MENDES, L.; DIAS, W.; MARTINS, T; GASPAR, D; PESSOA, A. M.; SILVA, C. F. M.; **SOKAL, B**. "*5G-RANGE project field trial,*" in Proc. European Conference on Networks and Communications (EuCNC), Valencia, Spain, 2019, pp. 490-494, doi: 10.1109/EuCNC.2019.8802021.

[C8] GOMES, P. R. B.; **SOKAL, B.**; de ALMEIDA, A. L. F.; HAARDT, M. "*Tensor-Based Semi-Blind Receiver for Channel and Symbol Estimation in Frequency-Selective MIMO Systems with Phase Noise Impairments,*" In: XXXVIII Simpósio Brasileiro de Telecomunicações e Processamento de Sinais, 2020, Florianópolis-SC.

[C9] ARDAH, K; **SOKAL, B.**; de ALMEIDA, A. L. F.; HAARDT, M. "*Compressed Sensing Based Channel Estimation and Open-loop Training Design for Hybrid Analog-digital Massive MIMO Systems,*" In: ICASSP 2020 2020 IEEE International Conference on Acoustics, Speech and Signal Processing (ICASSP), 2020, Barcelona.

[C10] RAKHIMOV, D; DERAM, S. P.; **SOKAL, B.**; NASKOVSKA, K.; de ALMEIDA, A. L. F.; HAARDT, M. "*Iterative Tensor Receiver for MIMO-GFDM systems,*" In: 2020 IEEE 11th Sensor Array and Multichannel Signal Processing Workshop (SAM), 2020, Hangzhou.

[C11] BENÍCIO, K. B.; **SOKAL, B.**; de ALMEIDA, A. L. F.. "*Channel Estimation and Joint Beamforming Design for Multi-IRS MIMO systems,*" In: XXXIX Simpósio Brasileiro de Telecomunicações e Processamento de Sinais, 2021, Fortaleza.

[C12] BENÍCIO, K. B.; **SOKAL, B.**; de ALMEIDA, A. L. F.. "*Channel Estimation and Performance Evaluation of Multi-IRS Aided MIMO Communication System,*" In: 2021 Workshop on Communication Networks and Power Systems (WCNPS), 2021, Brasilia.

1.5.3 Technical Reports

[T1] 5G-RANGE, "*Architecture, system and interface definitions of a 5G for Remote Area network,*" Deliverable 2.2, Aug. 2018. Available from: <http://5g-range.eu/index.php/category/deliverables/>.

[T2] 5G-RANGE, "*Physical layer of the Remote Area Access Network for the 5th Generation (5G-RANGE) – Part I,*" Deliverable 3.1, Dec. 2018. Available from: <http://5g-range.eu/index.php/category/deliverables/>.

[T3] 5G-RANGE, "*Physical layer of the Remote Area Access Network for the 5th Generation (5G-RANGE) – Part II,*" Deliverable 3.2, Feb. 2019. Available from: <http://5g-range.eu/index.php/category/deliverables/>.

It is worth mentioning that the items [J4], [C6]-[C7], and [T1]-[T3] were developed during the Remote area Access Network for 5th GEneration (5G-RANGE) project, from Nov/2017 to Jan/2019.

2 MATRIX AND TENSOR ALGEBRA PRELIMINARIES

In this chapter, some of the key definitions and properties of the matrix and tensor algebra that are useful in this document are discussed. In addition, the PARAllel FACtors (PARAFAC) and Tucker tensor decompositions are presented, with a detailed discussion on their uniqueness properties and estimation algorithms. Finally, we discuss the Kronecker factorization (KF) and the Khatri-Rao factorization (KRF) algorithms where the matrix estimation problem is recast into rank-one matrix and tensor problems. For more details, the reader can find in [23, 39, 40] a very detailed survey on tensors applications and properties.

2.1 Matrix Basics

In this document, we use the concepts of the Kronecker, Khatri-Rao, Hadamard products. In addition, we provide essential properties and concepts involving those products.

2.1.1 Hadamard Product

The Hadamard product is an element-wise product. In other words, is only possible when the factors have the same dimensions. Consider two matrices $\boldsymbol{A} \in \mathbb{C}^{I \times R}$ and $\boldsymbol{B} \in \mathbb{C}^{I \times R}$. The Hadamard product between them is defined as

$$\boldsymbol{C} = \boldsymbol{A} \odot \boldsymbol{B} \in \mathbb{C}^{I \times R}, \tag{2.1}$$

where $c_{i,j} = a_{i,j} b_{i,j}$ for $i = \{1, \ldots, I\}$, and $j = \{1, \ldots, J\}$. Inversely, we define the element-wise division operator $\oslash$, as

$$\boldsymbol{C} = \boldsymbol{A} \oslash \boldsymbol{B} \in \mathbb{C}^{I \times R}, \tag{2.2}$$

where, in this case, $c_{i,j} = a_{i,j} / b_{i,j}$ for $i = \{1, \ldots, I\}$, and $j = \{1, \ldots, J\}$.

2.1.2 Kronecker Product

The Kronecker product combines two or more factors that can have different sizes. Let us assume $\boldsymbol{X} \in \mathbb{C}^{I \times J}$ and $\boldsymbol{Y} \in \mathbb{C}^{M \times N}$. The Kronecker product between them is defined as

$$\boldsymbol{Z} = \boldsymbol{X} \otimes \boldsymbol{Y} \in \mathbb{C}^{MI \times NJ}, \tag{2.3}$$

$$= \begin{bmatrix} \left[x_{1,1}\boldsymbol{Y}\right]_{M \times N} & \cdots & \left[x_{1,J}\boldsymbol{Y}\right]_{M \times N} \\ \vdots & \ddots & \vdots \\ \left[x_{I,1}\boldsymbol{Y}\right]_{M \times N} & \cdots & \left[x_{I,J}\boldsymbol{Y}\right]_{M \times N} \end{bmatrix}. \tag{2.4}$$

It is important to note that, the factor on the right side of the Kronecker operator is the one that has its elements vary faster. We can observe that the whole matrix $\boldsymbol{Y}$ varies under one element variation of $\boldsymbol{X}$, forming a block structure. In this document, we order the dimensions of the

resulting matrix by the ones that varies faster, which in this case, for $\boldsymbol{Z}$ is the dimension M in rows, and N in the columns.

2.1.3 Khatri-Rao Product

The Khatri-Rao product is also known as the column-wise Kronecker product, consequentially, requires matrices with the same number of columns. Let us define the matrices $\boldsymbol{A} \in \mathbb{C}^{I \times R}$ and $\boldsymbol{B} \in \mathbb{C}^{J \times R}$, the Khatri-Rao product between them is defined as

$$\boldsymbol{C} = \boldsymbol{A} \diamond \boldsymbol{B} \in \mathbb{C}^{JI \times R} \tag{2.5}$$

$$= \begin{bmatrix} \boldsymbol{a}_1 \otimes \boldsymbol{b}_1, & \dots & \boldsymbol{a}_r \otimes \boldsymbol{b}_r, & \dots & \boldsymbol{a}_R \otimes \boldsymbol{b}_R \end{bmatrix}, \tag{2.6}$$

where $\boldsymbol{a}_r$ and $\boldsymbol{b}_r$ are the r-th column of $\boldsymbol{A}$ and $\boldsymbol{B}$, respectively.

2.1.4 Vectorization

Let us consider a matrix $\boldsymbol{A} = [\boldsymbol{a}_1, \dots, \boldsymbol{a}_R] \in \mathbb{C}^{I \times R}$. We define the $\text{vec}(\cdot)$ operator as

$$\boldsymbol{a} = \text{vec}\,(\boldsymbol{A}) = \begin{bmatrix} \boldsymbol{a}_1 \\ \vdots \\ \boldsymbol{a}_R \end{bmatrix}, \tag{2.7}$$

inversely, we define the $\text{unvec}_{\text{dim}}(\cdot)$ operator that reshapes a vector into a matrix (or a tensor), expressed as

$$\boldsymbol{A} = \text{unvec}_{I \times R}\,(\boldsymbol{a}) \in \mathbb{C}^{I \times R}. \tag{2.8}$$

2.1.5 Outer Product

The outer product between two vectors $\boldsymbol{a} \in \mathbb{C}^{I \times 1}$, and $\boldsymbol{b}^{J \times 1}$ defines a rank-one matrix, i.e.,

$$\boldsymbol{C} = \boldsymbol{a} \circ \boldsymbol{b} \in \mathbb{C}^{I \times J}$$

$$= \boldsymbol{a}\boldsymbol{b}^{\text{T}}. \tag{2.9}$$

2.1.6 Properties of Hadamard, Kronecker, and Khatri-Rao Products

Some of the key properties of the above discussed products and operators are the following

$$(\boldsymbol{A} \otimes \boldsymbol{B})\,(\boldsymbol{C} \otimes \boldsymbol{D}) = (\boldsymbol{A}\boldsymbol{C}) \otimes (\boldsymbol{B}\boldsymbol{D}), \tag{2.10}$$

$$(\boldsymbol{A} \otimes \boldsymbol{B})\,(\boldsymbol{C} \diamond \boldsymbol{D}) = (\boldsymbol{A}\boldsymbol{C}) \diamond (\boldsymbol{B}\boldsymbol{D}), \tag{2.11}$$

$$\text{vec}\,(\boldsymbol{A}\boldsymbol{B}\boldsymbol{C}) = \left(\boldsymbol{C}^{\text{T}} \otimes \boldsymbol{A}\right) \text{vec}\,(\boldsymbol{B}), \tag{2.12}$$

$$\text{vec}\,(\boldsymbol{A}\text{diag}\,(\boldsymbol{v})\,\boldsymbol{C}) = \left(\boldsymbol{C}^{\text{T}} \diamond \boldsymbol{A}\right) \boldsymbol{v}, \tag{2.13}$$

$$\text{vec}\,(\boldsymbol{a} \circ \boldsymbol{b}) = \boldsymbol{b} \otimes \boldsymbol{a}. \tag{2.14}$$

2.2 Tensor Basics

A tensor is an multidimensional array with dimensions greater than two. In fact, scalars, vectors and matrices can be considered as tensors of dimensions zero, one, and two, respectively. A N-th order tensor is defined as $\mathcal{X} \in \mathbb{C}^{I_1 \times I_2 \times \ldots \times I_N}$. The scalar representation of $\mathcal{X}$ is given as $\mathcal{X}_{i_1,i_2,\ldots,\ldots,i_N}$, with $i_n = \{1,\ldots,I_n\}$ and $n = \{1,\ldots,N\}$.

2.2.1 Tensor Slices

Slices are formed by fixing two dimensions and varying one or more. Depending on the tensor order, they can form lower-order tensor or matrices. For a better visualization, let us consider the third-order tensor $\mathcal{Q} \in \mathbb{C}^{I \times J \times K}$. We can slice the tensor $\mathcal{Q}$ in three different ways, as illustrated in Fig. 2.1. The frontal, lateral and horizontal slices are depicted in Fig. 2.1 (a), (b), and (c), respectively. In the case of third order tensors, its slices are matrices, defined as

Figure 2.1 – Illustration of a third-order tensor and its different slices.

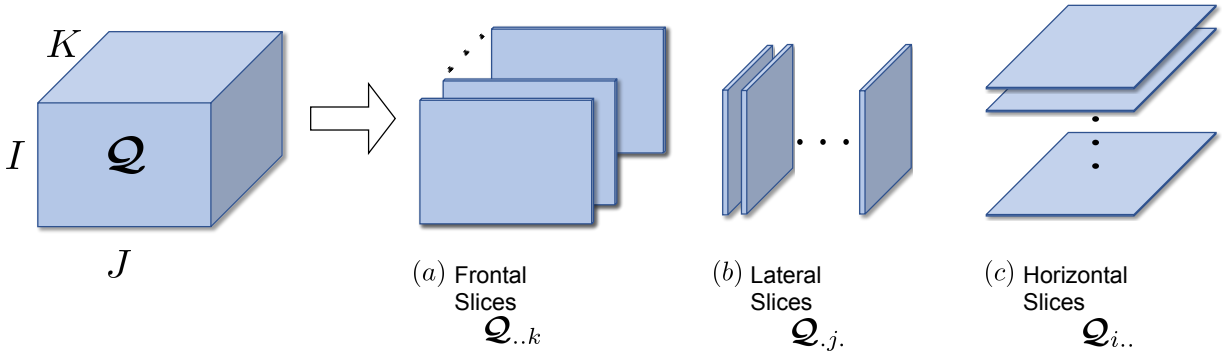

Source: Created by the author.

$$\mathcal{Q}_{..k} \in \mathbb{C}^{I \times J}, \text{ for } k = \{1,\ldots K\}, \tag{2.15}$$

$$\mathcal{Q}_{.j.} \in \mathbb{C}^{I \times K}, \text{ for } j = \{1,\ldots J\}, \tag{2.16}$$

$$\mathcal{Q}_{i..} \in \mathbb{C}^{J \times K}, \text{ for } i = \{1,\ldots I\}. \tag{2.17}$$

In other words, we have K matrices of size $I \times J$ by frontal slicing $\mathcal{Q}$, J matrices of size $I \times K$ by considering the lateral slices of $\mathcal{Q}$, and I matrices of size $J \times K$ if we slice $\mathcal{Q}$ in the horizontal direction. Nevertheless, the concept of slicing a tensor can be generalized to a N-th order tensor since the idea is to fix two or more of dimensions, while varying the others.

2.2.2 Tensor Unfolding

The tensor unfolding operation consists of mapping the elements of a tensor into a matrix. This is proceeded by selecting one dimension of the tensor and fixing it as rows of the matrix, while the remaining dimensions are fixed as columns. Taking, for example, the third order tensor $\mathcal{Q}$, illustrate in Figure 2.1, we can define three unfolding matrices, called as 1-mode

unfolding, 2-mode unfolding, and 3-mode unfolding. They can formed by collecting the frontal slices of $\mathcal{Q}$, as

$$[\mathcal{Q}]_{(1)} = [\mathcal{Q}_{..1}, \ldots, \mathcal{Q}_{..K}] \in \mathbb{C}^{I \times JK}, \tag{2.18}$$

$$[\mathcal{Q}]_{(2)} = \left[\mathcal{Q}_{..1}^{\mathrm{T}}, \ldots, \mathcal{Q}_{..K}^{\mathrm{T}}\right] \in \mathbb{C}^{J \times IK}, \tag{2.19}$$

$$[\mathcal{Q}]_{(3)} = \left[\mathrm{vec}(\mathcal{Q}_{..1}^{\mathrm{T}}), \ldots, \mathrm{vec}(\mathcal{Q}_{..K}^{\mathrm{T}})\right] \in \mathbb{C}^{K \times IJ}, \tag{2.20}$$

respectively. For a N-th order tensor, we have N matrices unfoldings. The mapping of elements from the N-th order tensor $\mathcal{X}_{i_1,i_2,\ldots,i_n,\ldots,i_N}$ to its n-mode unfolding matrix $[\mathcal{X}]_{(n)} \in \mathbb{C}^{I_n \times I_1 \cdots I_{n-1} I_{n+1} \cdots I_N}$ is given by

$$\mathcal{X}_{i_1,i_2,\ldots,i_n,\ldots,i_N} \rightarrow [\mathcal{X}]_{(n)\, i_n; i_1+(i_2-1)I_1+\ldots+(i_N-1)I_{N-1}\cdots I_{n+1} I_{n-1}\cdots I_1} \in \mathbb{C}^{I_n \times I_1 \cdots I_{n-1} I_{n+1} \cdots I_N}.$$

2.2.3 Tensor Generalized Unfolding

The traditional unfolding operation only selects one dimension of a tensor and fix it as rows of a matrix, while the remaining dimensions are combined and fixed as columns. The generalized unfolding operation consists of defining two subsets of dimensions, where the first subset $\mathbb{S}_1$ is used to define the rows of the generalized unfolding matrix, while the second subset $\mathbb{S}_2$ defines the columns. For example, let us consider a fourth order tensor $\mathcal{P} \in \mathbb{C}^{R_1 \times R_2 \times R_3 \times R_4}$. We can define $\mathbb{S}_1 = \{R_1, R_2\}$ as the set that contains the first and second dimension of $\mathcal{P}$, and $\mathbb{S}_2 = \{R_3, R_4\}$ containing the third and fourth dimension of $\mathcal{P}$. An example of generalized unfolding of $\mathcal{P}$ is $[\mathcal{P}]_{([\mathbb{S}_1],[\mathbb{S}_2])} = [\mathcal{P}]_{([1,2],[3,4])} \in \mathbb{C}^{R_1 R_2 \times R_3 R_4}$. Note that, in this example, different generalized unfoldings can be formed, for example $[\mathcal{P}]_{([1,3],[2,4])} \in \mathbb{C}^{R_1 R_3 \times R_2 R_4}$, and $[\mathcal{P}]_{([1,4],[2,3])} \in \mathbb{C}^{R_1 R_4 \times R_2 R_3}$.

2.2.4 Tensor n-mode product

The n-mode product performs a linear combination of a tensor with a matrix. Let us consider the N-th order tensor $\mathcal{X}$ and a matrix $\boldsymbol{A} \in \mathbb{C}^{J \times I_n}$. The n-mode product results in a new tensor, $\mathcal{W}$ denoted by

$$\mathcal{W} = \mathcal{X} \times_n \boldsymbol{A} \in \mathbb{C}^{I_1 \times \ldots \times J \times \ldots I_N}, \tag{2.21}$$

and can be written as function of its n-mode unfolding as

$$[\mathcal{W}]_{(n)} = \boldsymbol{A}\, [\mathcal{X}]_{(n)} \in \mathbb{C}^{J \times I_1 \cdots I_{n-1} I_{n+1} \cdots I_N}. \tag{2.22}$$

Note that, the product in (2.21) can be generalized to multiple modes, i.e., supposing a set of matrices $\boldsymbol{A}^{(n)} \in \mathbb{C}^{J_n \times I_n}$, for $n = \{1, \ldots, N\}$, we can define the tensor $\mathcal{W}$ as

$$\mathcal{W} = \mathcal{X} \times_1 \boldsymbol{A}^{(1)} \times_2 \boldsymbol{A}^{(2)} \times_3 \ldots \times_N \boldsymbol{A}^{(N)} \in \mathbb{C}^{J_1 \times J_2 \times \ldots \times J_N}. \tag{2.23}$$

This is also known as a Tucker decomposition, which will be discussed in details further in this chapter. The n-mode unfolding of $\mathcal{W}$ is given by

$$[\mathcal{W}]_{(n)} = \boldsymbol{A}^{(n)}\, [\mathcal{X}]_{(n)} \left(\boldsymbol{A}^{(N)} \otimes \ldots \otimes \boldsymbol{A}^{(n+1)} \otimes \boldsymbol{A}^{(n-1)} \otimes \ldots \otimes \boldsymbol{A}^{(1)}\right)^{\mathrm{T}}. \tag{2.24}$$

2.2.5 Identity Tensor

An identity matrix, defined $\boldsymbol{I}_R \in \mathbb{R}^{R\times R}$, is a square matrix whose elements are equal to one if the row and column indices are equal, i.e., $r_1 = r_2$, for r_1 and $r_2 = \{1,\ldots,R\}$, while being zero otherwise. Likewise, a N-th order identity tensor $\mathcal{I}_{N,R} \in \mathbb{R}^{R\times R\times\ldots\times R}$ is a tensor with elements equal to one when the indices $r_1 = r_2 = \ldots = r_n = \ldots = r_N$, for $r_n = \{1,\ldots,R\}$ and $n = \{1,\ldots,N\}$, and elements equal to zero otherwise. The upper index N indicates the order of the tensor, while the R indicates the number of elements different from zero e equal to one, where if $R = N$, the tensor is called a diagonal tensor [23]. Its n-mode unfolding is given by

$$[\mathcal{I}]_{(n)} = \boldsymbol{I}_R \underbrace{(\boldsymbol{I}_R \diamond \ldots \diamond \boldsymbol{I}_R)^{\mathrm{T}}}_{N-1 \text{ factors}} \in \mathbb{R}^{R\times R\cdots R}, \tag{2.25}$$

and, as it can be noticed, $[\mathcal{I}]_{(1)} = [\mathcal{I}]_{(2)} = \ldots = [\mathcal{I}]_{(N)}$ since it is the Khatri-Rao product of $N-1$ identity matrices of size $R\times R$. In addition, $[\mathcal{I}]_{(n)}$ only contains R columns different from zero.

2.2.6 Tensor contraction

As the n-mode product combines the columns of one (or more) matrices, the tensor contraction combines the same size dimensions of two (or more) tensors. For example, consider the tensor $\mathcal{A} \in \mathbb{C}^{I\times J\times K\times L}$ and the tensor $\mathcal{B} \in \mathbb{C}^{M\times K\times L\times N}$, we can combine them into a new tensor $C \in \mathbb{C}^{I\times J\times L\times M\times L\times N}$, defined as

$$C = \mathcal{A} \bullet_3^2 \mathcal{B}, \tag{2.26}$$

where $\bullet$ defines the contraction operator. In this case, we have combined the third dimension (lower index of $\bullet$) of $\mathcal{A}$ with the second dimension (upper index of $\bullet$) of $\mathcal{B}$. This operation is expressed in element-wise notation as

$$C_{i,j,l,m,l,n} = \sum_{k=1}^{K} \mathcal{A}_{i,j,k,l}\mathcal{B}_{m,k,l,n}. \tag{2.27}$$

This can also be expressed in function of the unfoldings of $\mathcal{A}$ and $\mathcal{B}$ as

$$[C]_{([1,2,3],[4,5,6])} = [\mathcal{A}]_{(3)}^{\mathrm{T}} [\mathcal{B}]_{(2)} \in \mathbb{C}^{IJL\times MLN}. \tag{2.28}$$

Moreover, the fourth dimension of $\mathcal{A}$ is the same as the third dimension of $\mathcal{B}$. Thus, we can extend the definition on (2.26) to a double contraction. Let us define the tensor $\mathcal{Z}$ as

$$\mathcal{Z} = \mathcal{A} \bullet_{3,4}^{2,3} \mathcal{B} \in \mathbb{C}^{I\times J\times M\times N}. \tag{2.29}$$

In this case, the double contraction is expressed in element-wise notation as,

$$\mathcal{Z}_{i,j,m,n} = \sum_{k=1}^{K}\sum_{l=1}^{L} \mathcal{A}_{i,j,k,l}\mathcal{B}_{m,k,l,n}. \tag{2.30}$$

Using the generalized unfolding definition, we can express $\mathcal{Z}$ as

$$[\mathcal{Z}]_{([1,2],[3,4])} = [\mathcal{A}]_{([1,2],[3,4])} [\mathcal{B}]_{([2,3],[1,4])}, \tag{2.31}$$

one can note that, the column indices of $[\mathcal{A}]_{([1,2],[3,4])}$ are the lower indices of the contraction operator (2.29), while the row indices of $[\mathcal{B}]_{([2,3],[1,4])}$ are the upper indices in the contraction operator.

2.2.7 Tensor Outer Product

Consider a N-th order tensor $\mathcal{X} \in \mathbb{C}^{I_1 \times \ldots \times I_N}$, and a M-th order tensor $\mathcal{Y} \in \mathbb{C}^{R_1 \times \ldots \times R_M}$. The outer product between forms a $(N+M)$-th order tensor, and its defined as

$$\mathcal{Z} = \mathcal{X} \circ \mathcal{Y} \in \mathbb{C}^{I_1 \times \ldots \times I_N \times R_1 \times \ldots \times R_M}, \tag{2.32}$$

$$\mathcal{Z}_{i_1,\ldots,i_N,r_1,\ldots,r_M} = \sum_{i_1=1}^{I_1} \cdots \sum_{i_N=1}^{I_N} \sum_{r_1=1}^{R_1} \cdots \sum_{r_m=1}^{R_M} \mathcal{X}_{i_1,\ldots,i_N} \mathcal{Y}_{r_1,\ldots,r_M}. \tag{2.33}$$

2.2.8 Tensor Kronecker Product

The tensor Kronecker product can be viewed as a special case of the outer product, where the dimensions are expanded by merging two or several dimensions into one. For example, considering the previous example for the case where $N = M = 3$, the tensor Kronecker product between $\mathcal{X}$ and $\mathcal{Y}$ forms a third order tensor defined as

$$\mathcal{T} = \mathcal{X} \otimes \mathcal{Y} \in \mathbb{C}^{R_1 I_1 \times R_2 I_2 \times R_3 I_3} \tag{2.34}$$

$$\mathcal{T}_{l_1,l_2,l_3} = \sum_{i_1=1}^{I_1} \sum_{i_2=1}^{I_2} \sum_{i_3=1}^{I_3} \sum_{r_1=1}^{R_1} \sum_{r_2=1}^{R_2} \sum_{r_3=1}^{R_3} \mathcal{X}_{i_1,i_2,i_3} \mathcal{Y}_{r_1,r_2,r_3}, \tag{2.35}$$

where $l_u = \{1, \ldots R_u, \ldots R_u I_u\}$, for $u = \{1, 2, 3\}$, is the element index of the expanded tensor $\mathcal{T}$, mapped as $l_u = r_u + (i_u - 1)R_u$. In the general case, where $N \neq M$ we have

$$\mathcal{T} = \mathcal{X} \otimes \mathcal{Y} \in \mathbb{C}^{R_1 I_1 \times R_2 I_2 \times \ldots \times R_M I_{N-M} \times I_{N-M+1} \times \ldots \times I_N}, \tag{2.36}$$

when $N > M$, and

$$\mathcal{T} = \mathcal{X} \otimes \mathcal{Y} \in \mathbb{C}^{R_1 I_1 \times R_2 I_2 \times \ldots \times R_{M-N} I_N \times R_{M-N+1} \times \ldots \times R_M}, \tag{2.37}$$

for the case where $M > N$.

2.2.9 Selective Kronecker Product

The outer product between tensors performs a dimension spread, while the Kronecker product performs an expansion. The SKP is a middle-term operator that selects which dimensions are combined to perform an expansion. For example, let us consider the previous Kronecker

product case for $N = M = 3$. As shown in (2.34), we have a third order tensor $\mathcal{T}$, with the frontal matrices slices defined as

$$\mathcal{T}_{..l} = \mathcal{X}_{..i_3} \otimes \mathcal{Y}_{..r_3} \in \mathbb{C}^{R_1 I_1 \times R_2 I_2}, \tag{2.38}$$

where $l = \{1, \ldots, R_2, \ldots, R_2 I_2\}$ is the index of the l-th frontal slice of $\mathcal{T}$, with $l = r_3 + (i_3 - 1)R_3$. However, using the SKP we can split the third dimension of $\mathcal{T}$ spreading it into a fourth dimension. This is given as

$$\bar{\mathcal{T}}_{..r_3,i_3} = \mathcal{X}_{..i_3} \otimes \mathcal{Y}_{..r_3} \in \mathbb{C}^{R_1 I_1 \times R_2 I_2}, \tag{2.39}$$

where $\bar{\mathcal{T}} \in \mathbb{C}^{R_1 I_2 \times R_2 I_2 \times R_3 \times I_3}$ is a fourth order tensor. Note that, the right hand side of (2.38) is equal to the right hand side of (2.39). The main difference is that we have splitted the third dimension of $\mathcal{T}$, $R_3 I_3$, into two dimensions, R_3 and I_3. This tensor operation is denoted by

$$\bar{\mathcal{T}} = \mathcal{X} \otimes_{1,2}^{1,2} \mathcal{Y} \in \mathbb{C}^{R_1 I_1 \times R_2 I_2 \times R_3 \times I_3}, \tag{2.40}$$

where the upper and lower indices in $\otimes$ indicates the combined dimensions of $\mathcal{X}$ and $\mathcal{Y}$, respectively. In other words, we are combining the first dimension of $\mathcal{X}$ with the first dimension of $\mathcal{Y}$ ($\otimes_1^1$), and the second dimension of $\mathcal{X}$ with the second dimension of $\mathcal{Y}$ ($\otimes_2^2$).
In general, the SKP can be performed in any dimensions of the factors. For example:

$$\begin{aligned}
\mathcal{X} \otimes_{1,2}^{2,3} \mathcal{Y} &\in \mathbb{C}^{R_2 I_1 \times R_3 I_2 \times R_1 \times I_3} \\
\mathcal{X} \otimes_{2,3}^{1,3} \mathcal{Y} &\in \mathbb{C}^{R_1 I_2 \times R_3 I_3 \times R_2 \times I_1} \\
\mathcal{X} \otimes_{2,3}^{1,2} \mathcal{Y} &\in \mathbb{C}^{R_1 I_2 \times R_2 I_3 \times R_3 \times I_1} \\
\mathcal{X} \otimes_{3,1,2}^{1,2,3} \mathcal{Y} &\in \mathbb{C}^{R_2 I_1 \times R_3 I_2 \times R_3 I_2}.
\end{aligned}$$

In the presented example, the tensor Kronecker product and the SKP are related as

$$\mathcal{X} \otimes \mathcal{Y} = \mathcal{X} \otimes_{1,2,3}^{1,2,3} \mathcal{Y} \in \mathbb{C}^{R_1 I_1 \times R_2 I_2 \times R_3 I_3}. \tag{2.41}$$

The proposed SKP operator will be later used, in Chapter 4, to derive a tensor-based model for the received signal, where the transmitted data is estimated.

Inspired by the work [39], in Figs. 2.2 to 2.5 we illustrate the above operations using a graph representation.

Figure 2.2 – Graph illustrations of tensor slices, unfoldings, and generalized unfolding.

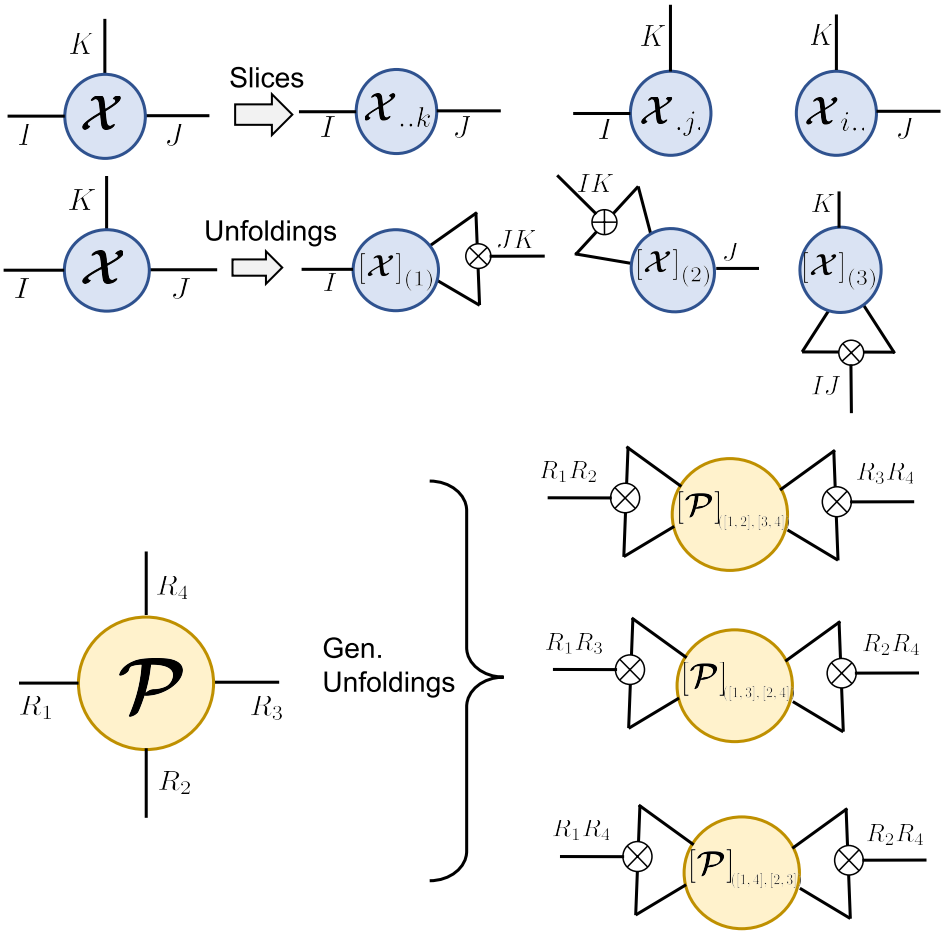

Source: Created by the author.

Figure 2.3 – Graph illustrations of tensor n-mode product and tensor double contraction.

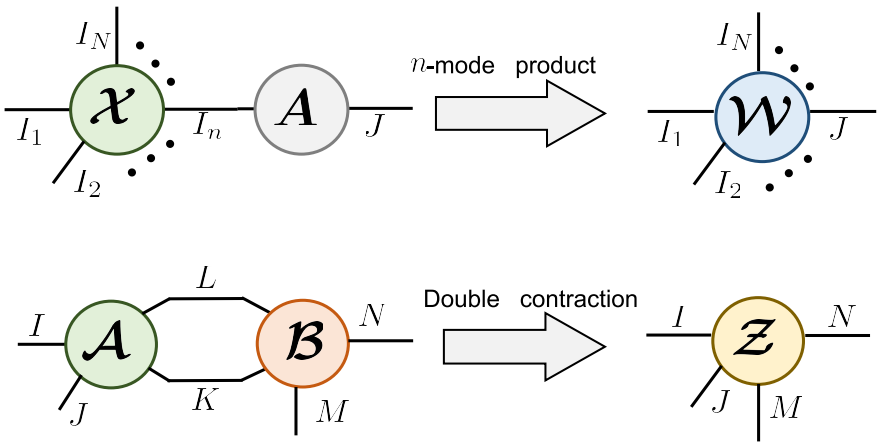

Source: Created by the author.

Figure 2.4 – Graph illustrations of tensor outer and Kronecker product.

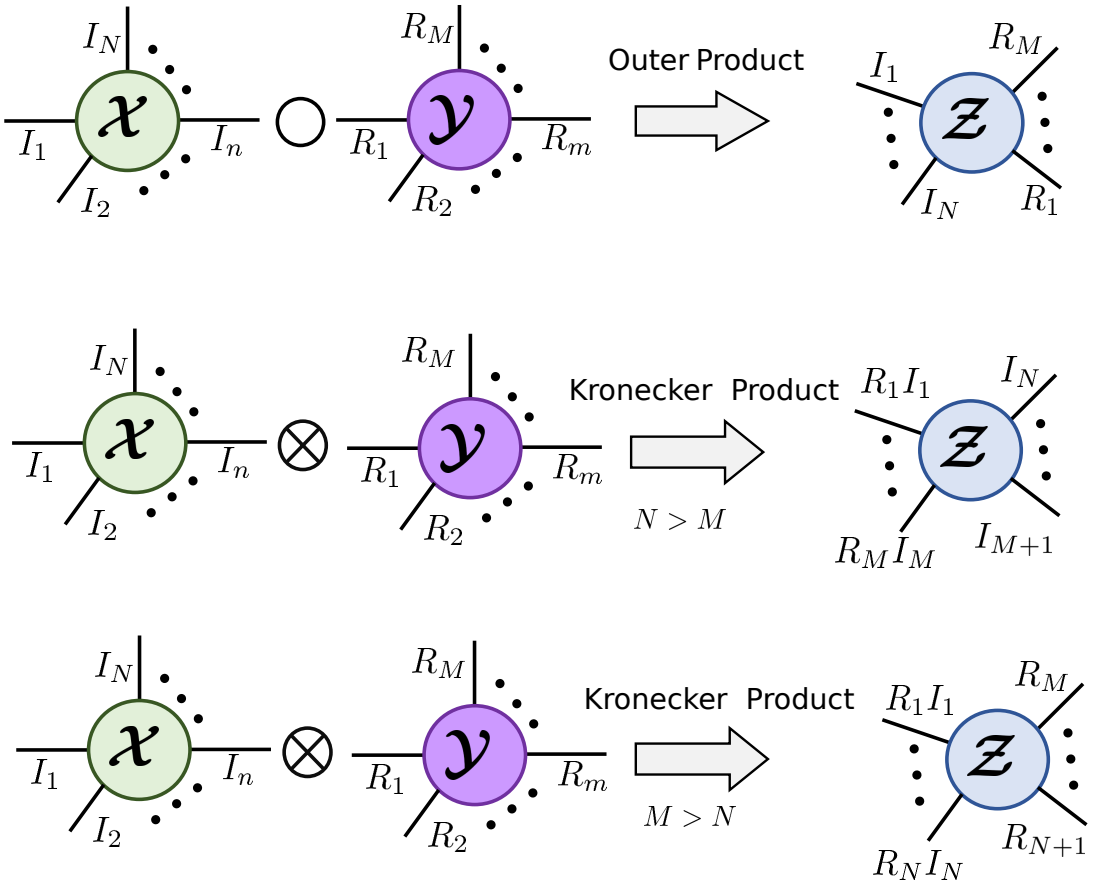

Source: Created by the author.

Figure 2.5 – Graph illustrations of some examples of the SKP.

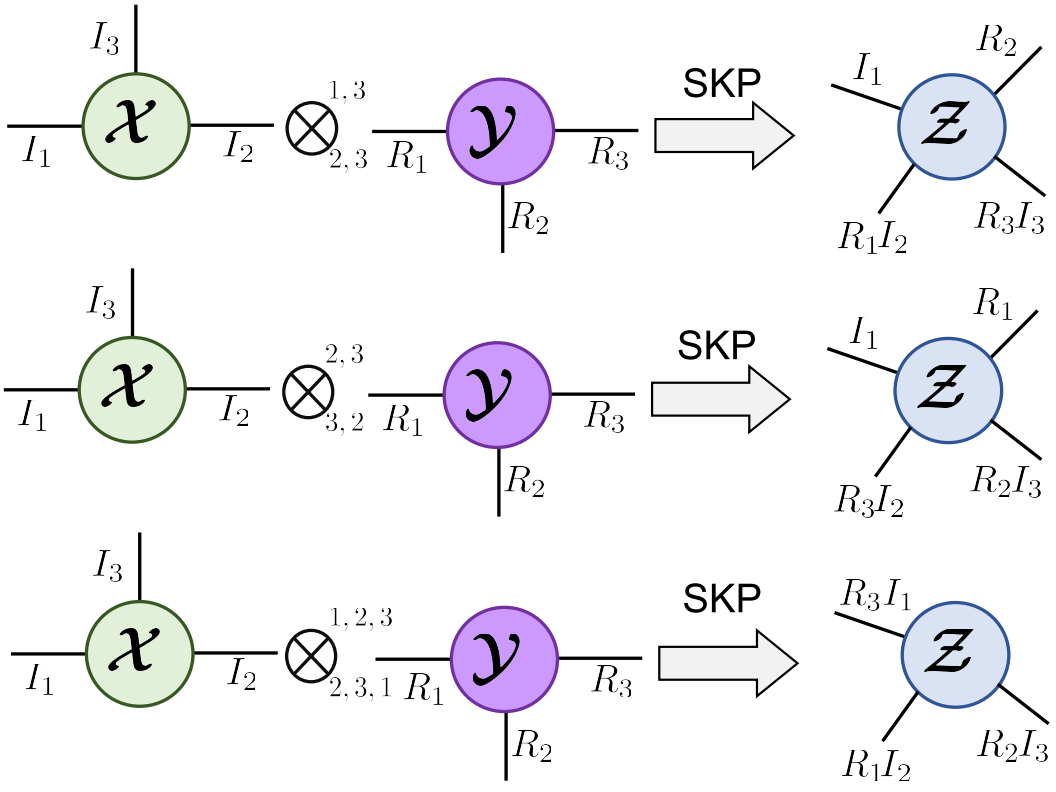

Source: Created by the author.

2.2.10 Rank-One Tensors

A N-th order rank-one tensor is denoted by the outer product of N vectors. Consider a set of N vectors $\boldsymbol{s}^{(n)} \in \mathbb{C}^{I_n \times 1}$, for $n = \{1, \ldots, N\}$, we can define the rank-one tensor $\mathcal{S} \in \mathbb{C}^{I_1 \times \ldots \times I_N}$ as

$$\mathcal{S} = \boldsymbol{s}^{(1)} \circ \boldsymbol{s}^{(2)} \circ \ldots \circ \boldsymbol{s}^{(N)}. \tag{2.42}$$

The n-th mode unfolding of $\mathcal{S}$, is a rank-one matrix denoted by $[\mathcal{S}]_{(n)} \in \mathbb{C}^{I_n \times I_1 \cdots I_{n-1} I_{n+1} \cdots I_N}$ and is given by

$$[\mathcal{S}]_{(n)} = \boldsymbol{s}^{(n)} \left(\boldsymbol{s}^{(N)} \otimes \ldots \otimes \boldsymbol{s}^{(n+1)} \otimes \boldsymbol{s}^{(n-1)} \otimes \ldots \otimes \boldsymbol{s}^{(1)} \right)^{\mathrm{T}}. \tag{2.43}$$

The vectorization of $\mathcal{S}$ is defined as $\mathrm{vec}\,(\mathcal{S}) = \boldsymbol{s} \in \mathbb{C}^{I_1 I_2 \cdots I_N \times 1}$ and by generalizing Propery 2.14, is given by

$$\boldsymbol{s} = \boldsymbol{s}^{(N)} \otimes \ldots \otimes \boldsymbol{s}^{(2)} \otimes \boldsymbol{s}^{(1)}. \tag{2.44}$$

2.2.11 Tensorization

The tensorization operation consists of mapping the elements of a vector into a higher order tensor. Let us define the vector $\boldsymbol{y} \in \mathbb{C}^{N \times 1}$, in which $N = \prod_{p=1}^{P} N_p$, where N_p is the size of the p-th partition of this vector. By applying the tensorization operator, defined as $\mathcal{T}\{\cdot\}$, we can form a P-th order tensor $\mathcal{Y} = \mathcal{T}\{\boldsymbol{y}\} \in \mathbb{C}^{N_1 \times N_2 \times \ldots \times N_P}$. The mapping of elements from $\mathcal{Y}$ to $\boldsymbol{y}$ is defined as

$$\mathcal{Y}_{n_1, n_2, \ldots, n_P} = \boldsymbol{y}_n, \tag{2.45}$$

where $n = \{1, \ldots, N_1, \ldots N_1 N_2, \ldots N_1 N_2 \cdots N_P\}$, for $p = \{1, \ldots, P\}$. For example considering the vector $\boldsymbol{s}$, given in (2.44), and applying the tensorization operator, we have the N-th order rank-one tensor $\mathcal{S} = \mathcal{T}\{\boldsymbol{s}\} \in \mathbb{C}^{I_1 \times I_2 \times \ldots \times N_P}$ given in (2.42). In other words, we have the following properties

$$\mathcal{S} = \mathcal{T}\{\boldsymbol{s}\} = \boldsymbol{s}^{(1)} \circ \boldsymbol{s}^{(2)} \circ \ldots \circ \boldsymbol{s}^{(N)} \in \mathbb{C}^{I_1 \times I_2 \times \ldots \times I_P} \tag{2.46}$$

$$\boldsymbol{s} = \mathrm{vec}\,(\mathcal{S}) = \boldsymbol{s}^{(N)} \otimes \ldots \otimes \boldsymbol{s}^{(2)} \otimes \boldsymbol{s}^{(1)} \in \mathbb{C}^{I_1 I_2 \cdots I_P}. \tag{2.47}$$

2.3 Tensor Decompositions

In the past two decades several tensor decompositions were proposed in the signal processing community. Some of these decomposition are Nested PARAFAC [29], Nested Tucker [28], PARATUck [27], Tensor-Train [30]. However, most of these decompositions are special cases or combinations of the PARAFAC [25] and Tucker [26, 41] decompositions. In this section, we review the PARAFAC and the Tucker decompositions and the classical algorithms in the literature that can be used to compute each decomposition.

Figure 2.6 – Illustration of a third-order PARAFAC tensor as a sum of R rank-one tensors.

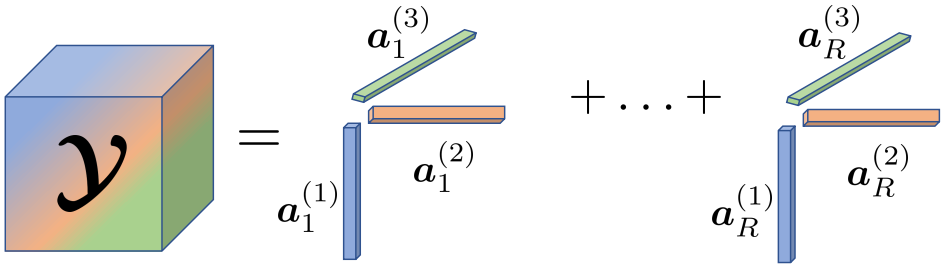

Source: Created by the author.

Figure 2.7 – Illustration of a third-order PARAFAC tensor as a combination of its factor matrices and an identity tensor.

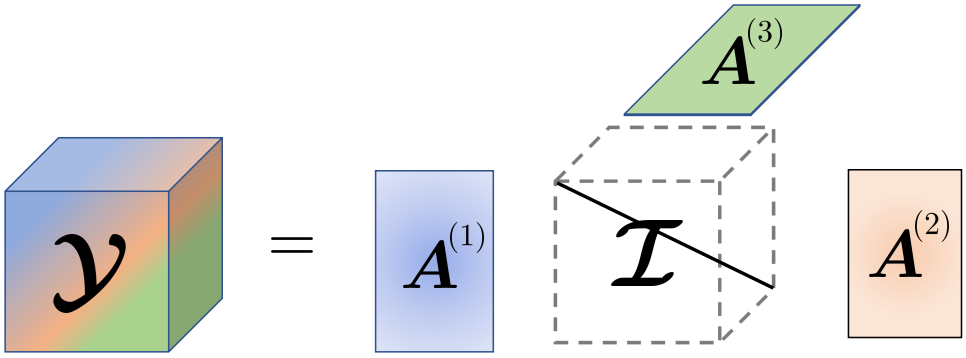

Source: Created by the author.

2.3.1 PARAFAC Decomposition

Any matrix of rank R can be expressed by the summation of its rank-one components, e.g., singular value decomposition (SVD). In the case of tensors, a tensor of rank R is given by the summation of its rank-one tensors components. This decomposition is called PARAFAC [25]. For a P-th order tensor $\mathcal{Y} \in \mathbb{C}^{I_1 \times I_2 \times \ldots \times I_P}$, its PARAFAC decomposition is given as

$$\mathcal{Y} = \sum_{r=1}^{R} \boldsymbol{a}_r^{(1)} \circ \boldsymbol{a}_r^{(2)} \circ \ldots \circ \boldsymbol{a}_r^{(P)} \in \mathbb{C}^{I_1 \times I_2 \times \ldots \times I_P}, \tag{2.48}$$

$$\mathcal{Y} = \mathcal{I}_{P,R} \times_1 \boldsymbol{A}^{(1)} \times_2 \boldsymbol{A}^{(2)} \times \ldots \times \boldsymbol{A}^{(P)}. \tag{2.49}$$

where $\boldsymbol{a}_r^{(p)} \in \mathbb{C}^{I_p \times 1}$, is the column of the p-th factor matrix $\boldsymbol{A}^{(p)} \in \mathbb{C}^{I_p \times R}$, for $p = \{1, \ldots, P\}$, and $\mathcal{I}_{P,R} \in \mathbb{R}^{R \times R \times \ldots \times R}$ is the P-th order indentity tensor. The p-th mode unfolding of $\mathcal{Y}$, defined as $[\mathcal{Y}]_{(p)}$, is expressed as

$$[\mathcal{Y}]_{(p)} = \boldsymbol{A}^{(p)} \left(\boldsymbol{A}^{(P)} \diamond \ldots \diamond \boldsymbol{A}^{(p+1)} \diamond \boldsymbol{A}^{(p-1)} \diamond \ldots \diamond \boldsymbol{A}^{(1)} \right)^{\mathrm{T}} \in \mathbb{C}^{I_p \times I_1 \cdots I_{p-1} I_{p+1} \cdots I_P}. \tag{2.50}$$

Figure 2.6 illustrates a PARAFAC tensor, for $P = 3$, as the summation of rank-one tensors. In this case, the three unfolding matrices of $\mathcal{Y}$, depicted in Figure 2.7, are given by

$$[\mathcal{Y}]_{(1)} = \boldsymbol{A}^{(1)} \left[\mathcal{I}_{3,R}\right]_{(1)} \left(\boldsymbol{A}^{(3)} \otimes \boldsymbol{A}^{(2)}\right)^{\mathrm{T}} \in \mathbb{C}^{I_1 \times I_2 I_3}, \tag{2.51}$$

$$[\mathcal{Y}]_{(2)} = \boldsymbol{A}^{(2)} \left[\mathcal{I}_{3,R}\right]_{(2)} \left(\boldsymbol{A}^{(3)} \otimes \boldsymbol{A}^{(1)}\right)^{\mathrm{T}} \in \mathbb{C}^{I_2 \times I_1 I_3}, \tag{2.52}$$

$$[\mathcal{Y}]_{(3)} = \boldsymbol{A}^{(3)} \left[\mathcal{I}_{3,R}\right]_{(3)} \left(\boldsymbol{A}^{(2)} \otimes \boldsymbol{A}^{(1)}\right)^{\mathrm{T}} \in \mathbb{C}^{I_3 \times I_1 I_2}. \tag{2.53}$$

where $\left[\mathcal{I}_{3,R}\right]_{(p)} \in \mathbb{C}^{R \times RR}$ is the p-th mode unfolding of $\mathcal{I}$, for $p = \{1,2,3\}$. As discussed in Section 2.2.5, we have that $\left[\mathcal{I}_{3,R}\right]_{(1)} = \left[\mathcal{I}_{3,R}\right]_{(2)} = \left[\mathcal{I}_{3,R}\right]_{(3)}$, are column selection matrices. Based on this, we can replace these matrices with the identity matrix $\boldsymbol{I}_R \in \mathbb{R}^{R \times R}$ while replacing the Kronecker operator $\otimes$ with the Khatri-Rao operator $\diamond$. We have that

$$[\mathcal{Y}]_{(1)} = \boldsymbol{A}^{(1)} \left(\boldsymbol{A}^{(3)} \diamond \boldsymbol{A}^{(2)}\right)^{\mathrm{T}} \in \mathbb{C}^{I_1 \times I_2 I_3}, \tag{2.54}$$

$$[\mathcal{Y}]_{(2)} = \boldsymbol{A}^{(2)} \left(\boldsymbol{A}^{(3)} \diamond \boldsymbol{A}^{(1)}\right)^{\mathrm{T}} \in \mathbb{C}^{I_2 \times I_1 I_3}, \tag{2.55}$$

$$[\mathcal{Y}]_{(3)} = \boldsymbol{A}^{(3)} \left(\boldsymbol{A}^{(2)} \diamond \boldsymbol{A}^{(1)}\right)^{\mathrm{T}} \in \mathbb{C}^{I_3 \times I_1 I_2}. \tag{2.56}$$

In addition, for the third order PARAFAC tensor, illustrated in Fig. 2.6, we can express its frontal slices in function of its factor matrices as

$$\mathcal{Y}_{..i_3} = \boldsymbol{A} \mathrm{diag}_{i_3}\left(\boldsymbol{A}^{(3)}\right) \boldsymbol{A}^{(2)\mathrm{T}} \in \mathbb{C}^{I_1 \times I_2}, \tag{2.57}$$

where $\mathrm{diag}_{i_3}\left(\boldsymbol{A}^{(3)}\right) \in \mathbb{C}^{R \times R}$ is the diagonal matrix formed by diagonalizing the i_3-th row of $\boldsymbol{A}^{(3)}$, for $i_3 = \{1, \ldots, I_3\}$.

2.3.1.1 Uniqueness

Matrix products are not unique since if we have $\boldsymbol{C} = \boldsymbol{AB}$, we also have that $\boldsymbol{C} = \boldsymbol{ATT}^{-1}\boldsymbol{B}$, with $\boldsymbol{T}$ being a non-singular matrix. The SVD is unique under the singular matrix orthogonality constraint. Unlike matrix product, the uniqueness property often comes easily in a higher-order PARAFAC tensors. In other words, uniqueness means that the rank-one tensor sum given (2.48) is the only possible combination to generate $\mathcal{Y}$, with the exception to some permutation and scaling factors, i.e., we can rewrite (2.49) as

$$\mathcal{Y} = \mathcal{I}_{3,R} \times_1 \boldsymbol{A}^{(1)} \Pi \Delta_1 \times_2 \boldsymbol{A}^{(2)} \Pi \Delta_2 \times_3 \boldsymbol{A}^{(2)} \Pi \Delta_3, \tag{2.58}$$

where Π is a permutation matrix and Δ_i, for $i = \{1,2,3\}$, is a scaling diagonal matrix, with $\Delta_1 \Delta_2 \Delta_3 = \boldsymbol{I}_R$. For third-order tensors, Kruskal [24] derived a not necessary but sufficient condition for uniqueness. The author define the k-rank of a matrix as the maximum value of columns that are linearly independents. Denoting as $k_{\boldsymbol{A}^{(1)}}$, $k_{\boldsymbol{A}^{(2)}}$ and $k_{\boldsymbol{A}^{(3)}}$ as the k-rank of $\boldsymbol{A}^{(1)}$, $\boldsymbol{A}^{(2)}$, and $\boldsymbol{A}^{(3)}$, the PARAFAC decomposition in (2.48) is unique if

$$k_{\boldsymbol{A}^{(1)}} + k_{\boldsymbol{A}^{(2)}} + k_{\boldsymbol{A}^{(3)}} \geq 2R + 2. \tag{2.59}$$

This condition was further generalized in [42] to N-th order PARAFAC tensor, by

$$\sum_{n=1}^{N} k_{\mathbf{A}^{(n)}} \geq 2R + (N-1). \tag{2.60}$$

2.3.1.2 Alternating Least Squares Estimation

In literature, the ALS (Alternating Least-Squares) algorithm is a classical algorithm originally proposed by Carrol, Chang, and Harshaman [25] to estimate the tensor factor matrices by solving multiple least squares (LS) problems in a iterative way [23, 43, 44, 45]. For example, let us consider the following third order PARAFAC tensor

$$\mathcal{X} = \mathcal{I}_{3,R} \times_1 \boldsymbol{A} \times_2 \boldsymbol{B} \times_3 \boldsymbol{C} \in \mathbb{C}^{I \times J \times K}, \tag{2.61}$$

where $\boldsymbol{A} \in \mathbb{C}^{I \times R}$, $\boldsymbol{B} \in \mathbb{C}^{J \times R}$, and $\boldsymbol{C} \in \mathbb{C}^{K \times R}$ are the factor matrices. To estimate $\mathcal{X}$ we solve the following problem

$$\min_{\hat{\mathcal{X}}} \left\| \mathcal{X} - \hat{\mathcal{X}} \right\|_{\mathrm{F}}^2, \tag{2.62}$$

the alternating least squares (ALS) algorithm recast the above minimization problem into three LS problems as

$$\min_{\hat{\boldsymbol{A}}} \left\| [\mathcal{X}]_{(1)} - \hat{\boldsymbol{A}} \left(\boldsymbol{C} \diamond \boldsymbol{B} \right)^{\mathrm{T}} \right\|_{\mathrm{F}}^2, \tag{2.63}$$

$$\min_{\hat{\boldsymbol{B}}} \left\| [\mathcal{X}]_{(2)} - \hat{\boldsymbol{B}} \left(\boldsymbol{C} \diamond \hat{\boldsymbol{A}} \right)^{\mathrm{T}} \right\|_{\mathrm{F}}^2, \tag{2.64}$$

$$\min_{\hat{\boldsymbol{C}}} \left\| [\mathcal{X}]_{(3)} - \hat{\boldsymbol{C}} \left(\hat{\boldsymbol{B}} \diamond \boldsymbol{A} \right)^{\mathrm{T}} \right\|_{\mathrm{F}}^2, \tag{2.65}$$

which the solutions are, respectively, given by

$$\hat{\boldsymbol{A}} = [\mathcal{X}]_{(1)} \left[\left(\boldsymbol{C} \diamond \boldsymbol{B} \right)^{\mathrm{T}} \right]^{+} \in \mathbb{C}^{I \times JK}, \tag{2.66}$$

$$\hat{\boldsymbol{B}} = [\mathcal{X}]_{(2)} \left[\left(\boldsymbol{C} \diamond \hat{\boldsymbol{A}} \right)^{\mathrm{T}} \right]^{+} \in \mathbb{C}^{J \times IK}, \tag{2.67}$$

$$\hat{\boldsymbol{C}} = [\mathcal{X}]_{(3)} \left[\left(\hat{\boldsymbol{B}} \diamond \hat{\boldsymbol{A}} \right)^{\mathrm{T}} \right]^{+} \in \mathbb{C}^{K \times IK}. \tag{2.68}$$

The algorithm starts with problem (2.63) by randomly initializing the matrices $\boldsymbol{B}$ and $\boldsymbol{C}$ and solving it using (2.66). For problem (2.64), the solution for $\hat{\boldsymbol{A}}$ is plugged in (2.64) which is solved using (2.67). Finally, for the last LS problem, the solutions of problems (2.66) and (2.67) are plugged into (2.65), and the problem is solved in (2.68), finalizing the first iteration of the ALS algorithm. The process is repeated until reaches at pre-determined number of iterations, or achieves a convergence threshold.

Generalizing to the N-th order PARAFAC tensor, $\mathcal{Y}$, given in (2.49), the ALS algorithm solves the following problem, for $p = \{1, \ldots, P\}$,

$$\min_{\hat{\boldsymbol{A}}^{(p)}} \left\| [\mathcal{Y}]_{(p)} - \hat{\boldsymbol{A}}^{(p)} \left(\boldsymbol{A}^{(P)} \diamond \ldots \diamond \boldsymbol{A}^{(p+1)} \diamond \boldsymbol{A}^{(p-1)} \diamond \ldots \diamond \boldsymbol{A}^{(1)} \right)^{\mathrm{T}} \right\|_{\mathrm{F}}^2, \tag{2.69}$$

with solution given by

$$\hat{\boldsymbol{A}}^{(p)} = [\boldsymbol{\mathcal{Y}}]_{(p)} \left(\left(\boldsymbol{A}^{(P)} \diamond \ldots \diamond \boldsymbol{A}^{(p+1)} \diamond \boldsymbol{A}^{(p-1)} \diamond \ldots \diamond \boldsymbol{A}^{(1)} \right)^{\mathrm{T}} \right)^{+}. \tag{2.70}$$

The ALS algorithm for a P-th order PARAFAC tensor is summarized in Algorithm 1.

Algorithm 1 PARAFAC ALS

1: **Inputs**: Tensor $\boldsymbol{\mathcal{Y}}$, R
2: Initialize the matrices $\hat{\boldsymbol{A}}_0^{(2)}, \ldots, \hat{\boldsymbol{A}}_0^{(P)}$. Iteration i = 0.
3: Define a maximum number of iteration I.
4: **for** $i = 1 : I$ **do**
5: **for** $p = 1 : P$ **do**
6: Compute an estimate of the p-th factor matrix $\boldsymbol{A}_{\mathrm{i}}^{(p)}$ as

$$\hat{\boldsymbol{A}}_i^{(p)} = [\boldsymbol{\mathcal{Y}}]_{(p)} \left(\left(\hat{\boldsymbol{A}}_{i-1}^{(P)} \diamond \ldots \diamond \hat{\boldsymbol{A}}_{i-1}^{(p+1)} \diamond \hat{\boldsymbol{A}}_{i-1}^{(p-1)} \diamond \ldots \diamond \hat{\boldsymbol{A}}_{i-1}^{(1)} \right)^{\mathrm{T}} \right)^{+}$$

7: **end for**
8: **end for**
9: Return $\hat{\boldsymbol{A}}^{(1)}, \ldots, \hat{\boldsymbol{A}}^{(P)}$.

Note that, the factor matrices output of the ALS algorithm, in Algorithm 1, are a permuted and scaled versions of the true matrices. In other words, we have the following relationship

$$\hat{\boldsymbol{A}}^{(p)} = \boldsymbol{A}^{(p)} \Pi \Delta_p \in \mathbb{C}^{I_p \times R}, \tag{2.71}$$

with $\prod_{p=1}^{P} \Delta_p = \boldsymbol{I}_R$.

2.3.1.3 Rank-One Estimation

For the case where $R = 1$, we have a rank-one tensor, as defined in Section 2.2.10. In this case, (2.48) becomes

$$\boldsymbol{\mathcal{Y}} = \boldsymbol{a}^{(1)} \circ \boldsymbol{a}^{(2)} \circ \ldots \circ \boldsymbol{a}^{(P)} \in \mathbb{C}^{I_1 \times I_2 \times \ldots \times I_P}. \tag{2.72}$$

Instead of using the ALS algorithm to estimate the factors, we can perform a rank-one HOSVD [41]. From the fact that each unfolding of $\boldsymbol{\mathcal{Y}}$ is a rank-one matrix (see (2.43)), each factor can be estimated by computing the SVD of each unfolding. In other words, we compute P independents SVDs. The rank-one HOSVD algorithm is summarized in Algorithm 2. Note that, since $R = 1$ there is no permutation matrix affecting the output, only a scaling ambiguity is present, i.e., the estimated factors are related to the true factors as $\hat{\boldsymbol{a}}^{(p)} = \alpha_p \boldsymbol{a}$, for $p = \{1, \ldots, P\}$, with $\prod_{p=1}^{P} \alpha_p = 1$.

Algorithm 2 Rank-One HOSVD

1: **Input**: $\mathcal{Y}$
2: **for** $p = 1 : P$ **do**
3: Compute the SVD of the p-mode unfolding of $\mathcal{Y}$ as

$$[\mathcal{Y}]_{(p)} = \boldsymbol{U}^{(p)} \Sigma^{(p)} \boldsymbol{V}^{(p)\mathrm{H}}.$$

4: Set an estimation of $\boldsymbol{a}^{(p)}$ by truncating the left singular matrix to its first

$$\hat{\boldsymbol{a}}^{(p)} = \boldsymbol{u}_{:1}^{(p)} (\sigma)^{1/P}.$$

5: **end for**
6: Return $\hat{\boldsymbol{a}}^{(1)}, \ldots, \hat{\boldsymbol{a}}^{(P)}$.

Figure 2.8 – Illustration of a third order Tucker tensor and its factor matrices and core tensor.

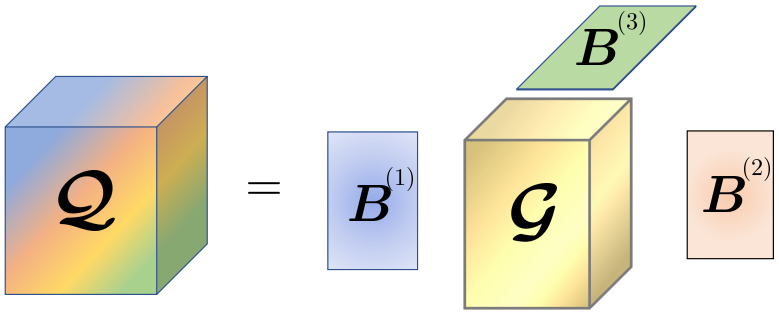

Source: Created by the author.

2.3.2 Tucker Decomposition

The Tucker decomposition was originally proposed by Tucker in 1964 [26]. It consist of a tensor compression or expansion and expresses a tensor as a set of factor matrices and a core tensor. A P-th order tensor $\mathcal{Q} \in \mathbb{C}^{I_1 \times \ldots \times I_P}$ that admits a Tucker decomposition, can be written as

$$\mathcal{Q} = \mathcal{G} \times_1 \boldsymbol{B}^{(1)} \times_2 \ldots \times_P \boldsymbol{B}^{(P)} \in \mathbb{C}^{I_1 \times \ldots \times I_P}, \tag{2.73}$$

where $\boldsymbol{B}^{(p)} \in \mathbb{C}^{I_p \times R_p}$ is the p-th factor matrix, for $p = \{1, \ldots, P\}$, and $\mathcal{G} \in \mathbb{C}^{R_1 \times \ldots \times R_P}$ is the core tensor. The tensor $\mathcal{Q}$ can also be represented as the outer product of its factors, given as

$$\mathcal{Q} = \sum_{r_1=1}^{R_1} \ldots \sum_{r_P=1}^{R_P} \mathcal{G}_{r_1,\ldots,r_P} \left(\boldsymbol{b}_{r_1}^{(1)} \circ \ldots \circ \boldsymbol{b}_{r_P}^{(P)} \right),$$

where $\boldsymbol{b}^{(p)} \in \mathbb{C}^{I_p \times 1}$ is the r_p-th column of the p-th factor matrix $\boldsymbol{B}^{(p)} \in \mathbb{C}^{I_p \times R_p}$, for $p = \{1, \ldots, P\}$ and $r_p = \{1, \ldots, R_p\}$. The p-th mode unfolding matrix of $\mathcal{Q}$, defined as $[\mathcal{Q}]_{(p)} \in \mathbb{C}^{N_p \times N_1 \cdots N_{p-1} N_{p+1} \cdots N_P}$, is given by

$$[\mathcal{Q}]_{(p)} = \boldsymbol{B}^{(p)} [\mathcal{G}]_{(p)} \left(\boldsymbol{B}^{(P)} \otimes \ldots \otimes \boldsymbol{B}^{(p+1)} \otimes \boldsymbol{B}^{(p-1)} \otimes \ldots \otimes \boldsymbol{B}^{(1)} \right)^{\mathrm{T}}. \tag{2.74}$$

Algorithm 3 HOSVD

1: Set the unfoldings ranks $R_1, \ldots, R_P$
2: **for** $p = 1 : P$ **do**
3: Compute the SVD of the p-mode unfolding of $\mathcal{Q}$ as

$$[\mathcal{Q}]_{(p)} = \boldsymbol{U}^{(p)} \Sigma^{(p)} \boldsymbol{V}^{(p)\mathrm{H}}.$$

4: Set an estimation of $\boldsymbol{B}^{(p)}$ by truncating the left singular matrix to its first R_p columns

$$\hat{\boldsymbol{B}}^{(p)} = \boldsymbol{U}^{(p)}_{:,1:R_p}.$$

5: **end for**
6: Compute an estimate of the core tensor $\boldsymbol{g} = \mathrm{vec}\,(\mathcal{G})$ as

$$\hat{\boldsymbol{g}} = \left(\hat{\boldsymbol{B}}^{(P)\mathrm{H}} \otimes \ldots \otimes \hat{\boldsymbol{B}}^{(1)\mathrm{H}}\right) \mathrm{vec}\,(\mathcal{Q}).$$

7: Define $\hat{\mathcal{G}} = \mathcal{T}\{\hat{\boldsymbol{g}}\}$.
8: Return $\hat{\boldsymbol{B}}^{(1)}, \ldots, \hat{\boldsymbol{B}}^{(P)}$ and $\hat{\mathcal{G}}$.

Inversely, the core tensor $\mathcal{G} \in \mathbb{C}^{R_1 \times R_2 \times \ldots \times R_P}$ is given by

$$\mathcal{G} = \mathcal{Q} \times_1 \boldsymbol{B}^{(1)+} \times_2 \boldsymbol{B}^{(2)+} \times_3 \ldots \times_P \boldsymbol{B}^{(P)+}, \tag{2.75}$$

or, using the vec operator, we have

$$\boldsymbol{g} = \left(\boldsymbol{B}^{(P)+} \otimes \ldots \otimes \boldsymbol{B}^{(2)+} \otimes \boldsymbol{B}^{(1)+}\right) \boldsymbol{q}, \tag{2.76}$$

where $\boldsymbol{g} = \mathrm{vec}(\mathcal{G}) \in \mathbb{C}^{R_1 \cdots R_P \times 1}$ and $\boldsymbol{g} = \mathrm{vec}(\mathcal{Q}) \in \mathbb{C}^{I_1 \cdots I_P \times 1}$.

Fig. 2.8, illustrates the Tucker decomposition for the case of $P = 3$. Its three mode unfoldings are given by

$$[\mathcal{Q}]_{(1)} = \boldsymbol{B}^{(1)} [\mathcal{G}]_{(1)} \left(\boldsymbol{B}^{(3)} \otimes \boldsymbol{B}^{(2)}\right)^{\mathrm{T}} \in \mathbb{C}^{I_1 \times I_2 I_3}, \tag{2.77}$$

$$[\mathcal{Q}]_{(2)} = \boldsymbol{B}^{(2)} [\mathcal{G}]_{(2)} \left(\boldsymbol{B}^{(3)} \otimes \boldsymbol{B}^{(1)}\right)^{\mathrm{T}} \in \mathbb{C}^{I_2 \times I_1 I_3}, \tag{2.78}$$

$$[\mathcal{Q}]_{(3)} = \boldsymbol{B}^{(3)} [\mathcal{G}]_{(3)} \left(\boldsymbol{B}^{(2)} \otimes \boldsymbol{B}^{(1)}\right)^{\mathrm{T}} \in \mathbb{C}^{I_3 \times I_1 I_2}, \tag{2.79}$$

while the core tensor is given as

$$\mathcal{G} = \mathcal{Q} \times_1 \boldsymbol{B}^{(1)+} \times_2 \boldsymbol{B}^{(2)+} \times_3 \boldsymbol{B}^{(2)+}, \tag{2.80}$$

$$\boldsymbol{g} = \left(\boldsymbol{B}^{(3)+} \otimes \boldsymbol{B}^{(2)+} \otimes \boldsymbol{B}^{(1)+}\right) \boldsymbol{q}. \tag{2.81}$$

2.3.2.1 HOSVD Algorithm

For a Tucker decomposition, the factor matrices and the core tensor are usually estimated using the HOSVD algorithm [46], which boils down to computing multiple (indepen-

dent) SVDs, one for each unfolding of the tensor $\mathcal{Q}$ [23, 46]. The HOSVD is summarized in Algorithm 3.

2.3.2.2 Uniqueness

The Tucker decomposition is not unique from the fact that, as in matrices, we can apply any transformation in the core tensor without changing the tensor fit [23]. However, as shown in [28], if the core tensor is known, then the Tucker decomposition is unique.

Proof.
Let us consider the Tucker tensor in (2.73), its vectorization is given by

$$\text{vec}\left(\mathcal{Q}\right) = \left(\boldsymbol{B}^{(P)} \otimes \ldots \otimes \boldsymbol{B}^{(2)} \otimes \boldsymbol{B}^{(1)}\right) \text{vec}\left(\mathcal{G}\right). \tag{2.82}$$

Replacing $\boldsymbol{B}^{(p)}$ for $\boldsymbol{B}^{(p)}\boldsymbol{Z}^{(p)}$, for $p = \{1, \ldots, P\}$, and applying Property (2.10), we have that

$$\text{vec}\left(\mathcal{Q}\right) = \left(\boldsymbol{B}^{(P)}\boldsymbol{Z}^{(P)} \otimes \ldots \otimes \boldsymbol{B}^{(2)}\boldsymbol{Z}^{(2)} \otimes \boldsymbol{B}^{(1)}\boldsymbol{Z}^{(1)}\right) \text{vec}\left(\mathcal{G}\right) \tag{2.83}$$

$$= \left(\boldsymbol{B}^{(P)} \otimes \ldots \otimes \boldsymbol{B}^{(2)} \otimes \boldsymbol{B}^{(1)}\right) \left(\boldsymbol{Z}^{(P)} \otimes \ldots \otimes \boldsymbol{Z}^{(2)} \otimes \boldsymbol{Z}^{(1)}\right) \text{vec}\left(\mathcal{G}\right), \tag{2.84}$$

the expressions in (2.82) and (2.84) are equal only if the core tensor $\mathcal{G}$ is known, and

$$\left(\boldsymbol{Z}^{(P)} \otimes \ldots \otimes \boldsymbol{Z}^{(2)} \otimes \boldsymbol{Z}^{(1)}\right) = \boldsymbol{I}_{R_1 \cdots R_P}.$$

This is equivalent to have $\boldsymbol{Z}^{(p)} = \alpha_p \boldsymbol{I}_{R_p}$, for $p = \{1, \ldots, P\}$, with α_p being a scaling factor, and $\prod_{p=1}^{P} \alpha_p = 1$. In other words, if the core tensor of a Tucker decomposition is known, then its factor matrices are unique under a scaling factor ambiguity.

2.4 Kronecker Product Factorization

Let us assume a matrix $\boldsymbol{X} = \boldsymbol{A} \otimes \boldsymbol{B} + \boldsymbol{N} \in \mathbb{C}^{I_2 I_1 \times R_2 R_1}$, where $\boldsymbol{A} \in \mathbb{C}^{I_1 \times R_1}$, $\boldsymbol{B} \in \mathbb{C}^{I_2 \times R_2}$, and $\boldsymbol{N}$ is a noise matrix. The problem consist of finding an optimal estimation of $\boldsymbol{A}$ and $\boldsymbol{B}$ based on the observation $\boldsymbol{X}$, i.e.,

$$\min_{\boldsymbol{A},\boldsymbol{B}} ||\boldsymbol{X} - \boldsymbol{A} \otimes \boldsymbol{B}||_{\text{F}}^2. \tag{2.85}$$

The authors of [47] proposed to recast the problem (2.85) into a rank-one approximation problem, i.e.,

$$\min_{\boldsymbol{A},\boldsymbol{B}} \left|\left|\bar{\boldsymbol{X}} - \text{vec}\left(\boldsymbol{B}\right) \circ \text{vec}\left(\boldsymbol{A}\right)\right|\right|_{\text{F}}^2, \tag{2.86}$$

where $\bar{\boldsymbol{X}} \in \mathbb{C}^{I_2 R_2 \times I_1 R_1}$ is a rearranged version of $\boldsymbol{X} \in \mathbb{C}^{I_2 I_1 \times R_2 R_1}$. This is possible since the Kronecker product by its nature is a block-wise product. Thus, rearranging the elements of these blocks yields a rank-one structure. This process is illustrated in Fig. 2.9.

Figure 2.9 – Illustration the rearranging of elements of matrix $\boldsymbol{X}$ into $\bar{\boldsymbol{X}}$.

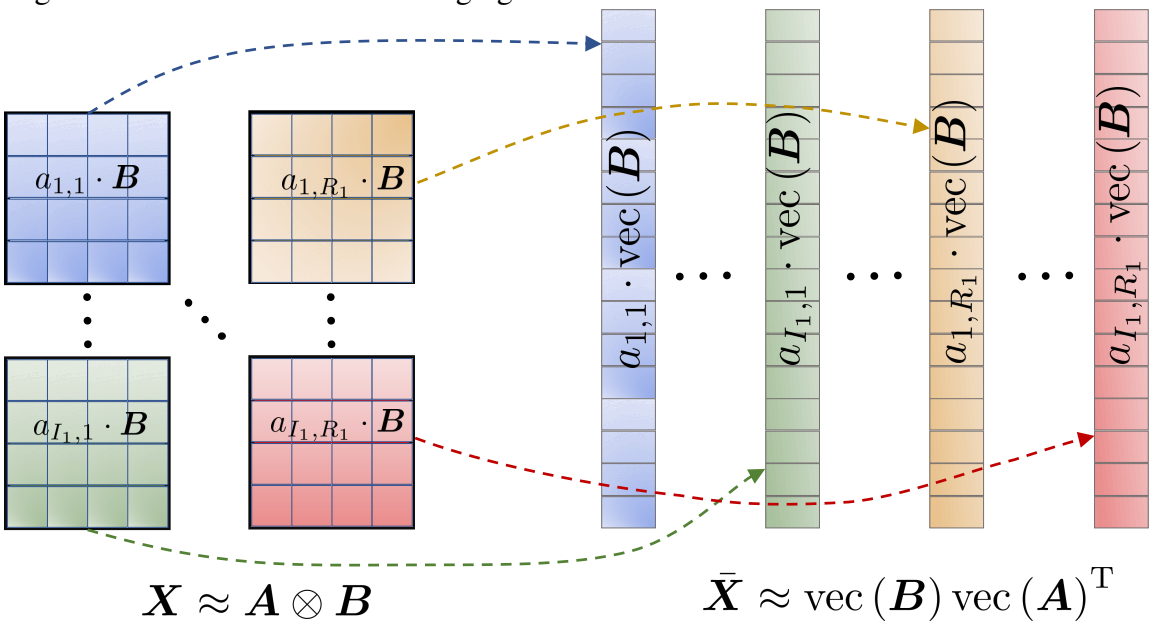

Source: Created by the author.

In fact, to obtain an optimal estimation of the factors $\boldsymbol{A}$ and $\boldsymbol{B}$ we can compute the SVD of $\bar{\boldsymbol{X}}$ as $\boldsymbol{U}\Sigma\boldsymbol{V}^{\mathrm{H}}$ and define the factor estimations as

$$\mathrm{vec}\left(\hat{\boldsymbol{B}}\right) = \sqrt{\sigma_1}\boldsymbol{u}_{.1}, \tag{2.87}$$

$$\mathrm{vec}\left(\hat{\boldsymbol{A}}\right) = \sqrt{\sigma_1}\boldsymbol{v}^{*}_{.1}, \tag{2.88}$$

where σ_1 is the largest singular value of $\bar{\boldsymbol{X}}$. Nevertheless, due to the SVD, the estimations on (2.87) and (2.88) are only basis to the real factors, i.e., $\mathrm{vec}\left(\hat{\boldsymbol{B}}\right) = \alpha\mathrm{vec}\left(\boldsymbol{B}\right)$, and $\mathrm{vec}\left(\hat{\boldsymbol{A}}\right) = \frac{1}{\alpha}\mathrm{vec}\left(\boldsymbol{A}\right)$, where α is a scaling factor ambiguity. Thus, one element of $\boldsymbol{A}$ or $\boldsymbol{B}$ must be known *a priori* in order to remove this ambiguity, i.e., $\alpha = \boldsymbol{B}_{1,1}/\hat{\boldsymbol{B}}_{1,1}$, or $\frac{1}{\alpha} = \boldsymbol{A}_{1,1}/\hat{\boldsymbol{A}}_{1,1}$.

The problem in (2.85) can be extended to the case that we have N matrices. Let us consider that we have $\boldsymbol{X} = \boldsymbol{A}^{(N)} \otimes \ldots \otimes \boldsymbol{A}^{(1)} + \boldsymbol{N} \in \mathbb{C}^{I_1 \cdots I_N \times R_1 \cdots R_N}$, where $\boldsymbol{A}^{(n)} \in \mathbb{C}^{I_n \times R_n}$, for $n = \{1, \ldots, N\}$ is the n-th factor matrix. We can rewrite the minimization problem in (2.85) as

$$\min_{\boldsymbol{A}^{(N)},\ldots,\boldsymbol{A}^{(1)}} \left\| \boldsymbol{X} - \boldsymbol{A}^{(N)} \otimes \ldots \otimes \boldsymbol{A}^{(1)} \right\|_{\mathrm{F}}^{2}. \tag{2.89}$$

In this case, instead of rearranging the elements of $\boldsymbol{X}$ as a rank-one matrix, we rearrange it as a N-th order rank-one tensor $\bar{\mathcal{X}} \in \mathbb{C}^{I_1 R_1 \times I_2 R_2 \times \ldots \times I_N R_N}$. The problem in (2.91) becomes

$$\min_{\boldsymbol{a}^{(N)},\ldots,\boldsymbol{a}^{(1)}} \left\| \bar{\mathcal{X}} - \boldsymbol{a}^{(1)} \circ \boldsymbol{a}^{(2)} \circ \ldots \circ \boldsymbol{a}^{(N)} \right\|_{\mathrm{F}}^{2}, \tag{2.90}$$

where $\boldsymbol{a}^{(n)} = \mathrm{vec}\left(\boldsymbol{A}^{(n)}\right) \in \mathbb{C}^{I_n R_n \times 1}$, for $n = \{1, \ldots, N\}$. The tensor $\bar{\mathcal{X}}$ is obtained via a similar rearranging than the one illustrated in Fig. 2.9, with the difference that in a N-th factor Kronecker product, we have a long hierarchical block structure. However, this can be easily programmed using permutation and reshaping functions. For example, the Algorithm 4, shows this process using a *MATLAB* syntax.

Algorithm 4 N-th order Kronecker Factorization

1: **Input**: $\boldsymbol{X} \in \mathbb{C}^{I_1 \cdots I_N \times R_1 \cdots R_N}$
2: **Reshaping**: Define $\mathcal{X}' \in \mathbb{C}^{I_1 \times I_2 \times \ldots \times I_N \times R_1 \times R_2 \times \ldots \times R_N}$ as the $2N$-th order tensor by reshaping the elements of $\boldsymbol{X}$, i.e., $\mathcal{X}' = \text{reshape}\left(\boldsymbol{X}, I_1, I_2, \ldots, I_N, R_1, R_2, \ldots, R_N\right)$.
3: **Permuting:** Define $\bar{\mathcal{X}}' \in \mathbb{C}^{I_1 \times R_1 \times I_2 \times R_2 \times \ldots \times I_N \times R_N}$ as the $2N$-th order tensor which is a permutation version of $\mathcal{X}'$, i.e., $\bar{\mathcal{X}}' = \text{permute}\left(\mathcal{X}', [1, N+1, 2, N+2, \ldots, N, 2N]\right)$.
4: **Reshaping**: Define $\bar{\mathcal{X}} \in \mathbb{C}^{I_1 R_1 \times I_2 R_2 \times \ldots \times I_N R_N}$ as the N-th order tensor that is formed by grouping every two dimensions of $\bar{\mathcal{X}}'$, i.e., $\bar{\mathcal{X}} = \text{reshape}\left(\bar{\mathcal{X}}', I_1 \cdot R_1, I_2 \cdot R_2, \ldots, I_N \cdot R_N\right)$.
5: **for** $n = 1 : N$ **do**
6: Compute the SVD of the n-mode unfolding of $\bar{\mathcal{X}}$ as $\left[\bar{\mathcal{X}}\right]_{(n)} = \boldsymbol{U}^{(n)} \Sigma^{(n)} \boldsymbol{V}^{(n)\text{H}}$ and compute an estimation of $\boldsymbol{a}^{(n)}$ as

$$\hat{\boldsymbol{a}}^{(n)} = \boldsymbol{u}_{.1}^{(n)} \left(\sigma_1^{(n)}\right)^{1/N}.$$

7: **end for**
8: **Output**: $\hat{\boldsymbol{a}}^{(N)}, \ldots, \hat{\boldsymbol{a}}^{(1)}$.

The outputs of Algorithm 4, $\hat{\boldsymbol{a}}^{(n)}$, for $n = \{1, \ldots, N\}$, are unique under a scaling ambiguity, i.e., they are related to the true factor as $\boldsymbol{a}^{(n)} = \alpha^{(n)} \hat{\boldsymbol{a}}^{(n)}$, with $\prod_{n=1}^{N} \alpha^{(n)} = 1$. In other words, to remove this scaling effect, we need to know the first element of $N-1$ factors. Supposing that the first element of $\boldsymbol{a}^{(n)}$, we have that $\alpha_n = \boldsymbol{a}_1^{(n)} / \hat{\boldsymbol{a}}_1^{(n)}$, for $n = \{1, \ldots, N-1\}$. Then $\hat{\boldsymbol{a}}^{(N)} = \frac{1}{\alpha_1 \alpha_2 \cdots \alpha_{N-1}} \boldsymbol{a}^{(N)}$.

2.5 Khatri-Rao Product Factorization

The Khatri-Rao approximation problem [40, 48] has a similar proceeding to the Kronecker approximation problem. The main difference is that the rearranging of elements is performed per column. Let us consider $\boldsymbol{Y} = \boldsymbol{B}^{(N)} \diamond \ldots \diamond \boldsymbol{B}^{(1)} + \boldsymbol{N} \in \mathbb{C}^{I_1 \cdots I_N \times R}$, where $\boldsymbol{B}^{(n)} \in \mathbb{C}^{I_n \times R}$ is the n-th factor matrix, for $n = \{1, \ldots, N\}$. The problem is formulated as

$$\min_{\boldsymbol{B}^{(N)}, \ldots, \boldsymbol{B}^{(1)}} \left\| \boldsymbol{Y} - \boldsymbol{B}^{(N)} \diamond \ldots \diamond \boldsymbol{B}^{(1)} \right\|_{\text{F}}^2. \tag{2.91}$$

From the fact that the Khatri-Rao product is defined as the column-wise Kronecker product, the r-th column of $\boldsymbol{Y}$ is given by

$$\boldsymbol{y}_{.r} = \boldsymbol{b}_r^{(N)} \otimes \ldots \otimes \boldsymbol{b}_r^{(1)} \in \mathbb{C}^{I_1 \cdots I_N \times 1}. \tag{2.92}$$

From the property (2.14), the elements of $\boldsymbol{y}_r$ are rearranged into the N-th order rank one tensor $\mathcal{Y}^{(r)}$ which is defined

$$\mathcal{Y}^{(r)} = \text{unvec}_{I_1 \times \ldots \times I_N}\left(\boldsymbol{y}_r\right) = \boldsymbol{b}_r^{(1)} \circ \ldots \circ \boldsymbol{b}_r^{(N)}. \tag{2.93}$$

The factors $\boldsymbol{b}_r^{(n)} \in \mathbb{C}^{I_n \times 1}$ can be estimated using the steps 5-7 of Algorithm 4. This process is repeated for every column of $\boldsymbol{Y}$ and its summarized in Algorithm 5.

Algorithm 5 N-th order Khatri-Rao Factorization

1: **Input**: $\boldsymbol{Y} \in \mathbb{C}^{I_1 \cdots I_N \times R}$
2: **for** $r = 1 : R$ **do**
3: Define $\boldsymbol{\mathcal{Y}}^{(r)} = \text{unvec}_{I_1 \times \ldots \times I_N}(\boldsymbol{y}_r)$
4: **for** $n = 1 : N$ **do**
5: Compute the SVD of the n-mode unfolding of $\boldsymbol{\mathcal{Y}}^{(r)}$ as $\left[\boldsymbol{\mathcal{Y}}^{(r)}\right]_{(n)} = \boldsymbol{U}^{(r,n)} \Sigma^{(r,n)} \boldsymbol{V}^{(r,n)\text{H}}$ and compute an estimation of $\boldsymbol{b}_r^{(n)}$ as

$$\hat{\boldsymbol{b}}_r^{(n)} = \boldsymbol{u}_{\cdot 1}^{(r,n)} \left(\sigma_1^{(r,n)}\right)^{1/n}.$$

6: **end for**
7: **end for**
8: **Output**: $\hat{\boldsymbol{B}}^{(N)} = [\hat{\boldsymbol{b}}_1^{(N)}, \ldots, \hat{\boldsymbol{b}}_R^{(N)}], \ldots, \hat{\boldsymbol{B}}^{(1)} = [\hat{\boldsymbol{b}}_1^{(1)}, \ldots, \hat{\boldsymbol{b}}_R^{(1)}]$.

The outputs of Algorithm 5, $\hat{\boldsymbol{b}}_r^{(n)} \in \mathbb{C}^{I_n \times 1}$ for $n = \{1, \ldots, N\}$, are related to the true factors as $\boldsymbol{b}_r^{(n)} = \beta_r^{(n)} \hat{\boldsymbol{b}}_r^{(n)}$, with $\prod \beta^{(n)} = 1$. However, in the Khatri-Rao Factorization, we perform the rank-one approximation R times, i.e., one per number of columns of the observation matrix $\boldsymbol{Y}$. Thus, the factor matrices are related to the true ones as, $\boldsymbol{B}^{(n)} = \hat{\boldsymbol{B}}^{(n)} \text{diag}\left(\boldsymbol{\beta}^{(n)}\right)$, where $\boldsymbol{\beta}^{(n)} = [\beta_1^{(n)}, \ldots, \beta_R^{(n)}] \in \mathbb{C}^{R \times 1}$ is the scaling vector that collects the scaling factors of the n-th factor, for all rank-one approximation, with $\prod_{n=1}^{N} \text{diag}\left(\boldsymbol{\beta}^{(n)}\right) = \boldsymbol{I}_R$. This means that, the knowledge of the first row of $N-1$ factor matrices is required to remove the scaling ambiguity. Supposing that we know *a priori* the first row of the factors $\boldsymbol{B}^{(n)}$ for $n = \{1, \ldots, N-1\}$, we can estimate this ambiguity as: $\boldsymbol{\beta}^{(n)} = \boldsymbol{B}_{1,\cdot}^{(n)} \oslash \hat{\boldsymbol{B}}_{1,\cdot}^{(n)}$. Then $\boldsymbol{B}^{(N)} = \hat{\boldsymbol{B}}^{(N)} \text{diag}\left(\boldsymbol{1}_R \oslash \left(\boldsymbol{\beta}^{(N-1)} \odot \ldots \odot \boldsymbol{\beta}^{(1)}\right)\right)$.

3 OVERVIEW OF INTELLIGENT RECONFIGURABLE SURFACES

In this chapter, a brief overview of the role of the IRS technology in future 5G and 6G networks is presented. More specifically, a general state-of-the-art view on its hardware implementation, its different operation modes, uses cases in single-cell and multi-cell, channel estimation methods, phase-shift design, and control feedback overhead is discussed.

3.1 What is an IRS?

The IRS, also known as reconfigurable intelligent surface (RIS), is a new technology to be introduced in wireless communication networks that has the capability to re-direct the impinging electromagnetic wave into a specific direction, i.e., it controls the propagation directions [49, 50, 51]. An IRS is a 2-D surface or metasurface [49, 50, 51] that contains several reconfigurable reflective elements and a smart controller who is responsible to reconfigure the phase-shift, amplitude coefficient of each IRS element. An example of IRS is illustrated in Fig. 3.1, where a smart controller is connected to the surface reconfigure the elements. In the literature, there are several different fabrication types of IRS. From electronic components devices such as positive-intrinsic-negative (PIN) diodes, field-effect transistors (FETs), varactors, [49] to metamaterials like graphene and liquid crystals [50, 52].

Figure 3.1 – Illustration of an IRS.

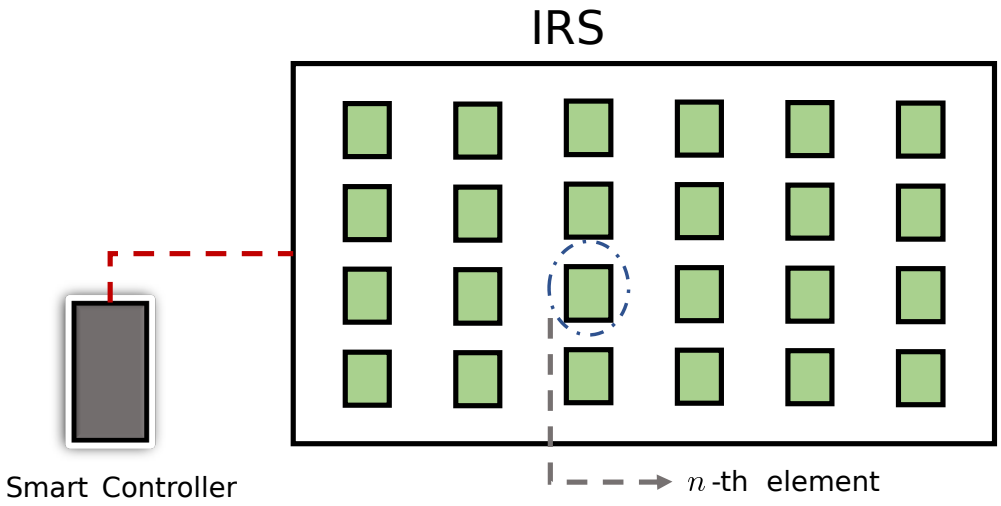

Source: Created by the author.

Assuming the illustrated IRS has N reconfigurable elements, we can define the vector that collects it as

$$\boldsymbol{s} = \left[\beta_1 e^{j\theta_1}, \beta_2 e^{j\theta_2}, \ldots, \beta_N e^{j\theta_N}\right]^{\mathrm{T}} \in \mathbb{C}^{N\times 1}, \tag{3.1}$$

where β_n is the coefficient amplitude of the n-th IRS element, and θ_n is the phase-shift applied to the n-th IRS element. Typically, the coefficient amplitude defines the amount of energy of the

impinging signal that is reflected, varying between zero and one, i.e., $\beta_n = [0, 1]$.

Nowadays, IRS technology is not restricted to only performing a reflection of the signal. In fact, its reflection property is one of its operational modes. We can separate IRS hardware model implementation into two major groups, passive IRSs, and active IRSs, while in terms of operation modes, we have reflection, transmission, sensing, absorption, and simultaneously transmission and reflection [52].

Summarizing, the IRS is a paradigm changing in wireless communications since usually the propagation medium is considered to be uncontrollable due to the several scatters present between the transmitter and receiver. In Fig. 3.2 we illustrate a comparison between massive MIMO and MIMO IRS-assisted networks. In Fig. 3.2 (a) the base station (BS) is equipped with tens or hundreds of antenna elements to generate sharp beams and serve the users at a high rate and reliability. However, from the fact that IRS is a large panel with several reconfigurable elements of a low-cost implementation device, one can exploit these advantages to extensively deploy IRSs in the network to create sharp beams to serve multiple users without the need to equip the BS with a massive number of antennas [50], as illustrated in In Fig. 3.2 (b). But this does not mean that MIMO IRS-assisted systems should replace massive MIMO

Figure 3.2 – Paradigm shift in wireless networks.
(a) Massive MIMO system.

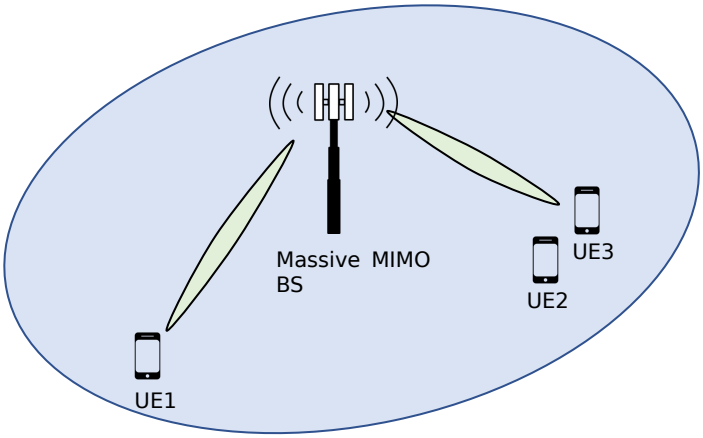

(b) MIMO IRS-assisted system.

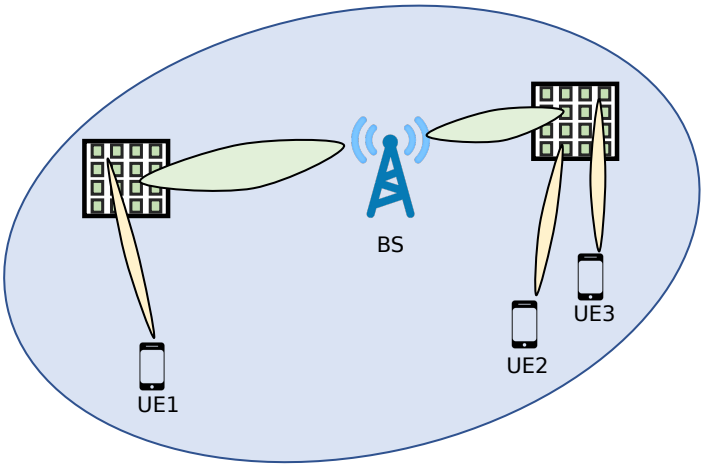

Source: Created by the author.

Figure 3.3 – Illustration of different applications of IRS in wireless communication network.

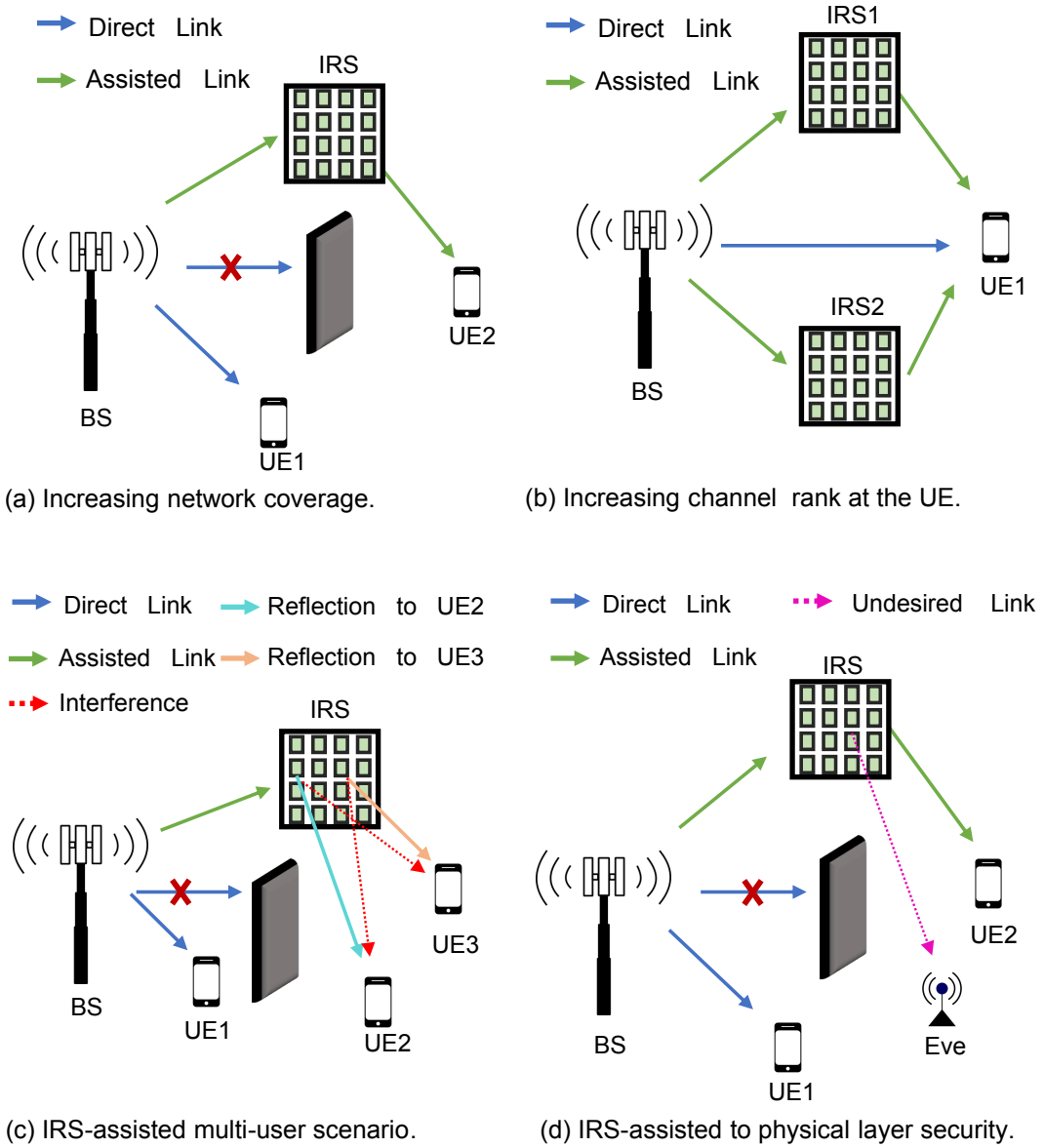

Source: Created by the author.

systems. These two technologies can be combined to improve even more system reliability, rate, and user quality of service. In [53], the authors discuss the benefits and trade-offs between spatial multiplexing and path loss decrease, when combining IRS with massive MIMO systems.

3.1.1 Advantages of IRS

In Figure 3.3, some of the advantages of implementing the IRS in wireless communication networks are illustrated. Similar to relays stations, the IRS can increase the network coverage by overcoming obstacles, making it possible for the BS to serve more users, and enhance the system capacity [54]. In Fig. 3.3 (a) the BS is only able to connect with UE2 through an IRS-assisted link, where it can be viewed as a virtual line-of-sight (LOS) link. Compared to the relay station case, the deployment of IRSs in the network is far easier since IRSs are made of

low-cost implementation components with a lower power consumption [50, 54].

Fig. 3.3 (b) shows the use of the IRS to increase the rank of the channel in BS-user equipment (UE) communication [50]. In this case, IRS1 and IRS2 act like an artificial scatter configured to improve the channel conditions at the receiver [50]. The multi-user scenario is also envisioned with the aid of the IRS, as illustrated in Fig. 3.3 (c). In this case, the IRS can be partitioned into regions to serve different users, wherein each region the phase-shifts are properly designed for the users. The main problem is how to handle the interference among the users of different regions. In [55], the authors proposed a solution based on non-orthogonal multiple access (NOMA) to overcome this issue, while in [56], the authors solve this problem using a machine learning based algorithm.

Another application of IRS in wireless communication networks is its use to improve physical layer security, as illustrated in 3.3 (d). To improve the communication secrecy, the IRS is configured to enhance the received signal-to-noise ratio (SNR) such that the BS can transmit to UE2 using minimal power for information, while the rest of the power is used to generate artificial noise [57]. The works of [58] and [59] show the use of IRS in NOMA networks, while in [58], the authors proposed a design of the IRS phase-shift to eliminate the received signal at the Eve. In [59], the authors show that the secrecy diversity order depends on the number of IRS elements and the fading parameter of the Nakagami-*m* model.

3.2 IRS Characteristics

In this section, we discuss some of the hardware designs for implementing an IRS. We focus on the discussion of passive *v.s.* active IRS. Also, we overview some of its operation modes, e.g., reflection, transmission, and simultaneous transmission and reflection, and its usual fabrication technology, PIN diodes, varactors, and metamaterial such as graphene.

3.2.1 Hardware Design

Although the IRS hardware design has a lot of distinguishing functionalities, it is mainly divided into two categories, passive and active IRS.

3.2.1.1 Passive IRS:

As it was briefly introduced, passive IRSs contain several reconfigurable passive elements that are capable to manipulate the incoming electromagnet waves and re-direct to a pre-determined direction, and are made of low-cost and low-power hungry components [49, 50, 52]. Its structure is based on metal layers printed on dielectric substrates to control the incident electromagnet waves. In particular, the reflective elements are implemented using technologies such as, for example, PIN diodes, and varactor circuits [51], where the phase-shift adjustment is done by the IRS controller which practically is the only active component (usually made of a field-programmable gate array (FPGA) [50]). By applying a bias voltage on the tunable

elements, the IRS controller changes the circuit impedance and consequentially the phase-shift of an element or group of elements.

The main advantage of passive IRS is its low-cost implementation and low-power consumption allowing it to be deployed in e.g., building facades, indoor environments, malls, etc. [49, 50, 52]. Also, passive IRSs are full-duplex devices having no noise amplification achieving a close to higher EE and SE compared to other technologies such as amplify-and-forward (AF) and decode-and-forward (DF) relays [54, 60, 61], depending on the number of elements. On the other hand, passive IRS does not possess any radio frequency (RF) chain, and consequentially no signal processing is possible. This turns the channel information acquisition problem harder since only the cascaded channel, i.e., the TX-IRS-RX equivalent channel, is available at the receiver side. However, the optimum phase-shift configuration for the IRS elements depends on the angles of the cascade channel, not being necessary to separate them [50, 62, 63].

Figure 3.4 – Illustration of a IRS with few active elements .

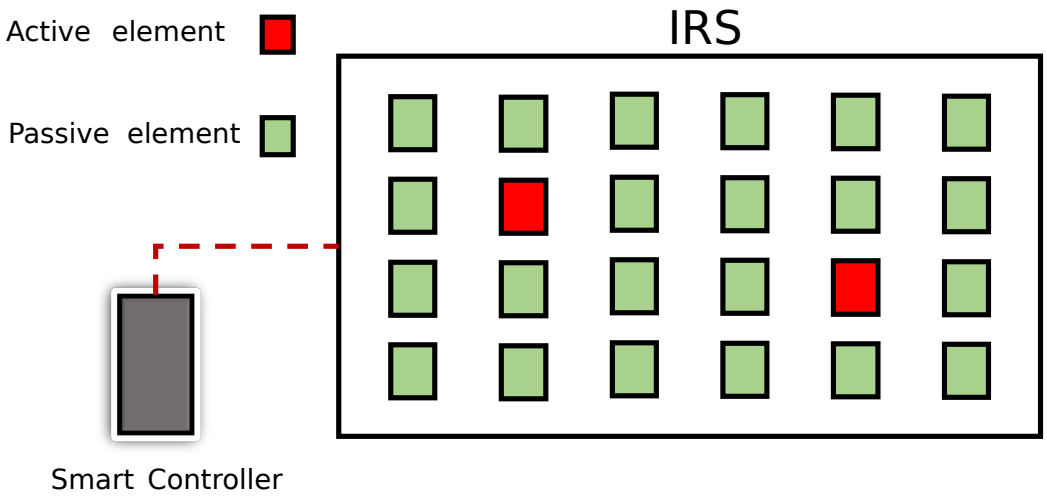

Source: Created by the author.

3.2.1.2 Active IRS:

In the active design, the IRS contains several or few a elements with dedicated RF chains. In the case of a few active elements, they are often used for sensing (sending pilots) and processing signals [64, 65, 66], while the rest of the elements has a passive design. This IRS is illustrated in Fig. 3.4, and comparing it with the passive IRS case, the active elements introduce an additional power-consumption to the system, but, as a benefit, it can process pilots to assist in the channel estimation problem. In this case, the channel response of the passive elements can be obtained, for example, using CS techniques [64], or matrix completion techniques [67].

The case of a surface where the element size is much larger than the operational wavelength is known as large intelligent surfaces (LIS) [52, 68, 69]. In the LIS implementation, the far-field plane wave assumption does not hold and new techniques based on the near-field

spherical waves are adopted [69], e.g., Holographic MIMO [70, 71, 72], which consists of adopting a very large number $N \rightarrow \infty$ of elements on a surface.

Figure 3.5 – Illustration of a LIS with different element spacing.

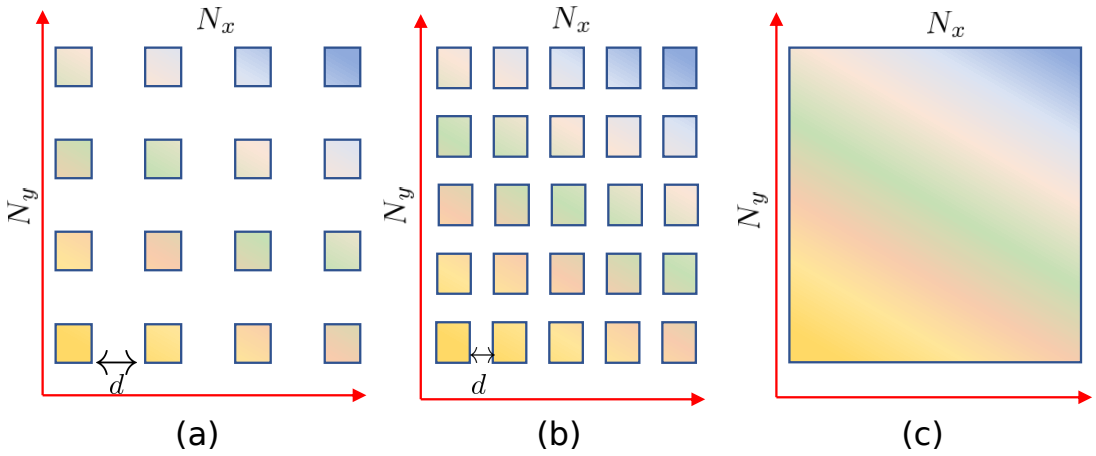

Source: Created by the author.

In Fig. 3.5, an IRS with $N = N_x N_Y$ elements is illustrated. Assuming λ as the operation wavelength, in Figure 3.5 (a) we have an IRS with element spacing $d = 0.5\lambda$, while in (b), with a smaller inter-element spacing $d < 0.5\lambda$, a higher number of element are concentrated in the same area, and in (c), with $d \rightarrow 0$, we have a continuous surface. Fig. 3.5 (a) and (b) are also called as discrete IRSs, while (c) is considered a continuous IRS [52]. The reduction of element spacing is possible in higher operational frequencies. For example, in sub-Tera-Hertz (THz) communications, the size of a IRS element from a graphene-based fabrication, is of 200μm $\times$ 190μm at $\lambda \approx 1360\mu$m [72, 73].

3.2.2 Operation Modes

The main operational modes of IRSs are listed as:

3.2.2.1 Reflecting IRSs

This was the original design purpose of passive IRS, i.e., a device capable to be reconfigurable to control the angular propagation of the impinging electromagnet waves [50], [52]. The ability to control the environment comes from low-cost eletronic components such as PIN diodes, varactors circuits [49], where, by applying a bias voltage in the elements, the IRS smart controller changes the circuit impedance, thus controling the angular reflection to the desired direction. However, [49] [50] shows that using these low-cost materials, the angular and the amplitude coefficients of the IRS are not independent.

3.2.2.2 Receiving IRSs

This operation mode is directly correlated with the active IRS with few active elements. The idea is to have a few elements with dedicated RF chains to perform channel estimation, pilot sequence processing, etc. The channel on the passive elements can be estimated using, for example, CS methods [64], or matrix completion based techniques [67].

3.2.2.3 Simultaneous Reflecting and Sensing IRSs

In this case, an element of the IRS is composed of two parts, one for reflecting and the other for sensing. These parts are connected via a wave-guide which can be connected to an RF chain. Consequentially, a portion of the received signal can be digitally processed [52, 74]. This hybrid IRS is also implemented using low-cost eletronic components, such as the ones previously mentioned, PIN and varactor diodes.

3.2.2.4 Simultaneous Transmitting and Reflecting IRSs

This implementation called simultaneous transmitting and reflecting (STAR)-IRS, is a recent type of IRS proposed by [75, 76, 77]. It is a 2-D surface where the element can reflect a portion of the received signal to a specific direction while transmitting a portion of the received signal to a different direction. The transmission capability act like the refraction phenomena. The STAR-IRS elements can operate in three different ways, 1) to perform transmission and reflection with an energy splitting protocol, 2) to perform only reflection, or 3) only transmission. The STAR-IRS controller can switch the operation of the elements based on system demand. Different from traditional IRSs, the STAR-IRS has 360° coverage, being suitable in scenarios, for example, I2O and O2I. A similar implementation to the STAR-IRS is called intelligent omni-surface (IOS), which also has a 360° coverage capability, it was proposed in [78, 79]. Both STAR-IRS and IOS are made of low-cost eletronic components.

3.3 IRS Use Cases

In Section 3.1.1, the advantages of deploying the IRS in wireless communication from a single-cell point of view were discussed. In this section, we extend to the possible IRS use cases in macro scenarios, such as I2O and O2I, multi-cell, and cell-free scenarios.

In Fig. 3.6 we show a macro scenario of an I2O and O2I. In the first moment, the IRS can be deployed in, e.g., buildings facades, to assist I2O and O2I communication. This can be accomplished using, for example, STAR-IRSs, where one can transmit and reflect in 360° degrees of coverage [75, 77]. Also, as mentioned, STAR-IRS can act in three principles, energy splitting for reflection and transmission, only reflection, or only transmission. Thus, depending on the network, the STAR-IRS can switch to outdoor-to-outdoor (O2O), or indoor-to-indoor (I2I). Recently, unmanned aerial vehicle (UAV) IRS-assisted networks were proposed in [80,

Figure 3.6 – General application of IRS in I2O and O2I scenarios.

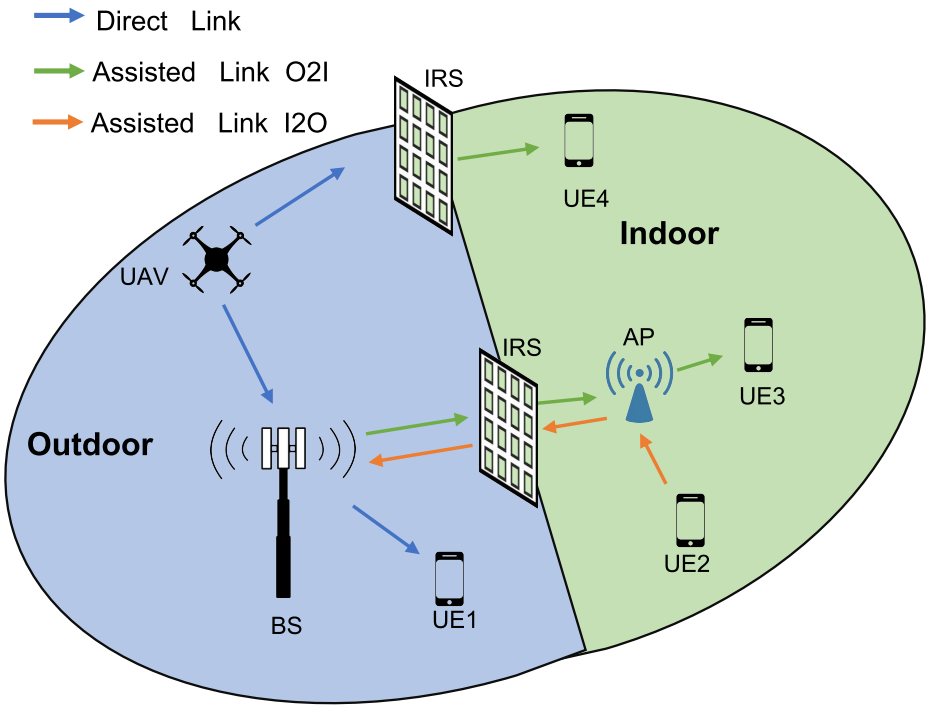

Source: Created by the author.

81, 82, 83, 84, 85]. In [80], the authors collect several applications and scenarios for UAV in IRS-assisted networks, such as Internet of Things (IoT) [83], capacity enhancement [85], physical layer security, parameter optimization [82, 84], relaying [84, 85], and energy saving in wireless power transfer systems [81], etc.

The deployment of IRSs in the multi-cell system has caught the attention of researchers in recent years [86, 87, 88, 89]. The main advantages of IRS in multi-cell systems are that they are the low-cost implementation which makes there easy to deploy at, e.g., the cell-edges to assist the high attenuated users. Also, the IRS can be configured to suppress the inter-cell interference, by properly adjusting its phase-shifts [87]. The work of [86] considers a multi-cell multi-band scenario and investigates the sum-rate maximization by minimizing the transmitted power. They also provide a frequency-depending design for the IRS phase-shifts. In [87], the authors consider a multi-cell NOMA network with a single IRS, where they propose a resource allocation framework to enhance the SE. The works of [89] and [88] propose a sum rate problem to joint design the transmit beamforming and the IRS phase-shift in multi-cell multiple-input single-output (MISO) systems.

With the advances of 5G networks, where mmWave frequencies will be employed to deliver higher rates, the radius of the communication cells is smaller, especially in the 5G frequency range (FR)2, where the frequency range is 24.250 up to 52.600 Giga-Hertz (GHz), much higher than FR1 where the frequencies are from 410 Mega-Hertz (MHz) to 7.125 GHz [90]. Consequentially, a massive BS deployment is expected, implying a high infrastructure cost, such as the backhauling fiber connection. To overcome this issue, in 5G networks there is the concept of integrated access and backhaul (IAB) nodes [91, 92], where the backhaul link connection is

Figure 3.7 – General application of IRS in multi-cell system with multiple users and multiple IRSs.

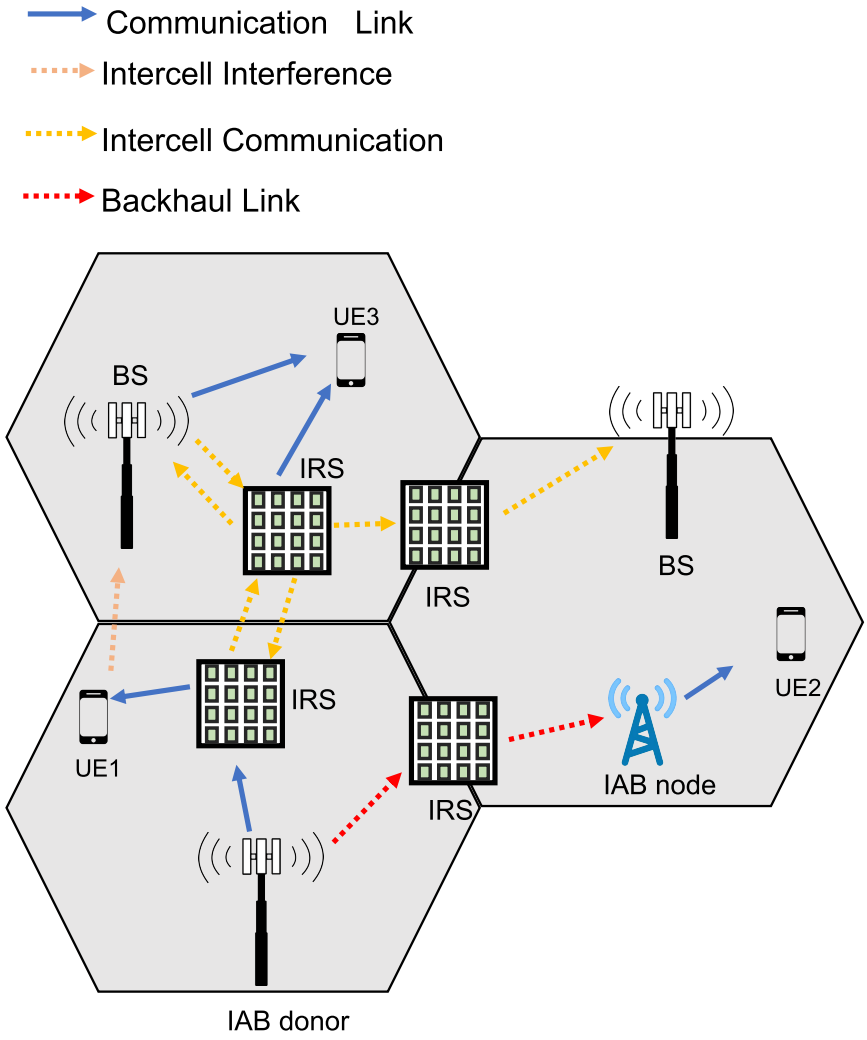

Source: Created by the author.

through a wireless channel. Nowadays, the use of IRS to aid in IAB communications is under investigation [93, 94, 95]. In [93], the authors propose a network plan integrating IAB nodes and IRS to overcome blockages in 5G mmWave networks. The authors of [94] show the benefits of IRS in UAV-IAB networks in terms of energy efficiency. In [95], a performance analysis over IRS-assisted IAB networks is provided, considering single and multi-hop backhauling in a mesh topology.

Following the context of 5G mmWave and future 6G networks, there is the concept of cell-free MIMO, where the communication cell has no more boundaries, and there are many access points (APs), each serving a small number of users, distributed over the cell and connected to a central unit process [96, 97]. Following this idea, the works [98, 99, 100] are related to IRS-assisted cell-free MIMO networks. The work [98] proposes the use of IRS attached in UAVs to assist the communication between the AP and the user. In [99], a decentralized framework is proposed, where the transmitted beamforming and the IRS phase-shifts are jointly optmized for cell-free MIMO systems. The authors of [100] tackles the ernegy cost problem of large BS

deploy with multiple IRS. Their scheme consist of a hybrid beamforming architeture where the digital BS beamformer and analog IRS beamforme is proposed.

Although the above mentioned scenarios are under discussion, the process of standardization of IRS for future beyond fifth-generation (B5G) networks may take some time. According to [52], in3rd Generation Partnership Project (3GPP), one possibility to start the standardization of IRSs is in Release 19 describing the channel model, use cases, and deployment scenarios, which can be expected in the year 2023.

3.4 Channel Estimation

Several works have addressed the channel state information (CSI) acquisition problem in IRS-assisted networks, e.g., [22, 101, 102, 103, 104, 105, 106, 107]. Usually, the channel estimation phase, the IRS phase-shift is pre-designed as discrete Fourier transform (DFT)-based or Hadamard structure, due to its Hermitian properties.

The work of [102] proposes a compressed sensing approach in a multi-user uplink MIMO scenario. In [103], a two time-scale channel estimation framework is proposed to overcome the pilot overhead in a multi-user IRS-aided system. Also, [104] addresses the channel estimation problem in millimiter-wave MIMO systems, where random blockages that can be caused by rough weather conditions were taken into consideration. The authors of [105] propose a low-complexity framework for channel estimation and passive beamforming in MIMO IRS-assisted systems. In [101], a semi-blind receiver is proposed for joint channel and symbol estimation in multi-user IRS-assisted MIMO systems. In [107] the authors propose a channel estimation and joint passive and active beamforming design in MIMO multi-IRS-assisted system. In this scenario, each IRS is aligned to a different channel path to enhance the achievable data rate.

The works of [108, 109, 110, 111] focus on the channel estimation problem in mmWave and/or massive MIMO by exploiting the sparsity of the channels and solving the parameters recovery problem using CS tools. More specifically, the authors of [108] propose a channel estimation framework, namely TRICE (Two-Stage RIS-aided Channel Estimation) for mmWave IRS-assisted single-user MIMO systems exploiting the sparsity at both BS and UE side, while on the other hand, the authors of [109] proposed a recovery problem exploiting the sparsity only at the side of the BS. Different from these works, [110] considers the broadband channel estimation problem by combining massive MIMO and IRS with OFDM to overcome the frequency selectivity of the sparse channels. The authors of [111] consider the channel estimation problem using holographic IRS in THz frequencies by taking into account the sparsity of the THz channels in the angular and time (delay) domain.

In [22] a tensor-based method for channel estimation in MIMO IRS-assisted systems is proposed. They show the benefits of exploiting the multidimensional structure of the received signal, where thanks to the tensor-based signal processing, allows separating the involved channels from the cascade channel to refine its estimation. Basically, they consider a frame

structure with two time dimensions. More specifically, they consider a frame structure of K blocks, each of T time-slots. Assuming that $\boldsymbol{G} \in \mathbb{C}^{M_R \times N}$ and $\boldsymbol{H} \in \mathbb{C}^{N \times M_T}$ are the IRS-RX and TX-IRS channels, the received signal at the k-th block frame is

$$\boldsymbol{Y}_k = \boldsymbol{G}\text{diag}_k\left(\boldsymbol{S}\right)\boldsymbol{H}\boldsymbol{X}^{\mathrm{T}} + \boldsymbol{V}_k \in \mathbb{C}^{M_R \times T}, \tag{3.2}$$

where $\boldsymbol{V}_k$ is the additive noise matrix on the k-th block, $\boldsymbol{X} \in \mathbb{C}^{T \times M_T}$ is the pilot matrix with T being the length of the pilot sequence, and $\boldsymbol{S} \in \mathbb{C}^{K \times N}$ is the IRS phase-shift matrix with a DFT design. Noting that (3.2) represents the k-th frontal slice of a PARAFAC tensor, the received PARAFAC tensor signal is given by

$$\mathcal{Y} = \mathcal{I}_{3,N} \times_1 \boldsymbol{G} \times_2 \boldsymbol{X}\boldsymbol{H}^{\mathrm{T}} \times_3 \boldsymbol{S} \in \mathbb{C}^{M_R \times T \times K} + \mathcal{V}. \tag{3.3}$$

From the fact that the matrices $\boldsymbol{X}$ (pilots) and $\boldsymbol{S}$ (DFT-based) are known at the receiver, the work of [22] proposes two algorithms to estimate the channels $\boldsymbol{G}$ and $\boldsymbol{H}$, one is based on closed-form solution Khatri-Rao factorization (KRF), while the second algorithm is iterative, based on the bilinear alternating least squares (BALS) solution. The authors have shown that separating the cascade channel using the tensor-based approach to refine the individual channels has a better performance than classical LS solutions. However, the main drawback of their solution is the long pilot sequence, since, to fulfill the identifiability conditions of the KRF and BALS algorithms, it is required that the number of blocks, times the minimum number between the receiving antennas and the length of the pilot sequence, must be greater or equal to the number of IRS elements, i.e., $K\min(T, M_R) \geq N$, with $T \geq M_T$.

3.5 IRS Phase-shift Optimization

In this section, we briefly discuss the IRS phase-shift optimization for IRS-assisted single-input single-output (SISO) and MIMO.

3.5.1 SISO Case

Ideally, the IRS contains N independent phase-shifts, which can provide an SNR gain in order of $O\left(N^2\right)$ [51, 112]. This comes from the fact the IRS with passive elements is full-duplex by nature, i.e., the incoming signal is instantaneously reflected into a specific direction, with no noise amplification, while the received power is proportional to N. To achieve this SNR gain, the IRS phase-shifts must be optimized to promote a coherent and constructive superposition of the reflected signal copies at the receiver. Let us assume a SISO case where the TX-IRS and IRS-RX involved channels are denoted by $\boldsymbol{h} \in \mathbb{C}^{1 \times N}$, and $\boldsymbol{g} \in \mathbb{C}^{N \times 1}$, respectively, and the IRS vector that contains the phase-shifts is given by $\boldsymbol{s} = \left[\beta_1 e^{j\theta_1}, \beta_2 e^{j\theta_2}, \ldots, \beta_N e^{j\theta_N}\right]^{\mathrm{T}} \in \mathbb{C}^{N \times 1}$.

In this case, the SNR is given by

$$\gamma = \frac{\left|\boldsymbol{g}^{\mathrm{H}}\mathrm{diag}\left(\boldsymbol{s}\right)\boldsymbol{h}x\right|^2}{\sigma_v^2}, \tag{3.4}$$

$$= \frac{\left|\sum\limits_{n=1}^{N} g_n^* \beta_n e^{j\phi_n} h_n x\right|^2}{\sigma_v^2}, \tag{3.5}$$

where x is the transmitted symbol with $\mathbb{E}\left[xx^*\right] = 1$, σ_v^2 is the variance of the received additive noise. Noting that the channels entries are complex-valued, the n-th element of the channels $\boldsymbol{h}$ and $\boldsymbol{g}$ are denoted as $h_n = |h_n|e^{j\varphi_n^{(h)}}$, and $g_n = |g_n|e^{j\varphi_n^{(g)}}$. It is clear that, in order to maximize the SNR in (3.5) the amplitude coefficient $\beta_n = 1 \forall n \in N$, while the IRS phase-shift should be aligned with the channels angles, i.e.,

$$\phi_n^{(\mathrm{opt})} = -(\varphi_n^{(g)*} + \varphi_n^{(h)}), \forall n \in N. \tag{3.6}$$

Substituting (3.6) into (3.5), we have

$$\gamma = \frac{\left|\sum\limits_{n=1}^{N} |g_n| e^{j\varphi_n^{(g)*}} e^{j\phi_n^{\mathrm{opt}}} |h_n| e^{j\varphi_n^{(h)}} x\right|^2}{\sigma_v^2}, \tag{3.7}$$

$$= \frac{\left|\sum\limits_{n=1}^{N} |g_n| e^{j\left(\varphi_n^{(g)*} + \varphi_n^{(h)} - (\varphi_n^{(g)*} + \varphi_n^{(h)})\right)} |h_n| x\right|^2}{\sigma_v^2}, \tag{3.8}$$

$$= \frac{\left|\sum\limits_{n=1}^{N} |g_n||h_n| x\right|^2}{\sigma_v^2} \tag{3.9}$$

$$= N^2 \frac{|\boldsymbol{g}^{\mathrm{H}}|^2 |\boldsymbol{h}|^2}{\sigma_v^2}. \tag{3.10}$$

3.5.2 MIMO Case

In the MIMO case, the optimization of the IRS phase-shift becomes more challenging. In this case, the problem becomes

$$\max_{\boldsymbol{s}=[e^{j\theta_1},\ldots,e^{j\theta_N}]} \log_2\left(\boldsymbol{I}_{M_r} + \frac{\boldsymbol{G}^{\mathrm{H}}\mathrm{diag}\left(\boldsymbol{s}\right)\boldsymbol{H}\boldsymbol{R}_{xx}\boldsymbol{H}^{\mathrm{H}}\mathrm{diag}\left(\boldsymbol{s}^*\right)\boldsymbol{G}}{\sigma_v^2}\right), \tag{3.11}$$

where $\boldsymbol{R}_{xx} = \mathbb{E}\left[\boldsymbol{x}\boldsymbol{x}^{\mathrm{H}}\right] \in \mathbb{C}^{M_T \times M_T}$. The authors of [113] proposed an alternating optimization procedure to solve the problem in (3.11). The main idea is to split (3.11) in N sub-problems.

In the literature, several other works proposed different strategies for phase-shift optimization in IRS-assisted MIMO systems. In the work of [114], a low-complexity framework to optimize the IRS phase-shift based on the maximization of the average received SNR is proposed. In [115], the authors proposed the IRS phase-shift optimization for multi-user MISO systems (virtually MIMO), based on an IRS phase-shift selection algorithm.

3.5.3 MIMO Single Stream Transmission Case

In this thesis, we focus our attention on the MIMO single stream transmission case proposed in [116] since this scenario will be considered in Chapter 5.

Let us consider a single stream transmission, and assume that there is no direct link between the TX and RX, e.g., BS. First, the TX sends a pilot signal to the RX with the aid of the IRS. Since the IRS has no signal processing capabilities, the channel estimation and the IRS phase-shifts optimization are performed at the RX. The received signal after processing the pilots is given by

$$y = \boldsymbol{w}^{\mathrm{H}}\boldsymbol{G}\mathrm{diag}\left(\boldsymbol{s}\right)\boldsymbol{H}\boldsymbol{q} + \boldsymbol{w}^{\mathrm{H}}\boldsymbol{b}, \tag{3.12}$$

where $\boldsymbol{b} \in \mathbb{C}^{M_R \times 1}$ is the additive noise at the receiver with $\mathbb{E}[\boldsymbol{b}\boldsymbol{b}^{\mathrm{H}}] = \sigma_b^2 \boldsymbol{I}_{M_r}$, $\boldsymbol{w} \in \mathbb{C}^{M_R \times 1}$ and $\boldsymbol{q} \in \mathbb{C}^{M_T \times 1}$ are the receiver and transmitter combiner and precoder, respectively. $\boldsymbol{H} \in \mathbb{C}^{N \times M_T}$ and $\boldsymbol{G} \in \mathbb{C}^{M_R \times N}$ are the TX-IRS and IRS-RX involved channels, and $\boldsymbol{s} = [e^{j\theta_1}, \ldots, e^{j\theta_N}] \in \mathbb{C}^{N \times 1}$ being the IRS phase-shift vector, where θ_n is the phase-shift applied to the n-th IRS element. The optimization problem in (3.11) becomes:

$$\max_{\boldsymbol{s},\boldsymbol{q},\boldsymbol{w}} \left| \boldsymbol{w}^{\mathrm{H}}\boldsymbol{G}\mathrm{diag}\left(\boldsymbol{s}\right)\boldsymbol{H}\boldsymbol{q} \right|, \tag{3.13}$$

with $||\boldsymbol{w}|| = 1$, $||\boldsymbol{q}|| = 1$, and $\theta_n \in [-\pi, \pi]$, for $n = \{1, \ldots, N\}$. To solve (3.13), the authors in [116] proposed three different algorithms, an upper-bound, an lower-bound, and an alternating optimization solution. We drive our attention to the upper-bound solution.

Upper-bound solution [116]: Let us assume the SVDs of $\boldsymbol{H} \in \mathbb{C}^{N \times M_T}$ and $\boldsymbol{G} \in \mathbb{C}^{M_R \times N}$, with $\mathrm{rank}(\boldsymbol{H}) = I$, and $\mathrm{rank}(\boldsymbol{G}) = J$, as $\boldsymbol{H} = \sum_{i=1}^{I} \sigma_i^{(h)} \boldsymbol{u}_i^{(h)} \boldsymbol{v}_i^{(h)\mathrm{H}} = \boldsymbol{U}^{(h)} \Sigma^{(h)} \boldsymbol{V}^{(h)\mathrm{H}}$ and $\boldsymbol{G} = \sum_{j=1}^{J} \sigma_i^{(g)} \boldsymbol{u}_j^{(g)} \boldsymbol{v}_j^{(g)\mathrm{H}} = \boldsymbol{U}^{(g)} \Sigma^{(g)} \boldsymbol{V}^{(g)\mathrm{H}}$. From the natural ordering of the SVD, the singular values are distributed as $\sigma_1^{(h)} \geq \sigma_2^{(h)} \geq \ldots \geq \sigma_I^{(h)}$, and $\sigma_1^{(g)} \geq \sigma_2^{(g)} \geq \ldots \geq \sigma_J^{(g)}$, the optimal design for $\boldsymbol{w}$, $\boldsymbol{q}$, and $\boldsymbol{s}$ is given by [116]

$$\boldsymbol{q} = \boldsymbol{v}_1^{(h)} \in \mathbb{C}^{M_T \times 1}, \tag{3.14}$$

$$\boldsymbol{w} = \boldsymbol{u}_1^{(g)} \in \mathbb{C}^{M_R \times 1}, \tag{3.15}$$

$$\theta_n = -\angle \left(v_{n,1}^{(g)*} \cdot u_{1,n}^{(h)} \right), \forall n \in N \tag{3.16}$$

$$\boldsymbol{s} = \left[e^{j\theta_1}, \ldots, e^{j\theta_n}, \ldots, e^{j\theta_N} \right] \in \mathbb{C}^{N \times 1}, \tag{3.17}$$

i.e., the strongest TX-IRS and IRS-RX links are selected to design the precoder, combiner, and phase-shifts of the IRS.

3.6 IRS Phase-shift Feedback Overhead

Although the IRS technology brings all the discussed advantages and scenarios in 5G and future 6G wireless communications, there is the issue of control signaling overhead. For

example, let us consider the MIMO single stream example. After the channel estimation step, the precoder and the combiner (active beamformers) vectors $\boldsymbol{w}$ and $\boldsymbol{q}$, and the IRS phase-shift vector $\boldsymbol{s}$ (passive beamformer) are optimized. Later, the RX needs to feedback to the IRS controller the designed phase-shifts so that the IRS controller tunes the phase-shift for each IRS element. Because this feedback occurs in a limited capacity control channel and the IRS may contain several hundred to thousands of reflecting elements, the feedback of each phase-shift with a certain resolution imposes a signaling overhead.

In this regard, the works of [116, 117] propose two different approaches to overcome the feedback issue in MIMO IRS-assisted networks. The work of [117] considers a MIMO-OFDM IRS-assisted system, focusing on the channel state information (CSI) feedback. The authors consider that the channel response in a region of the IRS is approximately the same due to the spatial correlation among the close elements. In other words, the authors propose to split the IRS into K regions, each having B elements. In this case, the IRS phase-shift vector is reformulated as

$$\boldsymbol{s} = \mathbf{1}_B \otimes \bar{\boldsymbol{s}} \in \mathbb{C}^{KB\times 1}, \tag{3.18}$$

where $\bar{\boldsymbol{s}} \in \mathbb{C}^{K\times 1}$ is the total number of independent phase-shifts per region, with the total number of IRS elements being $N = KB$. Thus, only K entries of the channels are fed back to the TX to design the precoder beamformer. The authors in [117] analyse the trade-off when K and B, where, for example, when the number of elements inside a group B increases, the total number of groups K decreases since $N = BK$, thus the spectral efficiency and the feedback overhead decreases. On the other hand, reducing B results in increasing K which means a higher spectral efficiency and feedback overhead since more channel elements are fed back.

The work [116] focus on the IRS phase-shift feedback overhead to the IRS controller. They model the feedback duration as

$$T_{\mathrm{F}} = \frac{N b_{\mathrm{F}}}{B_{\mathrm{F}} \log\left(1 + \frac{p_{\mathrm{F}}|g_{\mathrm{F}}|^2}{B_{\mathrm{F}} N_0}\right)}, \tag{3.19}$$

where N is the total number of IRS phase-shifts to be fed back, B_{F}, p_{F} are the feedback bandwidth and power, respectively, g_{F} is the scalar control channel used, b_{F} is the resolution of each phase-shift, and N_0 is the noise power density.

In Fig. 3.8, we illustrate the total number of bits to be feedback as we increase the number of IRS elements and its their resolution, i.e., the numerator of (3.19). It becomes clear that, for a large N with a high resolution b_{F}, the feedback duration of the IRS phase-shifts causes a control signaling overhead that degradates the system SE, given in (3.20). To overcome this issue, the authors of [116] focus on the problem of SE and EE maximization by optimizing the resource allocation, where the SE is given by

$$\mathrm{SE} = \left(1 - \frac{T_E + T_F}{T}\right) B \log_2\left(1 + \frac{p_{\mathrm{TX}}|\boldsymbol{w}^{\mathrm{H}}\boldsymbol{G}\mathrm{diag}\,(\boldsymbol{s})\,\boldsymbol{H}\boldsymbol{q}|^2}{BN_0}\right), \text{in bps}, \tag{3.20}$$

Figure 3.8 – Feedback payload, in bits, as function of the number of IRS elements N and the feedback quantization bits b_{F}.

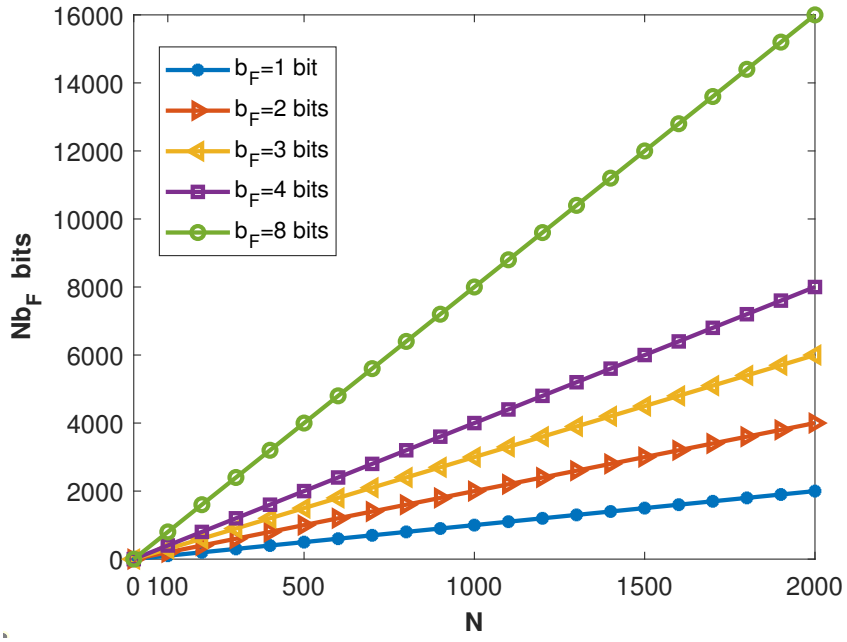

Source: Created by the author.

with T_E and T being the duration of the channel estimation phase and the total time interval, and B the transmission bandwidth. The EE is given by $\mathrm{EE} = \mathrm{Rate}/P_{\mathrm{tot}}$, and the total power consumption P_{tot} can be expressed as

$$\mathrm{P}_{\mathrm{tot}} = P_{\mathrm{E}} + \frac{T - T_{\mathrm{E}} - T_{\mathrm{F}}}{T}\mu p + \frac{\mu_{\mathrm{F}} p_{\mathrm{F}} T_{\mathrm{F}}}{T} + P_{\mathrm{c}}, \tag{3.21}$$

where P_{E} is the power used for the channel estimation phase, $1/\mu$ is the efficiency of the transmitter power amplifier, p_{F} is the power used during T_{F} seconds, and μ_{F} is the efficiency of the transmit amplifier used for feedback. The work [116] maximizes (3.20) and (3.21) by optimizing the resources p_{TX}, p_{F}, B, B_{F}.

In Chapter 5, we propose a new feedback overhead method by focusing on the numerator of (3.19), where we reduce the number of the IRS phase-shifts to be conveyed to the IRS controller thanks to the proposed tensor-based factorization.

4 TENSOR-BASED RECEIVER FOR PARAMETER ESTIMATION IN MIMO-OFDM SYSTEMS

OFDM has been adopted in third-generation (3G)/fourth-generation (4G) Long Term Evolution (LTE) services due to its well known robustness to multi-path propagation, frequency-selective fading, as well as low complexity implementation and equalization [118, 119]. However, these advantages rely on a perfect system synchronization to keep intact the orthogonality among the subcarriers. In practical scenarios, synchronization impairments lead to ICI that degrades the ultimate system performance. The two most common impairments that destroy subcarrier orthogonality is the carrier frequency offset (CFO), which is caused by the Doppler frequency shift effect induced by the mobility of the user, as well as the PN originated by hardware imperfections at the transmitter and receiver oscillators [118].

The PN compensation problem has been extensively studied in the past years [120, 121, 122, 123, 124, 125, 126, 127, 128, 129]. For instance, in [120] and [122], techniques for PN compensation are proposed for SISO systems. However, they assume a perfect knowledge of the CSI at the receiver, which may not be feasible in practice. In MIMO systems, the PN compensation becomes more challenging due to the presence of multiple independent phase-noise processes, i.e., one for each transmit and receive antenna. The authors of [123] propose a novel placement of pilot subcarriers in the preamble and data portions of the MIMO-OFDM frame for joint channel and PN estimation. The authors in [124, 125] propose compensation schemes based on the knowledge of the statistical model for the PN process.

In [126], a detailed study on the variance of the ICI as a function of the PN is provided, and an algorithm to compensate the so-called common phase error (CPE) and the ICI is formulated. The work [127] proposes a PN compensation method based on channel estimation via a linear time domain interpolation. In [128], the authors propose LS and weighted LS (WLS) methods for data, channel, and phase-noise tracking over a OFDM frame.

More recently, [129] presents a pilot signal design scheme for PN mitigation in mmWave MIMO-OFDM systems, where the combined channel and PN term is estimated and compensated for data detection. The work [121] proposes a PN compensation technique for high-frequency MIMO-OFDM systems using an LS method.

The use of tensor decompositions for modeling MIMO systems has been growing [18, 19, 28, 29, 130, 131, 132, 133, 134, 135, 136, 137], and more recently, has resulted in proposals of tensor-based receivers for MIMO-OFDM systems [35, 37, 38, 138, 139], However, these works do not take into account system impairments such as the phase-noise that leads to ICI. As discussed in these many references, the main reasons for using tensor-based modeling and signal processing are their ability to exploit the inherent multidimensional structure of the transmitted and/or received signals (e.g., time, frequency, space, polarization, etc.), as well as their built-in identifiability properties that allow us to derive blind or semi-blind receiver algorithms and

operate under more flexible conditions than matrix-based processing receivers. These key features are a natural consequence of the uniqueness properties of tensor decompositions compared to matrix decompositions [23].

In this chapter, we propose a tensor-based method for frequency-selective MIMO-OFDM channel, PN, and data estimation. By assuming that the PN is approximately constant over a very short symbol length, and motivated by the multidimensional structure of the received signal, a third-order PARAFAC (Parallel Factors) tensor model is developed for the received signal at the pilot subcarriers [25]. This model is exploited to separate the PN contribution from the channel. Then, we propose a two-stage receiver for joint channel, PN, and data estimation. In the first stage, we propose two algorithms to estimate the channel at the pilot subcarriers jointly with the PN impairments. The first one is an iterative solution based on the BALS, which consists of estimating the channel and phase-noise by solving two LS problems in an alternating way. The second one is a closed-form algorithm based on the least squares Khatri-Rao factorization (LSKRF) solution that solves multiple rank-one factorizations to jointly estimate the channel gains and phase-noise terms. The channel at the data subcarrieris is then obtained via interpolation. In the second stage, a zero-forcing (ZF) equalizer that exploits a PARATuck tensor structure of the signal is used to estimate the transmitted data. The identifiability conditions and computational complexity for both processing stages are also discussed.

Our simulation results show the effectiveness and high accuracy of the proposed receiver for the joint estimation of the channel, data, and PN impairments. We can summarize the main contributions of this chapter as follows:

1. A tensor decomposition based formulation to solve the problem of joint channel, PN, and data estimation in MIMO-OFDM systems, by assuming different PN perturbations for every pair of transmit and receive antenna. The proposed approach allows to separate the phase-noise from the channel gains, even without any CSI knowledge;
2. A two-stage receiver to jointly estimate the channels, PN terms, and data symbols. The first stage estimates the channel and the phase-noise (via BALS or LSKRF), while the second stage extracts the symbol estimates from a SKP formulation by means of a ZF filtering.

4.1 System Model

Let us consider a MIMO-OFDM system with M_T transmit antennas, M_R receive antennas, and F subcarriers. The total duration of an OFDM frame corresponds to K blocks of size L_P symbols each. We assume that each transmit and receive antenna is equipped with its own independent oscillator, so that the phase-noise (PN) is assumed to be different between the antennas and is constant within a block k, with $k = \{1, \ldots, K\}$. Note that the assumption that the transmit/receive antennas are subject to different PN perturbations has been addressed in the literature, such as in [119, 121, 128, 129]. As mentioned in [119, 140], this assumption copes

Figure 4.1 – MIMO system with antenna-dependent phase-noise impairments.

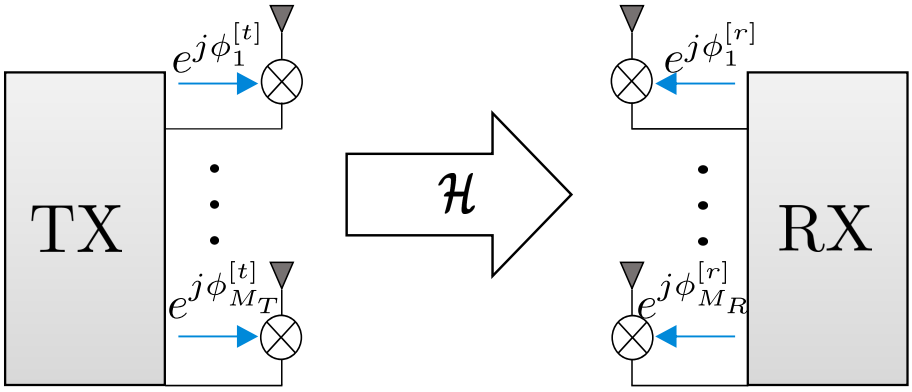

Source: Created by the author.

with realistic mmWave massive MIMO setups, including distributed MIMO scenarios.

Figure 4.1 illustrates the a MIMO system with antenna-dependent PN impairments. Let $h_{m_r,b}[n]$ and $s_{m_t,i}[n]$ be the discrete-time channel and the transmitted symbol, for $m_r = \{1,\ldots,M_R\}$, $m_t = \{1,\ldots,M_T\}$, $i = \{1,\ldots,L_P\}$. Then, the sampled discrete-time received signal at the period n, for n= $\{0,\ldots,F-1\}$, can be represented as

$$y_{m_r,i,k}[n] = e^{j\phi^{[\mathrm{r}]}_{k,m_r}[n]} h_{m_r,m_t}[n] \circledast e^{j\phi^{[\mathrm{t}]}_{k,m_t}[n]} s_{i,m_t}[n] + \upsilon_{m_r,i,k}[n], \tag{4.1}$$

where "$\circledast$" stands for time-domain convolution, $\phi^{(\mathrm{r})}_{k,m_r}[n]$ and $\phi^{(\mathrm{t})}_{k,m_t}[n]$ are the phase-noise (PN) impairment. Both are modeled as a Wiener process[1], i.e.,

$$\phi^{[\mathrm{x}]}_{k,m_\mathrm{x}}[n+1] = \phi^{[\mathrm{x}]}_{k,m_\mathrm{x}}[n] + \epsilon^{[\mathrm{x}]}_{k,m_\mathrm{x}}, \tag{4.2}$$

with $\epsilon^{[\mathrm{x}]}_{k,m_\mathrm{x}} \sim \mathcal{N}(0,\sigma^2_{\phi^{[\mathrm{x}]}})$, for $\mathrm{x} \in \{\mathrm{r},\mathrm{t}\}$. Moreover, $\upsilon_{m_r,i,k}[n]$ is the additive white Gaussian noise (AWGN) at the receiver $\sim \mathcal{CN}(0,\sigma^2_\upsilon)$. Applying the discrete Fourier transform (DFT), the received signal at the f-th subcarrier is given by

$$\begin{aligned} Y_{m_r,i,k}[f] &= \sum_{n=0}^{F-1} y_{m_r,i,k}[n] e^{-2j\pi fn/F} \\ Y_{m_r,i,k}[f] &= \Phi^{[\mathrm{r}]}_{k,m_r}[0] H_{m_r,m_t}[f] \Phi^{[\mathrm{t}]}_{k,m_t}[0] S_{m_t,i}[f] + V_{m_r,i,k}[f] \\ &\quad \underbrace{+\sum_{p=0,p\neq f}^{F-1} \Phi^{[\mathrm{r}]}_{k,m_r}[f-p] H_{m_r,m_t}[p] \sum_{q=0,q\neq f}^{F-1} \Phi^{[t]}_{k,m_t}[p-q] S_{m_t,i}[q]}_{\text{ICI components}} \end{aligned} \tag{4.3}$$

$$\begin{aligned} Y_{m_r,i,k}[f] &= \Phi^{[\mathrm{r}]}_{k,m_r}[0] H_{m_r,m_t}[f] \Phi^{[\mathrm{t}]}_{k,m_t}[0] S_{i,m_t}[f] + \\ &\quad G_{m_r,i,k}[f] + V_{m_r,i,k}[f], \end{aligned} \tag{4.4}$$

[1] The PN variance, $\sigma^2_{\phi^{[\mathrm{x}]}}$ is usually defined as $\sigma^2_{\phi^{[\mathrm{x}]}} = 4\pi\beta T_{sp}$, with β being the single-sided of the 3 dB bandwidth of the Lorentzian spectrum for $e^{j\phi^{[\mathrm{x}]}[n]}$ and T_{sp} is the sampling period [121, 141]. In this chapter, we assume a very high phase-noise variance $\sigma^2_{\phi^{[\mathrm{x}]}} = 5\cdot 10^{-3}\mathrm{rad}^2$.

where $f = \{0, \ldots, F-1\}$ is the subcarrier index in the frequency domain. The matrices $\Phi^{[\mathrm{r}]}_{k,m_r}[0] = \frac{1}{F}\sum_{n=0}^{F-1} e^{j\phi^{[\mathrm{r}]}_{k,m_r}[n]}$ and $\Phi^{[\mathrm{t}]}_{k,m_t}[0] = \frac{1}{F}\sum_{n=0}^{F-1} e^{j\phi^{[\mathrm{t}]}_{k,m_t}[n]}$ are the common phase error (CPE) generated by the receive and transmit antennas, respectively, and $G_{m_r,i,k}[f]$ is the inter-carrier interference (ICI) term. [2] For convenience, the detailed steps from equation (4.1) to (4.4) are given in the Appendix A.

The received signal $Y_{m_r,i,k}[f]$ is modelled as a fourth-order tensor $\mathcal{Y} \in \mathbb{C}^{M_R \times L_P \times K \times F}$ and we make use of the proposed tensor notation, introduced in Chapter 2, to develop our receivers. Let us introduce a combiner matrix $\boldsymbol{W} \in \mathbb{C}^{M_R \times M_R}$ that is assumed to be fixed over the K blocks and all F subcarriers. Resorting to the slice-wise notation, the received signal tensor $\mathcal{Y}_{..kf} \in \mathbb{C}^{M_R \times L_P}$ at the k-th block and f-th subcarrier can be written as

$$\mathcal{Y}_{..kf} = \boldsymbol{W}\mathrm{diag}_k\left(\Phi^{[\mathrm{r}]}[0]\right)\mathcal{H}_{..f}\mathrm{diag}_k\left(\Phi^{[\mathrm{t}]}[0]\right)\mathcal{S}^{\mathrm{T}}_{..f} + \boldsymbol{W}\mathcal{G}_{..kf} + \boldsymbol{W}\mathcal{V}_{..kf}, \tag{4.5}$$

where $\Phi^{[\mathrm{x}]}[0] \in \mathbb{C}^{K \times M_X}$, for $\mathrm{x} \in \{\mathrm{r}, \mathrm{t}\}$, is the phase-noise matrix formed by collecting the phase-noise CPE terms across the K blocks and the M_X antennas, i.e.,

$$\Phi^{[\mathrm{x}]}[0] = \begin{bmatrix} \Phi^{(\mathrm{x})}_{1,1}[0] & \ldots & \Phi^{(\mathrm{x})}_{1,M_X}[0] \\ \vdots & \ddots & \vdots \\ \Phi^{(\mathrm{x})}_{K,1}[0] & \ldots & \Phi^{(\mathrm{x})}_{K,M_X}[0] \end{bmatrix}. \tag{4.6}$$

The third-order tensor $\mathcal{S} \in \mathbb{C}^{L_P \times M_T \times F}$ is obtained by collecting the transmitted symbols $S_{i,m_t}[f]$ across all L_P symbol periods, M_T antennas and F subcarriers, for $i = \{1, \ldots, L_P\}$, $m_t = \{1, \ldots, M_T\}$, and $f = \{1, \ldots, F\}$.

In (4.5), $\mathcal{H}_{..f}$ represents the f-th frontal slice of the frequency-selective channel tensor $\mathcal{H} \in \mathbb{C}^{M_R \times M_T \times F}$, which, in Appendix A, is given by

$$\mathcal{H}_{a,b,f} = \sum_{l=1}^{L} \bar{h}_{a,b}[l] e^{-2j\pi f \tau_l d_{\mathrm{F}}}, \tag{4.7}$$

where $\bar{h}_{a,b}[l]$ is the channel gain of the l-th propagation path, $l = \{1, \ldots, L\}$, τ_l is the associated delay (in seconds), $d_{\mathrm{F}} = 1/T_s$ is the frequency spacing between two subcarriers (in Hertz), and T_s is the symbol duration.

In tensor notation, (4.5) can be considered as a special case of a fourth-order PARATuck model. However, in order to exploit the known factors at the receiver, i.e., the pilot matrix $\boldsymbol{S}^{(\mathrm{P})}$ and the combiner matrix $\boldsymbol{W}$, we will show how to recast such PARATuck model as an equivalent PARAFAC model for the joint phase-noise and channel estimation.

Figure 4.2 – Illustration of frame and block structures. The total frame length is $K \cdot L_P$.

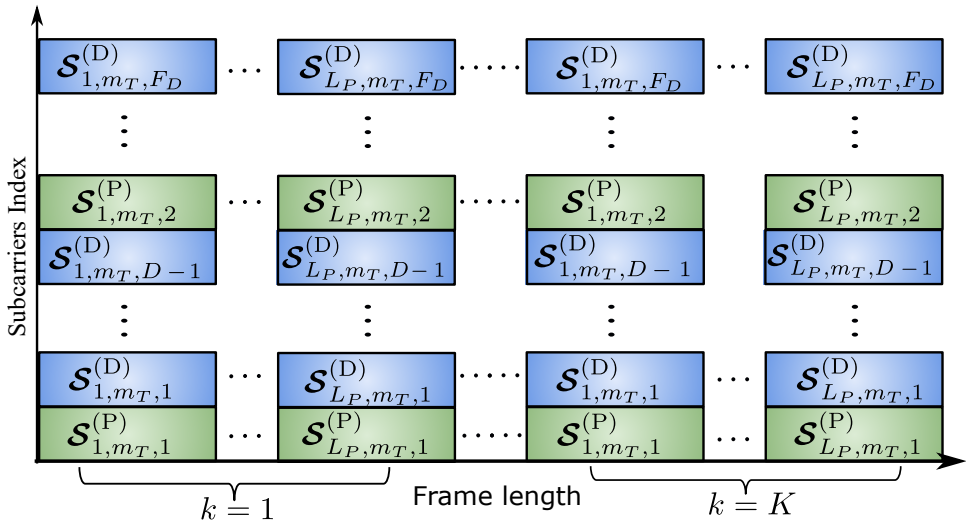

Source: Created by the author.

4.2 PARAFAC Pilot Modeling

The symbol tensor $\mathcal{S} \in \mathbb{C}^{L_P \times M_T \times F}$ is given by the concatenation of a pilot tensor $\mathcal{S}^{(\mathrm{P})} \in \mathbb{C}^{L_P \times M_T \times F_\mathrm{P}}$ and a data symbol tensor $\mathcal{S}^{(\mathrm{D})} \in \mathbb{C}^{L_P \times M_T \times F_\mathrm{D}}$, such that $F = F_\mathrm{P} + F_\mathrm{D}$, as illustrated in Figure 4.2. This concatenation depends on the value of $D = F/F_\mathrm{P}$, which is the distance between the pilot and data subcarriers, counted in indices. We can write the concatenation of the pilot and symbol tensors using the slice notation as

$$\mathcal{S} = \left[\mathcal{S}^{(\mathrm{P})}_{..1} \sqcup_3 \mathcal{S}^{(\mathrm{D})}_{..1:D-1} \sqcup_3 \ldots \sqcup_3 \mathcal{S}^{(\mathrm{P})}_{..F_\mathrm{P}} \sqcup_3 \mathcal{S}^{(\mathrm{D})}_{..D+F_\mathrm{P}:F_\mathrm{D}}\right]. \tag{4.8}$$

Likewise, the channel tensor $\mathcal{H}$ is divided into a pilot channel part $\mathcal{H}^{(\mathrm{P})} \in \mathbb{C}^{M_R \times M_T \times F_\mathrm{P}}$ and a data channel part $\mathcal{H}^{(\mathrm{D})} \in \mathbb{C}^{M_R \times M_T \times F_\mathrm{D}}$.

As a first step, the receiver extracts only the pilot preamble of each block. From (4.5), the contribution of the pilot part $\mathcal{Y}^{(\mathrm{P})}_{..kf_p} \in \mathbb{C}^{M_R \times L_P}$ associated with the k-th block at the f_p-th pilot subcarrier can be expressed as

$$\mathcal{Y}^{(\mathrm{P})}_{..kf_p} = \boldsymbol{W}\mathrm{diag}_k\left(\Phi^{[r]}[0]\right)\mathcal{H}^{(\mathrm{P})}_{..f_p}\mathrm{diag}_k\left(\Phi^{[t]}[0]\right)\mathcal{S}^{(\mathrm{P})\mathrm{T}}_{..f_p} + \boldsymbol{W}\mathcal{V}^{(\mathrm{P})}_{..kf_p} + \boldsymbol{W}\mathcal{G}^{(\mathrm{P})}_{..kf_p} \in \mathbb{C}^{M_R \times L_P}. \tag{4.9}$$

Let us consider that the same pilot is transmitted across all pilot subcarriers, i.e.,

$$\mathcal{S}^{(\mathrm{P})}_{..f_p} = \boldsymbol{S}^{(\mathrm{P})} \in \mathbb{C}^{L_P \times M_T} \ \forall f_p \in F_\mathrm{P}. \tag{4.10}$$

Then, we can write equation (4.9) as

$$\mathcal{Y}^{(\mathrm{P})}_{..kf_p} = \boldsymbol{W}\mathrm{diag}_k\left(\Phi^{[\mathrm{r}]}[0]\right)\mathcal{H}^{(\mathrm{P})}_{..f_p}\mathrm{diag}_k\left(\Phi^{[\mathrm{t}]}[0]\right)\boldsymbol{S}^{(\mathrm{P})\mathrm{T}} + \boldsymbol{W}\mathcal{V}^{(\mathrm{P})}_{..kf_p} + \boldsymbol{W}\mathcal{G}^{(\mathrm{P})}_{..kf_p}. \tag{4.11}$$

[2] Note that the ICI structure in eq. (4.3) consists of a summation of phase-noise, channel frequency responses, and OFDM symbols, and can be modeled as an AWGN process $\sim \mathcal{CN}(0, \sigma^2_{\mathrm{ICI}})$ [119], reducing the receiver complexity [121, 129]. In Appendix B, we derive an expression to calculate σ^2_{ICI}, which mainly depends on the phase-noise variance $\sigma^2_{\phi^{[\mathrm{x}]}}$ and the total number of subcarriers F.

Defining $\boldsymbol{y}_{kf_p}^{(\mathrm{P})} = \mathrm{vec}\left(\mathcal{Y}_{..kf_p}^{(\mathrm{P})}\right) \in \mathbb{C}^{M_R L_P \times 1}$, $\boldsymbol{h}_{f_p} = \mathrm{vec}(\mathcal{H}_{..f_p}^{(\mathrm{P})}) \in \mathbb{C}^{M_R M_T \times 1}$ and applying properties (2.10)-(2.14) to (4.11), neglecting the noise and the ICI terms, yields

$$\begin{aligned}
\boldsymbol{y}_{kf_p}^{(\mathrm{P})} &= \left(\boldsymbol{S}^{(\mathrm{P})} \otimes \boldsymbol{W}\right) \mathrm{vec}\left(\mathrm{diag}_k\left(\Phi^{[\mathrm{r}]}[0]\right) \mathcal{H}_{..f_p}^{(\mathrm{P})} \mathrm{diag}_k\left(\Phi^{[\mathrm{t}]}[0]\right)\right) \\
&= \left(\boldsymbol{S}^{(\mathrm{P})} \otimes \boldsymbol{W}\right) \left(\mathrm{diag}_k\left(\Phi^{[\mathrm{t}]}[0]\right) \otimes \mathrm{diag}_k\left(\Phi^{[\mathrm{r}]}[0]\right)\right) \boldsymbol{h}_{f_p}^{(\mathrm{P})} \\
&= \left(\boldsymbol{h}_{f_p}^{(\mathrm{P})\mathrm{T}} \diamond (\boldsymbol{S}^{(\mathrm{P})} \otimes \boldsymbol{W})\right) \left(\Phi^{[\mathrm{t}]}[0]_{k.} \otimes \Phi^{[\mathrm{r}]}[0]_{k.}\right)^{\mathrm{T}} \\
&= \left(\boldsymbol{S}^{(\mathrm{P})} \otimes \boldsymbol{W}\right) \mathrm{diag}\left(\boldsymbol{h}_{f_p}^{(\mathrm{P})}\right) \boldsymbol{\phi}_{k.}^{\mathrm{T}}
\end{aligned} \tag{4.12}$$

where $\boldsymbol{\phi}_{k.} = \Phi^{[\mathrm{t}]}[0]_{k.} \otimes \Phi^{[\mathrm{r}]}[0]_{k.} \in \mathbb{C}^{1 \times M_R M_T}$ is the combined transmitter and receiver phase-noise at the k-th block. Collecting the vectorized received pilots $\boldsymbol{y}_{kf_p}^{(\mathrm{P})}$ for all the $k = 1, \ldots, K$ blocks as the columns of the resulting matrix $\boldsymbol{Y}_{f_p}^{(\mathrm{P})} = \left[\boldsymbol{y}_{1,f_p}^{(\mathrm{P})}, \ldots, \boldsymbol{y}_{K,f_p}^{(\mathrm{P})}\right]$, and according to the definition of the Khatri-Rao product, we have

$$\begin{aligned}
\boldsymbol{Y}_{f_p}^{(\mathrm{P})} &= \left(\boldsymbol{S}^{(\mathrm{P})} \otimes \boldsymbol{W}\right) \mathrm{diag}\left(\boldsymbol{h}_{f_p}^{(\mathrm{P})}\right) \left[\boldsymbol{\phi}_{1.}^{\mathrm{T}}, \ldots, \boldsymbol{\phi}_{K.}^{\mathrm{T}}\right] \\
&= \left(\boldsymbol{S}^{(\mathrm{P})} \otimes \boldsymbol{W}\right) \mathrm{diag}\left(\boldsymbol{h}_{f_p}^{(\mathrm{P})}\right) \Phi^{\mathrm{T}} \in \mathbb{C}^{M_R L_P \times K},
\end{aligned} \tag{4.13}$$

where $\Phi = \left(\Phi^{[t]\mathrm{T}}[0] \diamond \Phi^{[r]\mathrm{T}}[0]\right)^{\mathrm{T}} \in \mathbb{C}^{K \times M_R M_T}$ is the combined phase-noise concatenated across all the K blocks and antennas. According to (2.57), $\boldsymbol{Y}_{f_p}^{(\mathrm{P})}$ can be interpreted as the f_p-th frontal slice of the third-order tensor $\mathcal{Y}^{(\mathrm{P})} \in \mathbb{C}^{M_R L_P \times K \times F_\mathrm{P}}$ which corresponds to the following PARAFAC decomposition

$$\mathcal{Y}^{(\mathrm{P})} = \mathcal{I}_{3,M_R M_T} \times_1 (\boldsymbol{S}^{(\mathrm{P})} \otimes \boldsymbol{W}) \times_2 \Phi \times_3 [\mathcal{H}]_{(3)}^{(\mathrm{P})}, \tag{4.14}$$

where $[\mathcal{H}]_{(3)}^{(\mathrm{P})} \in \mathbb{C}^{F_\mathrm{P} \times M_R M_T}$ is the 3-mode unfolding of the pilot channel tensor $\mathcal{H}^{(\mathrm{P})} \in \mathbb{C}^{M_R \times M_T \times F_\mathrm{P}}$. The 1-mode, 2-mode and 3-mode unfoldings of $\mathcal{Y}^{(\mathrm{P})}$, denoted by $\left[\mathcal{Y}^{(\mathrm{P})}\right]_{(1)}$, $\left[\mathcal{Y}^{(\mathrm{P})}\right]_{(2)}$ and $\left[\mathcal{Y}^{(\mathrm{P})}\right]_{(3)}$ respectively, admit the following factorizations:

$$\left[\mathcal{Y}^{(\mathrm{P})}\right]_{(1)} = \left(\boldsymbol{S}^{(\mathrm{P})} \otimes \boldsymbol{W}\right) \left([\mathcal{H}]_{(3)}^{(\mathrm{P})} \diamond \Phi\right)^{\mathrm{T}} \in \mathbb{C}^{M_R L_P \times K F_\mathrm{P}}, \tag{4.15}$$

$$\left[\mathcal{Y}^{(\mathrm{P})}\right]_{(2)} = \Phi \left([\mathcal{H}]_{(3)}^{(\mathrm{P})} \diamond \left(\boldsymbol{S}^{(\mathrm{P})} \otimes \boldsymbol{W}\right)\right)^{\mathrm{T}} \in \mathbb{C}^{K \times M_R L_P F_\mathrm{P}}, \tag{4.16}$$

$$\left[\mathcal{Y}^{(\mathrm{P})}\right]_{(3)} = [\mathcal{H}]_{(3)}^{(\mathrm{P})} \left(\Phi \diamond \left(\boldsymbol{S}^{(\mathrm{P})} \otimes \boldsymbol{W}\right)\right)^{\mathrm{T}} \in \mathbb{C}^{F_\mathrm{P} \times M_R L_P K}. \tag{4.17}$$

Equations (4.15)-(4.17) are the basis for the first-stage of the proposed receiver, where two different algorithms can be used to estimate the combined phase-noise and the pilot channel.

4.3 Proposed Receiver

The proposed tensor-based receiver is composed of two processing stages. In the first stage, two different algorithms are derived to estimate the channel at the pilot subcarriers

and the phase-noise (PN) impairments. The first algorithm is based on bilinear alternating least squares (BALS), and consists of estimating the channel from the pilot subcarriers and the PN terms in an iterative way, while the second one has a closed-form solution based on the least squares Khatri-Rao factorization (LSKRF) for simultaneous channel and phase-noise estimation. Once the channel coefficients associated with the pilot subcarriers are estimated, the channel coefficients at the data subcarriers are obtained by interpolating the estimated channel at the pilot subcarriers. In the second stage, the proposed zero forcing selective Kronecker product (ZFSKP) receiver, a zero-forcing (ZF) approach based on the selective Kronecker product (SKP) formulation , is used to estimate the data symbols. These two stages are detailed below.

4.3.1 Stage 1*: Channel and PN estimation via BALS*

The first stage of the proposed receiver consists of jointly estimating the channel and PN impairments from the received signal tensor in (4.14), which can be done by exploiting the unfoldings $\left[\mathcal{Y}^{(\mathrm{P})}\right]_{(2)}$ and $\left[\mathcal{Y}^{(\mathrm{P})}\right]_{(3)}$ from equations (4.16) and (4.17), respectively. To this end, we make use of the BALS algorithm that alternates between the estimation of the factor matrices $[\mathcal{H}]^{(\mathrm{P})}_{(3)}$ and Φ by optimizing the following two least squares (LS) criteria:

$$\left[\hat{\mathcal{H}}\right]^{(\mathrm{P})}_{(3)} = \underset{[\mathcal{H}]^{(\mathrm{P})}_{(3)}}{\operatorname{argmin}} \left\| \left[\mathcal{Y}^{(\mathrm{P})}\right]_{(3)} - \left[\hat{\mathcal{H}}\right]^{(\mathrm{P})}_{(3)} \left(\Phi \diamond \left(\boldsymbol{S}^{(\mathrm{P})} \otimes \boldsymbol{W}\right)\right)^{\mathrm{T}} \right\|^2_{\mathrm{F}},$$

$$\hat{\Phi} = \underset{\Phi}{\operatorname{argmin}} \left\| \left[\mathcal{Y}^{(\mathrm{P})}\right]_{(2)} - \Phi \left([\mathcal{H}]^{(\mathrm{P})}_{(3)} \diamond \left(\boldsymbol{S}^{(\mathrm{P})} \otimes \boldsymbol{W}\right)\right)^{\mathrm{T}} \right\|^2_{\mathrm{F}},$$

the solutions of which are given, respectively, by

$$\left[\hat{\mathcal{H}}\right]^{(\mathrm{P})}_{(3)} = \left[\mathcal{Y}^{(\mathrm{P})}\right]_{(3)} \left[\left(\Phi \diamond \left(\boldsymbol{S}^{(\mathrm{P})} \otimes \boldsymbol{W}\right)\right)^{\mathrm{T}}\right]^{+} \tag{4.18}$$

$$\hat{\Phi} = \left[\mathcal{Y}^{(\mathrm{P})}\right]_{(2)} \left[\left([\mathcal{H}]^{(\mathrm{P})}_{(3)} \diamond \left(\boldsymbol{S}^{(\mathrm{P})} \otimes \boldsymbol{W}\right)\right)^{\mathrm{T}}\right]^{+}. \tag{4.19}$$

Due to the knowledge of $\boldsymbol{W}$ and $\boldsymbol{S}^{(\mathrm{P})}$ at the receiver, each iteration of the BALS algorithm contains only two updating steps. At each step, the fitting error is minimized with respect to one factor matrix by fixing the other to its value obtained at the previous updating step. This procedure is repeated until the convergence of the BALS stage at the i-th iteration. The convergence is declared when $|e_{(i)} - e_{(i-1)}| \leq 10^{-6}$, where $e_{(i)}$ denotes the residual error calculated as

$$e_{(i)} = \frac{\left\| \mathcal{Y}^{(\mathrm{P})} - \hat{\mathcal{Y}}^{(\mathrm{P})}_{(i)} \right\|^2_{\mathrm{F}}}{\left\| \mathcal{Y}^{(\mathrm{P})} \right\|^2_{\mathrm{F}}}, \tag{4.20}$$

where $\hat{\mathcal{Y}}^{(\mathrm{P})}_{(i)}$ is the reconstructed tensor $\mathcal{Y}^{(\mathrm{P})}$ computed from the estimated factor matrices at the end of the i-th iteration.

Algorithm 6 Stage1: BALS

1: **Inputs**: Received tensor pilot signal $\mathcal{Y}^{((\mathrm{P})}$, pilot matrix $\boldsymbol{S}^{(\mathrm{P})}$, and combiner $\boldsymbol{W}$.
2: Generate $\hat{\phi}^{[r]}[n] \sim \mathcal{N}\left(0, \sigma^2_{\phi^{[\mathrm{r}]}}\right)$ and $\hat{\phi}^{[t]}[n] \sim \mathcal{N}\left(0, \sigma^2_{\phi^{[\mathrm{t}]}}\right)$ using the Wiener model;
3: Set $\hat{\Phi}^{[r]}_{k,m_r}[0] = 1/F \sum_{n=0}^{F-1} e^{j\hat{\phi}^{[r]}_{k,m_r}[n]}$ and $\hat{\Phi}^{[t]}_{k,m_t}[0] = 1/F \sum_{n=0}^{F-1} e^{j\hat{\phi}^{[t]}_{k,m_t}[n]}$;
4: Iteration $i = 0$;
5: Set $\hat{\Phi}_{(0)} = \hat{\Phi}^{[t]\mathrm{T}}[0] \diamond \hat{\Phi}^{[r]\mathrm{T}}[0]$;
6: $i = i + 1$;
7: Compute an estimation for $\left[\hat{\mathcal{H}}\right]^{(\mathrm{P})}_{(3)(i)}$ using

$$\left[\hat{\mathcal{H}}\right]^{(\mathrm{P})}_{(3)(i)} = \left[\mathcal{Y}^{(\mathrm{P})}\right]_{(3)} \left[\left(\hat{\Phi}_{(i-1)} \diamond \left(\boldsymbol{S}^{(\mathrm{P})} \otimes \boldsymbol{W}\right)\right)^{\mathrm{T}}\right]^{+},$$

8: Compute an estimation for $\hat{\Phi}_{(i)}$ using

$$\hat{\Phi}_{(i)} = \left[\mathcal{Y}^{(\mathrm{P})}\right]_{(2)} \left[\left(\left[\hat{\mathcal{H}}\right]^{(\mathrm{P})}_{(3)(i)} \diamond \left(\boldsymbol{S}^{(\mathrm{P})} \otimes \boldsymbol{W}\right)\right)^{\mathrm{T}}\right]^{+},$$

9: Reconstruct tensor $\hat{\mathcal{Y}}^{(\mathrm{P})}_{(i)}$ and compute the residual error according to equation (4.20);
10: Return to step 5 and repeat until convergence;
11: Estimate the channel at the data subcarriers $\left[\hat{\mathcal{H}}\right]^{(\mathrm{D})}_{(3)}$ by interpolating $\left[\hat{\mathcal{H}}\right]^{(\mathrm{P})}_{(3)}$;
12: **Outputs**: Estimated combined PN matrix $\hat{\Phi}$, and channels $\left[\hat{\mathcal{H}}\right]^{(\mathrm{P})}_{(3)}$, and $\left[\hat{\mathcal{H}}\right]^{(\mathrm{D})}_{(3)}$.

Note that, for the initialization of Algorithm 6, we consider that the phase-noise variance is known at the receiver. This assumption is realistic if we note that the phase-noise variance parameters (β and T_{sp}) are usually known at the receiver, or can be considered known in advance, since they are intrinsic parameters of the oscillators and fixed by the system design [128].

4.3.2 Stage 1*: Channel and PN estimation via LS-KRF*

The proposed least squares Khatri-Rao factorization (LSKRF) algorithm estimates the channel at the pilot subcarriers and the PN contributions in a closed-form manner. Transposing the unfolding $[\mathcal{Y}]^{(\mathrm{P})}_{(1)}$ in (4.15), and applying a pseudo-inverse at the right, we have

$$[\mathcal{H}]^{(\mathrm{P})}_{(3)} \diamond \Phi \approx \left[\mathcal{Y}^{(\mathrm{P})}\right]^{\mathrm{T}}_{(1)} \left(\boldsymbol{S}^{(\mathrm{P})\mathrm{T}} \otimes \boldsymbol{W}^{\mathrm{T}}\right)^{+}. \tag{4.21}$$

Note that the uniqueness of the Khatri-Rao product term in (4.21) requires that $\boldsymbol{S}^{(\mathrm{P})\mathrm{T}} \otimes \boldsymbol{W}$ to be full-column rank, which implies $L_P \geq M_T$.

Let us define $\boldsymbol{Z} \approx [\mathcal{H}]^{(\mathrm{P})}_{(3)} \diamond \Phi \in \mathbb{C}^{KF_{\mathrm{P}} \times M_R M_T}$ and note that the r-th column of $\boldsymbol{Z}$, defined

Algorithm 7 Stage 1 LSKRF

1: **Inputs**: Received 1-mode pilot tensor signal $[\mathcal{Y}]_{(1)}^{((\mathrm{P})}$, pilot matrix $\boldsymbol{S}^{(\mathrm{P})}$, and combiner $\boldsymbol{W}$.
2: Compute an estimate of $\boldsymbol{Z}$ as

$$\hat{\boldsymbol{Z}} = \left[\mathcal{Y}^{(\mathrm{P})}\right]_{(1)}^{\mathrm{T}} \left(\boldsymbol{S}^{(\mathrm{P})\mathrm{T}} \otimes \boldsymbol{W}^{\mathrm{T}}\right)^{+}.$$

3: **for** $r = 1 : M_R M_T$ **do**
4: Define $\bar{\boldsymbol{Z}}^{(r)} = \mathrm{unvec}_{K\times F_\mathrm{P}}(\hat{\boldsymbol{Z}}_{.r})$.
5: Compute the SVD of $\overline{Z} = \boldsymbol{U}^{(r)}\Sigma^{(r)}\boldsymbol{V}^{(r)\mathrm{H}}$.
6: Estimate $\hat{\Phi}_{.r} = \left(\Sigma_{1,1}^{(r)}\right)^{1/2}\boldsymbol{U}_{.1}^{(r)}$
7: Estimate $\left[\hat{\mathcal{H}}\right]_{(3).r}^{(\mathrm{P})} = \left(\Sigma_{1,1}^{(r)}\right)^{1/2}\boldsymbol{V}_{.1}^{(r)*}$.
8: **end for**
9: Estimate the channel at the data subcarriers $\left[\hat{\mathcal{H}}\right]_{(3)}^{(\mathrm{D})}$ by interpolating $\left[\hat{\mathcal{H}}\right]_{(3)}^{(\mathrm{P})}$;
10: **Outputs**: Estimated combined PN matrix $\hat{\Phi}$, and channels $\left[\hat{\mathcal{H}}\right]_{(3)}^{(\mathrm{P})}$, and $\left[\hat{\mathcal{H}}\right]_{(3)}^{(\mathrm{D})}$.

as $\boldsymbol{Z}_{.r} \approx [\mathcal{H}]_{(3).r}^{(\mathrm{P})} \otimes \Phi_{.r} \in \mathbb{C}^{KF_\mathrm{P}}$, with $r = \{1, \ldots, M_R M_T\}$. From Property (2.14), we have

$$\mathrm{vec}\left(\Phi_{.r} \circ [\mathcal{H}]_{(3).r}^{(\mathrm{P})}\right) = [\mathcal{H}]_{(3).r}^{(\mathrm{P})} \otimes \Phi_{.r} \approx \boldsymbol{Z}_{.r} \in \mathbb{C}^{KF_\mathrm{P}\times 1}. \tag{4.22}$$

Applying the unvec(·) operator, we defined

$$\bar{\boldsymbol{Z}}^{(r)} = \mathrm{unvec}_{K\times F_\mathrm{P}}\left(\boldsymbol{Z}_{.r}\right) \approx \Phi_{.r} \cdot [\mathcal{H}]_{(3).r}^{(\mathrm{P})\mathrm{T}} \in \mathbb{C}^{K\times F_\mathrm{P}}. \tag{4.23}$$

Hence, an estimation of $\Phi_{.r}$ and $[\mathcal{H}]_{(3).r}^{(\mathrm{P})\mathrm{T}}$ can be obtained, respectively, from the dominant left and right singular vectors of $\bar{\boldsymbol{Z}}^{(r)} = \boldsymbol{U}^{(r)}\Sigma^{(r)}\boldsymbol{V}^{(r)\mathrm{H}}$, i.e.,

$$\hat{\Phi}_{.r} = \left(\Sigma_{1,1}^{(r)}\right)^{1/2}\boldsymbol{U}_{.1}^{(r)} \tag{4.24}$$

$$\left[\hat{\mathcal{H}}\right]_{(3).r}^{(\mathrm{P})} = \left(\Sigma_{1,1}^{(r)}\right)^{1/2}\boldsymbol{V}_{.1}^{(r)*}, \tag{4.25}$$

$r = 1, \ldots, M_R M_T$. The estimation of the entire matrices $\hat{\Phi}$ and $\left[\hat{\mathcal{H}}\right]_{(3)}^{(\mathrm{P})}$ requires the computation of $M_R M_T$ rank-one matrix approximations. Instead of computing SVDs, efficient solutions based on the power method can be used [142].

4.3.3 Scaling ambiguity in the estimated parameters at Stage 1

It is important to mention that, after the BALS and the LSKRF in Stage 1, the estimated matrices are linked to the true ones by the following relationship:

$$\left[\hat{\mathcal{H}}\right]_{(3)}^{(\mathrm{P})} = [\mathcal{H}]_{(3)}^{(\mathrm{P})}\Lambda, \quad \hat{\Phi} = \Phi\Lambda^{-1}, \tag{4.26}$$

where $\Lambda = \text{diag}(\boldsymbol{\lambda}) \in \mathbb{C}^{M_R M_T \times M_R M_T}$, with $\boldsymbol{\lambda} = \left[\alpha_1, \ldots, \alpha_{M_R M_T}\right]$ being a vector containing $M_R M_T$ scaling factors. To solve these scaling ambiguities, one row of Φ or $[\mathcal{H}]^{(\text{P})}_{(3)}$ has to be known, which physically means that the phase-noise process at a certain block k is known, or, alternatively, that the CSI at a certain pilot subcarrier f_p is available. However, since we are interested in data estimation, the scaling factors affecting the channel matrix are canceled with the ones acting over the phase-noise matrix, i.e., $\Lambda\Lambda^{-1} = \boldsymbol{I}_{M_R M_T}$. Thus, the role of the BALS and the LS-KRF algorithms is to decouple and refine the estimates of the channel and phase-noise matrices before combining them for the data estimation, according to eq. (4.31).

4.3.4 Stage 2: Data estimation using the ZFSKP approach

We derive an SKP-based ZF approach, namely zero forcing selective Kronecker product (ZFSKP), to estimate the transmitted symbol tensor from the data subcarriers. Let us consider the received signal at the k-th frame and f_d-th data subcarrier in equation (4.5). By defining $\boldsymbol{y}^{(\text{D})}_{kf_d} \doteq \text{vec}(\mathcal{Y}^{(\text{D})}_{..kf_d}) \in \mathbb{C}^{M_R L_P \times 1}$ and $\boldsymbol{h}^{(\text{D})}_{f_d} = \text{vec}(\mathcal{H}^{(\text{D})}_{..f_d}) \in \mathbb{C}^{M_R M_T \times 1}$, and neglecting the noise and the ICI terms (for notational convenience), we have

$$\begin{aligned}\boldsymbol{y}^{(\text{D})}_{kf_d} &= \text{vec}\left(\boldsymbol{W} D_k\left(\Phi^{[\text{r}]}[0]\right)\mathcal{H}^{(\text{D})}_{..f_d} D_k\left(\Phi^{[\text{t}]}[0]\right)\mathcal{S}^{(\text{D})\text{T}}_{..f_d}\right)\\ &= \left(\mathcal{S}^{(\text{D})}_{..f_d} \otimes \boldsymbol{W}\right)\text{diag}(\boldsymbol{h}^{(\text{D})}_{f_d})\left(\Phi^{[\text{t}]}[0]_{k.} \otimes \Phi^{[\text{r}]}[0]_{k.}\right)^{\text{T}}.\end{aligned}$$

By collecting data during the K frames, we obtain

$$\boldsymbol{Y}^{(\text{D})}_{f_d} = \left(\mathcal{S}^{(\text{D})}_{..f_d} \otimes \boldsymbol{W}\right)\text{diag}(\boldsymbol{h}^{(\text{D})}_{f_d})\Phi^{\text{T}} \in \mathbb{C}^{M_R L_P \times K}. \tag{4.27}$$

Note that (4.27) differs from (4.13) since the term $\mathcal{S}^{(\text{D})}_{..f_d}$ varies over the F_D subcarriers, which means that equation (4.27) does not fit a PARAFAC model. However, by collecting all the F_D terms in $\boldsymbol{Y}^{(\text{D})} = [\boldsymbol{Y}^{(\text{D})}_1 \ldots \boldsymbol{Y}^{(\text{D})}_{F_\text{D}}] \in \mathbb{C}^{M_R L_P \times K F_\text{D}}$, we get

$$\begin{aligned}\boldsymbol{Y}^{(\text{D})} &= \left[\left(\mathcal{S}^{(\text{D})}_{..1} \otimes \boldsymbol{W}\right), \ldots, \left(\mathcal{S}^{(\text{D})}_{..F_\text{D}} \otimes \boldsymbol{W}\right)\right]\text{diag}\left(\begin{bmatrix}\boldsymbol{h}^{(\text{D})}_1\\ \vdots\\ \boldsymbol{h}^{(\text{D})}_{F_D}\end{bmatrix}\right)\begin{bmatrix}\Phi & & \\ & \ddots & \\ & & \Phi\end{bmatrix}^{\text{T}}\\ &= \left([\mathcal{S}]^{(\text{D})}_{(1)} \otimes \boldsymbol{W}\right)\text{diag}\left(\text{vec}([\mathcal{H}]^{(\text{D})\text{T}}_{(3)})\right)\left(\boldsymbol{I}_{F_\text{D}} \otimes \Phi\right)^{\text{T}}.\end{aligned} \tag{4.28}$$

The received data matrix $\boldsymbol{Y}^{(\text{D})} \in \mathbb{C}^{M_R L_P \times K F_\text{D}}$ can be interpreted as a generalized unfolding of the fourth-order received data tensor $\mathcal{Y}^{(\text{D})} \in \mathbb{C}^{M_R \times L_P \times K \times F_\text{D}}$ given by

$$\mathcal{Y}^{(\text{D})} = \overline{\mathcal{H}}^{(\text{D})} \times_1 \boldsymbol{W} \times_2 [\mathcal{S}]^{(\text{D})}_{(1)} \times_3 \Phi \times_4 \boldsymbol{I}_{F_\text{D}}, \tag{4.29}$$

where $\overline{\mathcal{H}}^{(\text{D})}$ is the core tensor of the data received signal, which corresponds to a reshaping of the elements of $\text{diag}(\text{vec}([\mathcal{H}]^{(\text{D})\text{T}}_{(3)})) \in \mathbb{C}^{M_R M_T F_\text{D} \times M_R M_T F_\text{D}}$ as a fourth-order tensor $\overline{\mathcal{H}}^{(\text{D})} \in$

Algorithm 8 Stage 1 LSKRF

1: **Inputs**: Received data tensor $\mathcal{Y}^{(\mathrm{D})}$, and the outputs of Algorithm 6 or 7.
2: Reshape the elements of diag(vec$\left(\left[\hat{\mathcal{H}}\right]_{(3)}^{(\mathrm{D})\mathrm{T}}\right)$ into $\overline{\mathcal{H}}^{(\mathrm{D})}$ using (4.30).
3: Estimate the transmitted data as

$$\left[\hat{\mathcal{S}}\right]_{(1)}^{(\mathrm{D})} = [\mathcal{Y}]_{(2)}^{(\mathrm{D})} \left(\left[\hat{\overline{\mathcal{H}}}\right]_{(2)}^{(\mathrm{D})} (\boldsymbol{I}_{F_{\mathrm{D}}} \otimes \hat{\Phi} \otimes \boldsymbol{W})^{\mathrm{T}}\right)^{+}, \tag{4.32}$$

4: **Outputs**: Estimated symbols $\left[\hat{\mathcal{S}}\right]_{(1)}^{(\mathrm{D})} \in \mathbb{C}^{L_{\mathrm{P}} \times M_T F_{\mathrm{D}}}$.

$\mathbb{C}^{M_R \times M_T F_{\mathrm{D}} \times M_R M_T \times F_{\mathrm{D}}}$ that can be constructed similar to the using the SKP structure introduced in Section 2.2.9 as

$$\overline{\mathcal{H}}^{(\mathrm{D})} = \left(\underbrace{\mathcal{I}_{3,F_{\mathrm{D}}} \otimes_{2,3}^{2,4} \left(\mathcal{I}_{3,M_T} \otimes_{2,3}^{2,3} \mathcal{I}_{3,M_R}\right)}_{\in \mathbb{R}^{M_R \times M_T F_{\mathrm{D}} \times M_R M_T \times M_R M_T F_{\mathrm{D}} \times F_{\mathrm{D}}}}\right) \times_4 \mathrm{vec}\left([\mathcal{H}]_{(3)}^{(\mathrm{D})\mathrm{T}}\right)^{\mathrm{T}}. \tag{4.30}$$

From equation (4.29), an estimate of the data symbol tensor can be obtained as

$$\left[\hat{\mathcal{S}}\right]_{(1)}^{(\mathrm{D})} = [\mathcal{Y}]_{(2)}^{(\mathrm{D})} \left(\left[\hat{\overline{\mathcal{H}}}\right]_{(2)}^{(\mathrm{D})} (\boldsymbol{I}_{F_{\mathrm{D}}} \otimes \hat{\Phi} \otimes \boldsymbol{W})^{\mathrm{T}}\right)^{+}, \tag{4.31}$$

where $\hat{\Phi}$ is the PN matrix estimated in the first stage, and $\left[\hat{\overline{\mathcal{H}}}\right]_{(2)}^{(\mathrm{D})}$ is the 2-mode unfolding of the tensor $\overline{\mathcal{H}}^{(\mathrm{D})}$. The ZFSKP receiver is summarized in Algorithm 8.

4.3.5 Uniqueness and Identifiability Conditions

In this section, we discuss the range of parameter settings that ensure the uniqueness and identifiability of the proposed receiver. First, recall equation (2.59), where the uniqueness condition for a third-order PARAFAC model is stated. Adapting this condition to our system context, we can rewrite (2.59) as

$$k_{(\boldsymbol{S}^{(\mathrm{P})} \otimes \boldsymbol{W})} + k_{\Phi} + k_{[\mathcal{H}]_{(3)}^{(\mathrm{P})}} \geq 2(M_R M_T) + 2. \tag{4.33}$$

Since the factor $\boldsymbol{S}^{(\mathrm{P})} \otimes \boldsymbol{W} \in \mathbb{C}^{M_R L_P \times M_R M_T}$ is known at the receiver, we can ensure by a proper design such that $\boldsymbol{S}^{(\mathrm{P})} \otimes \boldsymbol{W}$ has full rank, so that $k_{(\boldsymbol{S}^{(\mathrm{P})} \otimes \boldsymbol{W})} = \mathrm{rank}\left(\boldsymbol{S}^{(\mathrm{P})} \otimes \boldsymbol{W}\right) = M_R M_T$. The factor $[\mathcal{H}]_{(3)}^{(\mathrm{P})} \in \mathbb{C}^{F_{\mathrm{P}} \times M_R M_T}$ can also be assumed to be a full rank matrix under a rich scattering propagation environment, which implies that $k_{[\mathcal{H}]_{(3)}^{(\mathrm{P})}} = \mathrm{rank}\left([\mathcal{H}]_{(3)}^{(\mathrm{P})}\right) = M_R M_T$. Under these assumptions, we can deduce from (4.33) that $k_{\Phi} \geq 2$ is enough to ensure the uniqueness of model (2.59) and, hence, to guarantee a joint channel and phase-noise recovery.

Finally, note that LS estimation steps 7 and 8 of Algorithm 6 require that $FL_P \geq M_T$ and $KL_P \geq M_T$, while the ZF estimation of the data symbols in (4.31) requires that $M_T \leq M_R K$.

4.3.6 Computational Complexity

Here we derive the computational complexity of the proposed receiver in terms of FLOPS (Floating-point Operations Per Second). Considering a matrix $\boldsymbol{A} \in \mathbb{C}^{M\times N}$, we know that the computation of its dominant singular value and singular vectors have a cost of $O(l\cdot(N^2M + M^2N))$, where l is the maximum number of iterations of the power method (see [142]). In our experiments, we have noted that $l = 1$ is enough to achieve a good accuracy. Moreover, we know that $O(N^2M)$ operations are required to compute the pseudo-inverse of $\boldsymbol{A}$, with $N < M$. Using these results, we find that Stage 1 via BALS has a complexity of order $O(I\cdot 2\left((M_RM_T)^2M_RL_P(F_\mathrm{P}+K)\right))$, where I is the number of iterations required to achieve the convergence. If the LS-KRF is used in Stage 1, we have a complexity of $O(M_RM_T\,(F_\mathrm{P}K(F_\mathrm{P}+K)))$. Finally, the complexity associated with the data symbol estimation in Stage 2 is given by $O\left((F_\mathrm{D}M_T)^3\right)$.

4.4 Simulation Results

We evaluate the performance of the proposed receiver in terms of the normalized mean square error (NMSE) between the estimated and true frequency-selective MIMO channel and the combined phase-noise matrix, and transmitted symbol error rate (SER). Our simulation results represent an average over $M = 5000$ independent Monte Carlo runs. Each run corresponds to an independent realization of the channel, pilots, data, additive white Gaussian noise (AWGN), ICI, and PN. The transmitted symbols are normalized such that the SNR $= \frac{1}{\sigma_v^2}$ is controlled by varying the noise power σ_v^2 of the AWGN tensor $\mathcal{V}$, while the variance of the ICI σ_{ICI}^2 is kept constant, since it depends on the variance of the phase-noise and on the number of subcarriers, as detailed in the Appendix B. The combiner matrix $\boldsymbol{W} \in \mathbb{C}^{M_R\times M_R}$ is designed as a DFT matrix. The NMSE is defined as

$$\mathrm{NMSE}(\hat{\mathcal{H}}^{(\mathrm{D})}) = \frac{1}{M}\sum_{m=1}^{M}\frac{\|\mathcal{H}^{(\mathrm{D})} - \hat{\mathcal{H}}^{(\mathrm{D})}\|_\mathrm{F}^{\,2}}{\|\mathcal{H}^{(\mathrm{D})}\|_\mathrm{F}}, \tag{4.34}$$

$$\mathrm{NMSE}(\hat{\Phi}) = \frac{1}{M}\sum_{m=1}^{M}\frac{\|\Phi - \hat{\Phi}\|_\mathrm{F}^{\,2}}{\|\Phi\|_\mathrm{F}}, \tag{4.35}$$

The pilots and data symbols follow a 4-QAM constellation. For the channel model in (4.7), the coefficients $\{h[l]\}$ are i.i.d. complex Gaussian random variables with zero mean and unit variance. The number of propagation paths is equal to $L = 16$, and the frequency spacing between two subcarriers is $d_\mathrm{F} = 15$ kilo-Hertz (kHz). The path delays are chosen as $\tau_l = \mathrm{DS}\cdot\upsilon_l$, where υ_l is a random variable that follows a normal distribution with $\upsilon_l \sim \mathcal{N}(0,1)$ and DS $= 1\mu$s is the channel delay spread. To estimate the channel coefficients at the data subcarriers from those at the pilot subcarriers, we consider cubic splines for the channel interpolation [143]. Indeed, in our simulations, the channel delay taps do not necessarily coincide with the sampling period, i.e., $\tau_l d_\mathrm{F} \neq \frac{l}{F}$ in eq. (4.7). In this situation, the spline-based interpolation provides a more accurate reconstruction of the frequency-domain channel compared to the traditional DFT-based interpolation.

In the following experiments, we compare the performance of the proposed receivers, namely, the BALS and ZFSKP, as well as the LSKRF and ZFSKP, with those of two different competitors: 1) the PN compensation scheme based on [129] and 2) the Baseline LS estimator.

The competing receivers start from the LS estimate provided by (4.21), i.e., $\boldsymbol{Z} \approx [\mathcal{H}]^{(\mathrm{P})}_{(3)} \diamond \Phi \in \mathbb{C}^{KF_{\mathrm{P}} \times M_R M_T}$. The PN compensation scheme of [129] considers $\boldsymbol{Z}$ as the effective pilot channel. An estimate of the effective data channel $\hat{\mathcal{Z}}^{(\mathrm{D})} \in \mathbb{C}^{M_R \times M_T \times F_{\mathrm{D}}}$ is then obtained from the time-domain by averaging over the K blocks followed by interpolation. We use the following subcarrier-wise ZF for data estimation:

$$\hat{\mathcal{S}}^{(\mathrm{D})}_{..f_{\mathrm{D}}} = \left(\boldsymbol{W}\hat{\mathcal{Z}}^{(\mathrm{D})}_{..f_{\mathrm{D}}}\right)^{+} \bar{\mathcal{Y}}^{(\mathrm{D})}_{..f_D}, . \tag{4.36}$$

where $\bar{\mathcal{Y}}^{(\mathrm{D})}_{..f_D} = \frac{1}{K}\sum_{k=1}^{K} \mathcal{Y}^{(\mathrm{D})}_{..kf_D} \in \mathbb{C}^{M_R \times L_P}$. For the baseline LS estimator, we consider the solution of problem (4.21) in two different manners. To obtain an estimate of the pilot channel matrix $[\mathcal{H}]^{(\mathrm{P})}_{(3)}$, we assume a perfect knowledge of the PN matrix Φ and we perform the Khatri-Rao factorization algorithm with one known factor, as discussed in [40], then the spline interpolation is applied to obtain an estimate of the data channel matrix $[\mathcal{H}]^{(\mathrm{D})}_{(3)}$. Likewise, to have an estimation of the phase-noise matrix Φ, the Baseline LS estimator assumes the knowledge of the pilot channel matrix $[\mathcal{H}]^{(\mathrm{P})}_{(3)}$ and perform the Khatri-Rao factorization algorithm with one known factor. Thus, the Baseline LS estimator is a benchmark receiver in the NMSE experiments. With these two benchmark estimations, the Baseline LS estimator applies the following ZF filtering to estimate the data symbols:

$$\hat{\mathcal{S}}^{(\mathrm{D})}_{..f_D} = \left(\boldsymbol{W}(\bar{\hat{\Phi}} \odot \hat{\mathcal{H}}^{(\mathrm{D})}_{..f_D})\right)^{+} \bar{\mathcal{Y}}^{(\mathrm{D})}_{..f_D}, \tag{4.37}$$

where $\bar{\hat{\Phi}} = \frac{1}{K}\sum_{k=1}^{K} \mathrm{unvec}(\hat{\Phi}_{k.}) \in \mathbb{C}^{M_R \times M_T}$ is phase-noise matrix estimated by averaging it over the K blocks, $\hat{\mathcal{H}}^{(\mathrm{D})}_{..f_D} \in \mathbb{C}^{M_R \times M_T}$ is the estimated data channel at the f_D data subcarrier, and $\odot$ stands for the Hadamard product.

4.4.1 ICI power

Fig. 4.3 depicts the values of the ICI power for different number of subcarriers with different values of the transmitter and receiver phase-noise variance (B.4). This result is based on the development detailed in Appendix B, where the ICI power mainly depends on the number of subcarriers and the PN variance. In this chapter, we evaluate the proposed BALS and LSKRF receivers considering two cases: 1) $F = 64$ subcarriers with the transmitter and receiver phase-noise variance $\sigma^2_{\phi^{[\mathrm{t}]}} = \sigma^2_{\phi^{[\mathrm{r}]}} = 5 \cdot 10^{-3}$, leading to a ICI power $\sigma^2_{\mathrm{ICI}} \approx 0.04$ dB, and 2) $F = 128$ subcarriers with the transmitter and receiver phase-noise variance $\sigma^2_{\phi^{[\mathrm{t}]}} = \sigma^2_{\phi^{[\mathrm{r}]}} = 10^{-3}$, resulting $\sigma^2_{\mathrm{ICI}} \approx 0.02$ dB.

Figure 4.3 – ICI power *vs* the number of subcarriers for different values of phase-noise power.

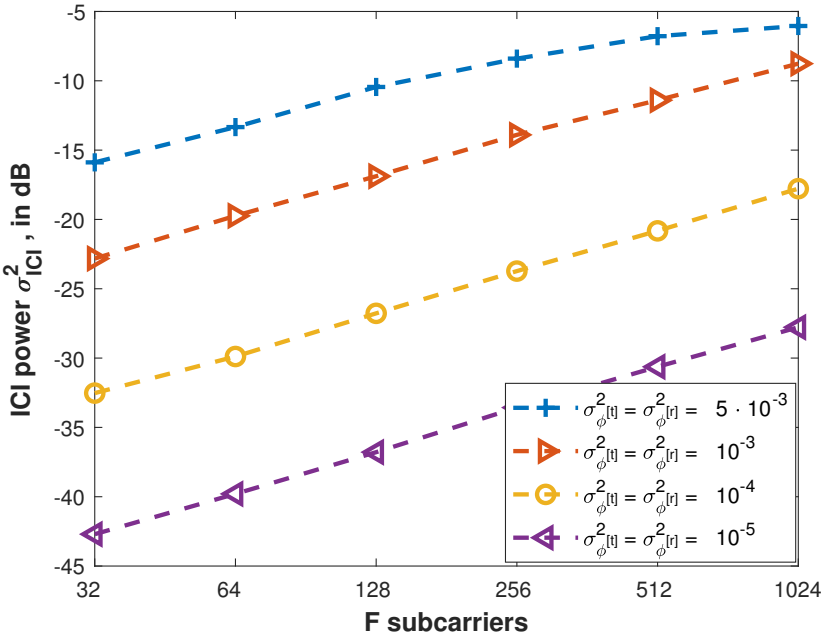

Source: Created by the author.

4.4.2 Data Detection

In this section, we evaluate the performance of the proposed receiver in two parameter configurations, each of comparing four different cases. In Fig. 4.4 we have the configuration of $M_T = L_P = 2$, and $M_R = K = 4$, where we consider the number of subcarriers $F = 64$ and $F = 128$ and the cases with and without the ICI. In Fig. 4.4 (a), we evaluate the performance assuming $F = 64$ and $F_P = 16$ pilots subcarriers with the presence of a high phase-noise variance $\sigma^2_{\phi^{[x]}} = 5 \cdot 10^{-3}$ at the transmitter and the receiver which induces a significant ICI perturbation ($\sigma^2_{ICI} \approx 0.04$ dB), explaining the saturation of the curves at higher SNR values. Note that, our proposed receivers achieve a target SER of 10^{-3} at a SNR of 20 dB, while the Baseline LS receiver only achieves this target SER at an SNR close to 30 dB. Therefore, a significant SNR gain can be obtained by exploiting the tensor structure of the data model. More specifically, this remarkable gain comes from two factors: 1) the decoupling of the channel matrix from the phase-noise matrix, which allows us to successfully refine these estimates via BALS and LSKRF, improving the data estimation performance; 2) the all-at-once estimation of the data symbols using the ZFSKP filter that exploits the tensor structure of the received signal through the combination of all the subcarriers. In Fig. 4.4 (b) we have the case of $F = 128$, $F_P = 32$ pilot subcarriers which we consider the phase-noise variance of $\sigma^2_{\phi^{[x]}} = 10^{-3}$ at the transmitter and the receiver resulting in a ICI power $\sigma^2_{ICI} \approx 0.02$ dB. As expected, with a lower ICI, a better performance is achieved by the proposed BALS ZFSKP and LSKRF ZFSKP receivers. We can observe that, at a SNR of 30 dB, the proposed receivers achieves a target SER of 10^{-4}, while the competitors receivers, due to the the high ICI power, are unable to achieve this gain. In Figs. 4.4

Figure 4.4 – Illustration of the SER assuming $M_R = K = 4$, and $M_T = L_P = 2$ in four cases (a) $F = 64$, $F_P = 16$, (b) $F = 128$, $F_P = 32$ (c) $F = 64$, $F_P = 16$ assuming no ICI, (d) $F = 128$, $F_P = 32$ assuming no ICI.

(a) $\sigma^2_{\phi^{[t]}} = \sigma^2_{\phi^{[r]}} = 5 \cdot 10^{-3}$, $\sigma^2_{\text{ICI}} \approx 0.04$ dB. (b) $\sigma^2_{\phi^{[t]}} = \sigma^2_{\phi^{[r]}} = 10^{-3}$, $\sigma^2_{\text{ICI}} \approx 0.02$ dB.

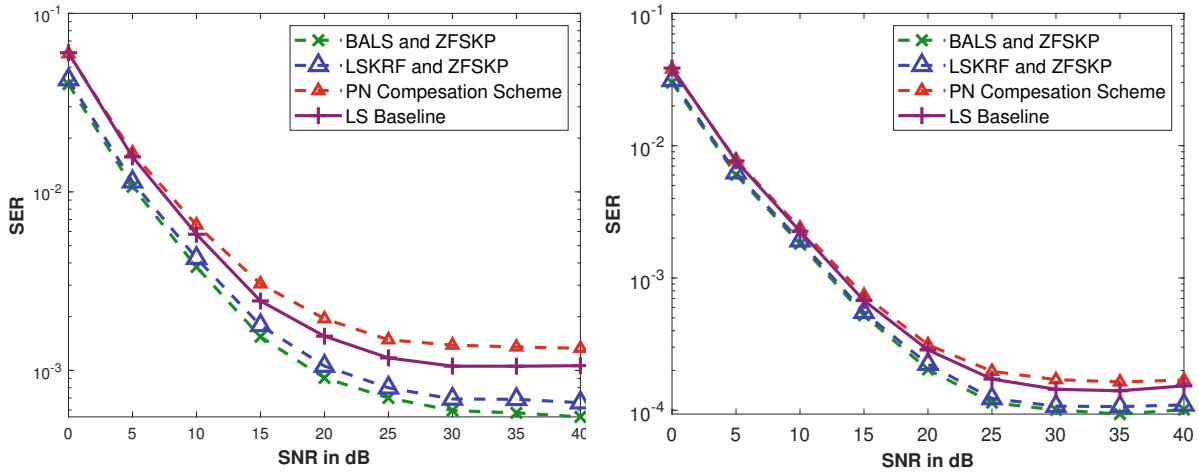

(c) $\sigma^2_{\phi^{[t]}} = \sigma^2_{\phi^{[r]}} = 5 \cdot 10^{-3}$, $\sigma^2_{\text{ICI}} = 0$. (d) $\sigma^2_{\phi^{[t]}} = \sigma^2_{\phi^{[r]}} = 10^{-3}$, $\sigma^2_{\text{ICI}} = 0$.

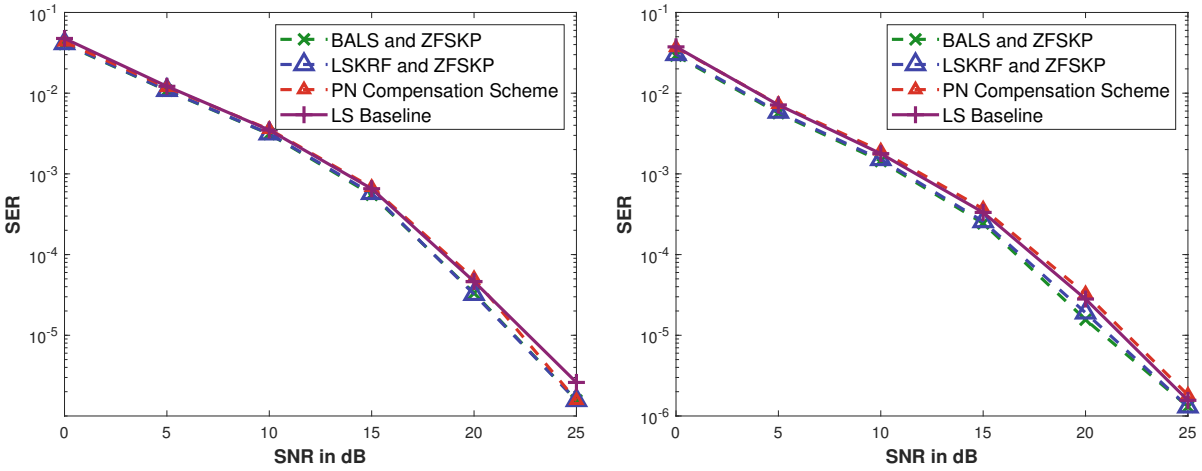

Source: Created by the author.

(c) and (d), we consider an ideal scenario where the ICI is perfectly suppressed, i.e., $\sigma^2_{\text{ICI}} = 0$. In this case, we can observe that all the receivers has approximately the same performance, showing that, the proposed receivers achieve a satisfactory SER performance compared to the competitors in the practical and challenging scenarios where the ICI is present.

In scenario of Fig. 4.5, we assume the parameter configuration of $M_T = L_P = 2$, and $M_R = 4$ $K = 8$. Similar to the results of Figs. 4.4 (a) and (b), we have that the proposed receivers, BALS ZFSKP and LSKRF ZFSKP, outperform the competitors in the cases of $F = 64$ and $F = 128$ subcarriers, respectively. This results follows the explanation of the ones if Figs. 4.4 (a) and (b), but with the difference that, by increasing the number of blocks to $K = 8$ the performances of the all receivers are enhanced, since, as expected, we have a higher number of transmitted pilots. In Fig. 4.5 (c) and (d), the ideal scenario where the ICI is suppressed is depicted, for $F = 64$ and $F = 128$ subcarriers, respectively. In this case, due to the fact of an

Figure 4.5 – Illustration of the SER assuming $M_R = 4$, $K = 8$, and $M_T = L_P = 2$ in four cases (a) $F = 64$, $F_{\mathrm{P}} = 16$, (b) $F = 128$, $F_{\mathrm{P}} = 32$ (c) $F = 64$, $F_{\mathrm{P}} = 16$ assuming no ICI, (d) $F = 128$, $F_{\mathrm{P}} = 32$ assuming no ICI.

(a) $\sigma^2_{\phi^{[\mathrm{t}]}} = \sigma^2_{\phi^{[\mathrm{r}]}} = 5 \cdot 10^{-3}$, $\sigma^2_{\mathrm{ICI}} \approx 0.04$ dB. (b) $\sigma^2_{\phi^{[\mathrm{t}]}} = \sigma^2_{\phi^{[\mathrm{r}]}} = 10^{-3}$, $\sigma^2_{\mathrm{ICI}} \approx 0.02$ dB.

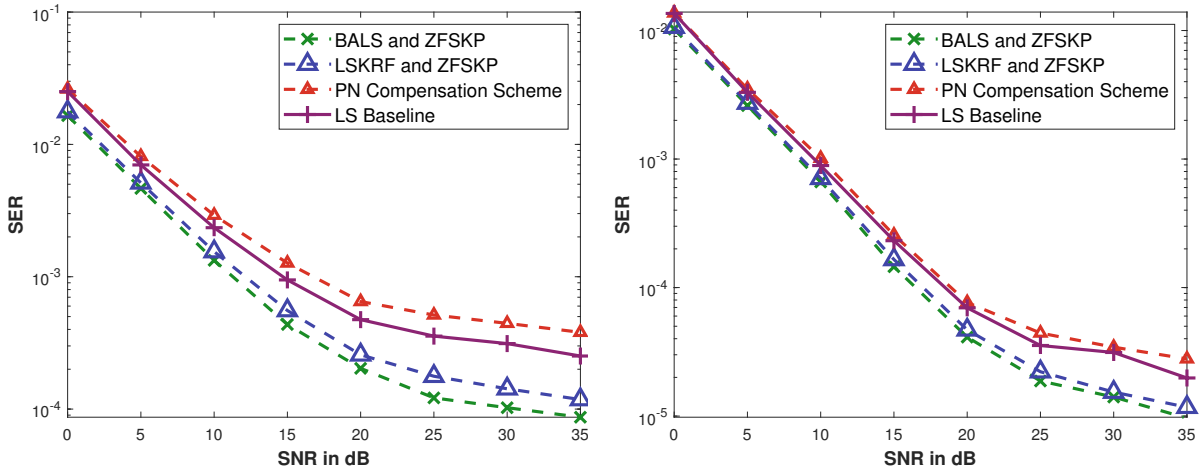

(c) $\sigma^2_{\phi^{[\mathrm{t}]}} = \sigma^2_{\phi^{[\mathrm{r}]}} = 5 \cdot 10^{-3}$, $\sigma^2_{\mathrm{ICI}} = 0$ dB. (d) $\sigma^2_{\phi^{[\mathrm{t}]}} = \sigma^2_{\phi^{[\mathrm{r}]}} = 10^{-3}$, $\sigma^2_{\mathrm{ICI}} = 0$ dB.

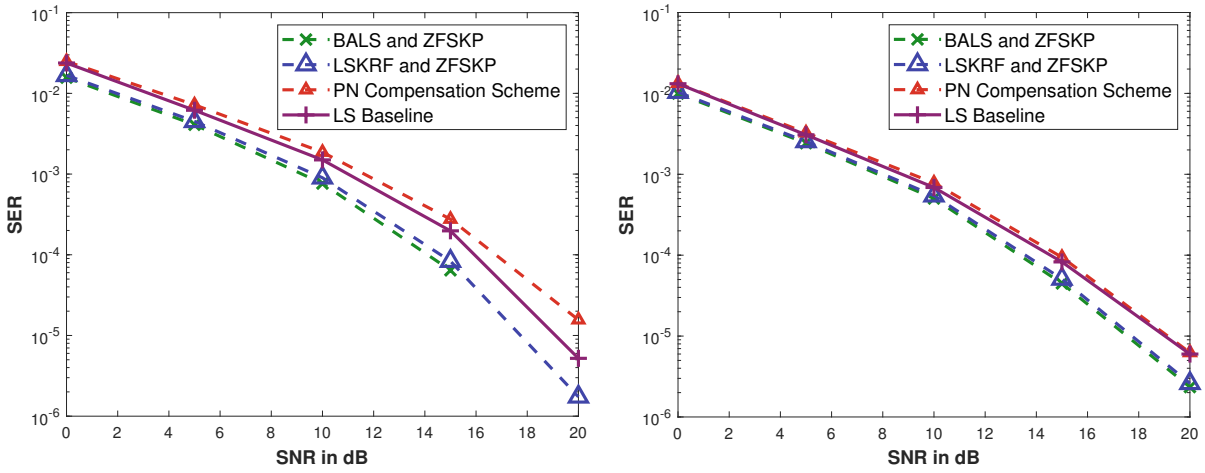

Source: Created by the author.

increased number of frames $K = 8$, the proposed BALS ZFSKP and LSKRF ZFSKP receivers outperforms the competitors. This result shows the that proposed receivers effectively exploit the tensor structure of the received signal, while the Baseline LS solution and the PN compensation scheme [129] perform the phase-noise compensation on a per subcarrier basis, thus ignoring the multidimensional structure of the problem.

Summarizing the results on Figs. 4.4 and 4.5, we have that the tensor-based receivers efficiently exploit the multidimensional structure of the received tensor signal by separating the contributions of the pilot channel matrix from the phase-noise matrix, where their estimates are refined using the BALS and LSKRF algorithms. Also, it is worth to mention that, in tensor-based algorithms, such as the BALS and LSKRF, a scaling factor is always present on the estimated algorithms. However these scaling factors cancel each other in the data estimation (4.31), thus not affecting the data detection.

Figure 4.6 – Illustration of the NMSE of the PN matrix assuming $M_R = 4$, $K = 4$, and $M_T = L_P = 2$ in four cases (a) $F = 64$, $F_P = 16$, (b) $F = 128$, $F_P = 32$.
(a) $\sigma^2_{\phi^{[t]}} = \sigma^2_{\phi^{[r]}} = 5 \cdot 10^{-3}$, $\sigma^2_{\text{ICI}} \approx 0.04$ dB. (b) $\sigma^2_{\phi^{[t]}} = \sigma^2_{\phi^{[r]}} = 10^{-3}$, $\sigma^2_{\text{ICI}} \approx 0.02$ dB.

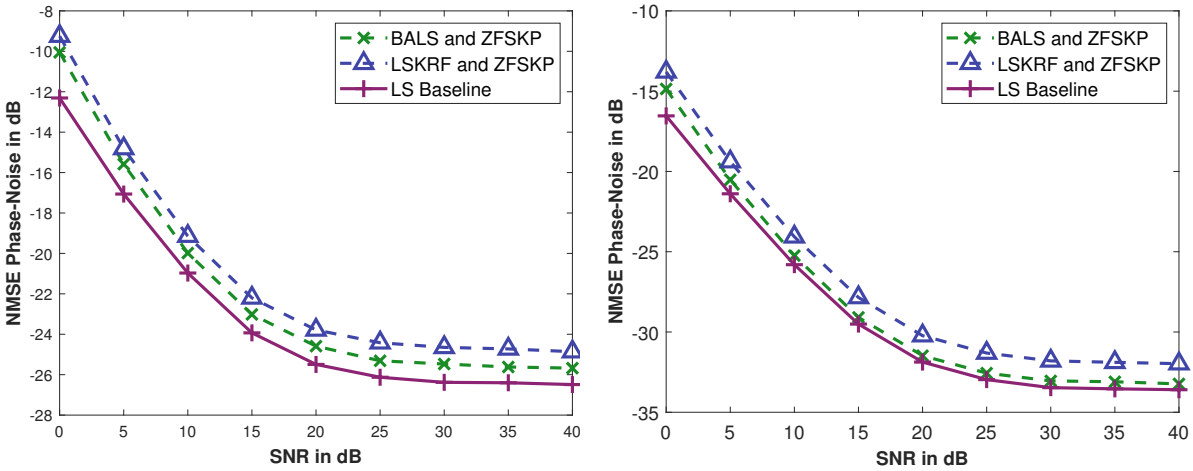

Source: Created by the author.

Figure 4.7 – Illustration of the NMSE of the PN matrix assuming $M_R = 4$, $K = 8$, and $M_T = L_P = 2$ in four cases (a) $F = 64$, $F_P = 16$, (b) $F = 128$, $F_P = 32$.
(a) $\sigma^2_{\phi^{[t]}} = \sigma^2_{\phi^{[r]}} = 5 \cdot 10^{-3}$, $\sigma^2_{\text{ICI}} \approx 0.04$ dB. (b) $\sigma^2_{\phi^{[t]}} = \sigma^2_{\phi^{[r]}} = 10^{-3}$, $\sigma^2_{\text{ICI}} \approx 0.02$ dB.

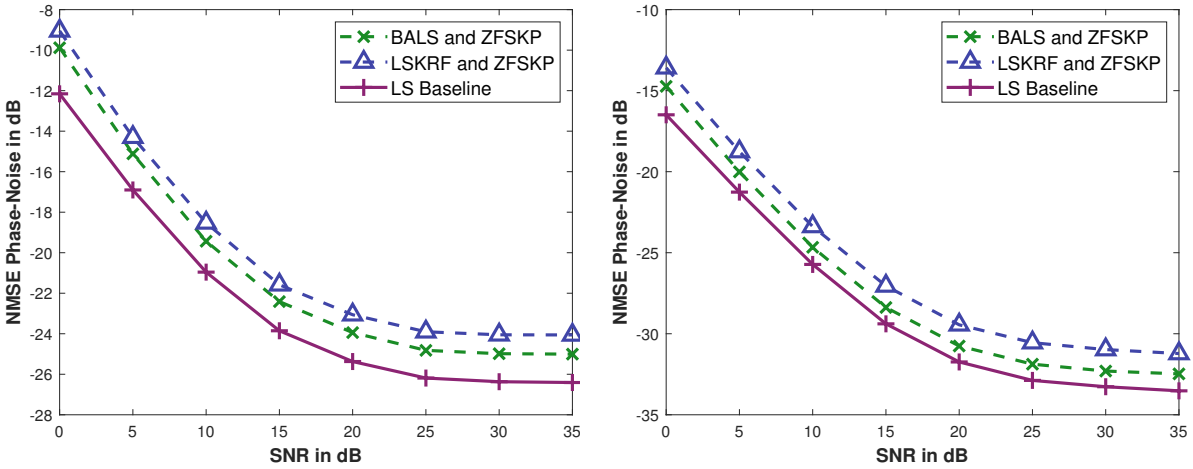

Source: Created by the author.

4.4.3 Phase-Noise NMSE

In Figs. 4.6 and 4.7 we compare the NMSE of the estimated phase-noise matrix $\Phi \in \mathbb{C}^{K \times M_R M_T}$. In all scenarios we have that the LS Baseline competitor outperforms the proposed receivers BALS ZFSKP and LSKRF ZFSKP. This can be explained by the fact that the LS Baseline competitor receiver considers the knowledge of the pilot channel matrix $[\mathcal{H}]^{(\text{P})}_{(3)}$ to perform the Khatri-Rao factorization with one factor known in (4.21) [40]. On the other hand, the proposed receivers only consider the knowledge one row of the phase-noise matrix Φ, in order to remove the scaling effects discussed in Section 4.3.3. It is worth to mention that, the knowledge of one row of the phase-noise matrix Φ is only considered in the NMSE experiments,

Figure 4.8 – Illustration of the NMSE of the data channel matrix assuming $M_R = 4$, $K = 4$, and $M_T = L_P = 2$ in four cases (a) $F = 64$, $F_{\mathrm{P}} = 16$, (b) $F = 128$, $F_{\mathrm{P}} = 32$.
(a) $\sigma^2_{\phi^{[\mathrm{t}]}} = \sigma^2_{\phi^{[\mathrm{r}]}} = 5 \cdot 10^{-3}$, $\sigma^2_{\mathrm{ICI}} \approx 0.04$ dB. (b) $\sigma^2_{\phi^{[\mathrm{t}]}} = \sigma^2_{\phi^{[\mathrm{r}]}} = 10^{-3}$, $\sigma^2_{\mathrm{ICI}} \approx 0.02$ dB.

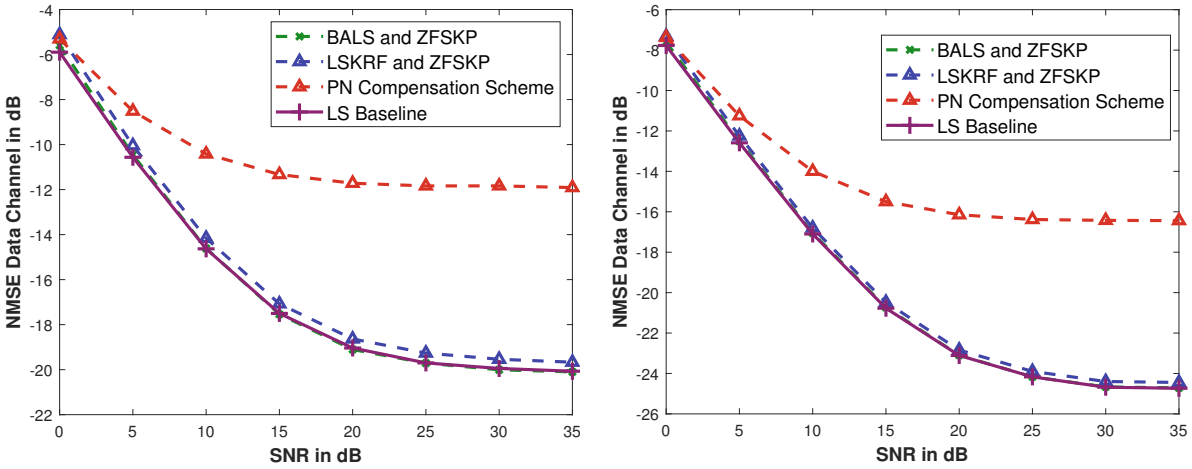

Source: Created by the author.

Figure 4.9 – Illustration of the NMSE of the data channel matrix assuming $M_R = 4$, $K = 8$, and $M_T = L_P = 2$ in four cases (a) $F = 64$, $F_{\mathrm{P}} = 16$, (b) $F = 128$, $F_{\mathrm{P}} = 32$.
(a) $\sigma^2_{\phi^{[\mathrm{t}]}} = \sigma^2_{\phi^{[\mathrm{r}]}} = 5 \cdot 10^{-3}$, $\sigma^2_{\mathrm{ICI}} \approx 0.04$ dB. (b) $\sigma^2_{\phi^{[\mathrm{t}]}} = \sigma^2_{\phi^{[\mathrm{r}]}} = 10^{-3}$, $\sigma^2_{\mathrm{ICI}} \approx 0.02$ dB.

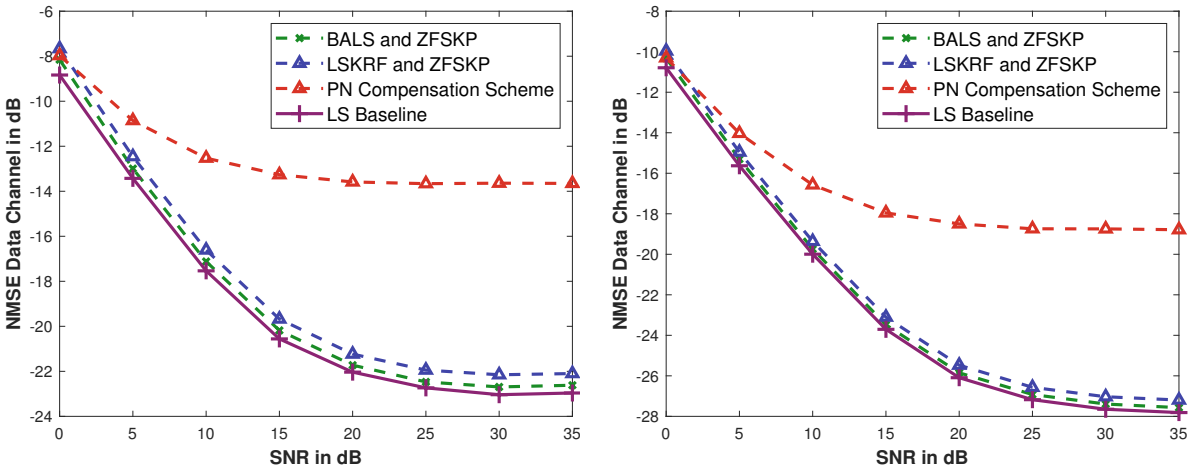

Source: Created by the author.

not being necessary in the data estimation stage.

4.4.4 Data Channel NMSE

In Figs. 4.8 and 4.9 we compare the NMSE of the estimated data matrix $[\boldsymbol{H}]^{(\mathrm{D})}_{(3)} \in \mathbb{C}^{F_{\mathrm{D}} \times M_R M_T}$. Similar to the discussions Figs. 4.6 and 4.7, we have that the proposed receivers BALS ZFSKP and LSKRF ZFSKP have a close performance to the LS Baseline competitor and outperforms the PN compensation scheme of [129]. This can be explained by the fact that, the PN compensation scheme of [129] does not considers the separation of the pilot channel matrix and the phase-noise matrix, thus the data channel is estimated via the interpolation of

Figure 4.10 – Computational complexity of the BALS, LS-KRF, and Baseline LS algorithms for different scenarios.

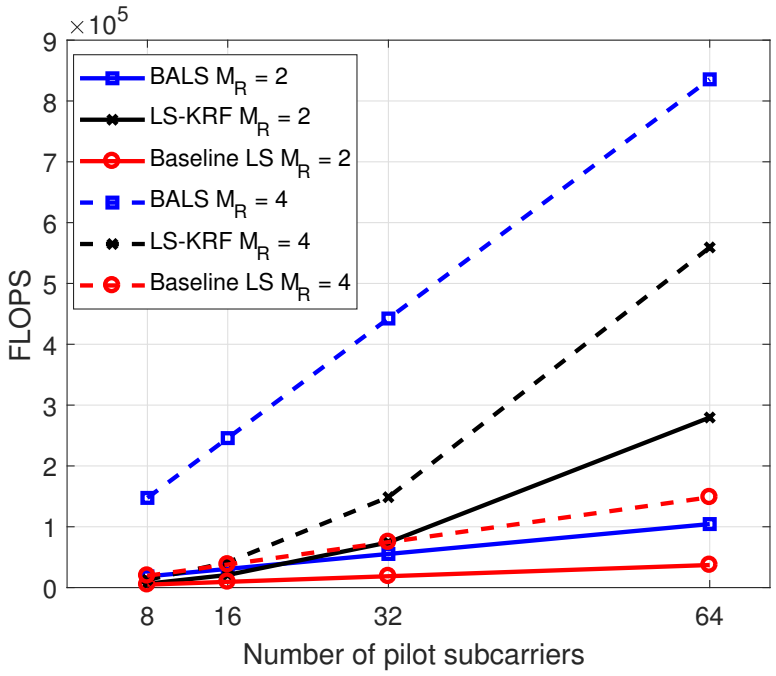

Source: Created by the author.

the LS estimation of $\boldsymbol{Z}$ in (4.21), while the proposed receivers exploits the separability of the pilot channel matrix $[\boldsymbol{H}]^{(\mathrm{P})}_{(3)} \in \mathbb{C}^{F_\mathrm{P} \times M_R M_T}$ and the phase-noise matrix $\Phi \in \mathbb{C}^{K \times M_R M_T}$ to refine its estimations. On the other hand, to have an estimate of the data channel $[\boldsymbol{H}]^{(\mathrm{D})}_{(3)}$, the LS Baseline competitor considers the knowledge of the phase-noise matrix Φ to perform the Khatri-Rao factorization with one factor known in (4.21) [40] to estimate the pilot channel. Then, the data channel is obtained by interpolation. In this experiment, the proposed receiver considers the knowledge of one row of the PN matrix Φ to remove the scaling factor intrinsic to the tensor-based algorithms.

4.4.5 Computational Complexity

Fig. 4.10 compares the computational complexity between the BALS and LSKRF algorithms for different numbers of pilot subcarriers. It is important to mention that, for the BALS algorithm in Algorithm 6, $I = 6$ iterations are needed to achieve the convergence for higher SNR values (> 10 dB). Note that the pseudo-inverse cost in step 1 in Algorithm 7 is not taken into account since the factors $\boldsymbol{S}^{(\mathrm{P})\mathrm{T}}$ and $\boldsymbol{W}$ are known, which means that it can be computed off-line. A trade-off between BALS and LSKRF exists. The first is more attractive for a small number of receiving antennas (e.g., downlink), while the second is preferable when assuming a larger number of receiving antennas (e.g., uplink). Regarding the Baseline LS estimator, we can observe that it is a cheaper algorithm compared to the BALS and the LSKRF algorithms. However, as shown in Figs. 4.4 and 4.5, our proposed receivers achieves a better SER performance. Also, the Baseline LS estimator can be considered as a benchmark receiver since the pilot channel and

phase-noise matrices are assumed to be known.

4.5 Summary

In this chapter, we have proposed a two-stage tensor-based receiver for joint channel, PN, and data estimation in MIMO-OFDM systems. For the first stage, we have derived two algorithms for channel and phase-noise estimation. The first one consists of an iterative solution based on the BALS, while the second algorithm has a closed-form solution based on the LLSKRF. Our numerical simulations show that both algorithms achieve a similar performance, but LSKRF becomes preferable as compared to the BALS when the number of receiving antennas is increased due to its lower computational complexity. We also have proposed a ZFSKP equalizer that exploits the tensor structure of the received signal via the selective Kronecker product (SKP) operator, allowing us to estimate the data on all subcarriers at once. In terms of performance, we have shown that our proposed receiver outperforms its competitors in challenging scenarios with a high phase-noise variance inducing a significant ICI power. As one perspective, the investigation of different strategies for the pilot symbol allocation with the objective of enhancing the symbol detection.

5 TENSOR-BASED METHOD FOR REDUCING THE CONTROL SIGNALING IN IRS-ASSISTED MIMO SYSTEMS

5.1 Introduction

As presented in Chapter 3, the IRS is a candidate technology for beyond fifth generation and sixth generation networks due to its ability to control the electromagnetic properties of the radio-frequency waves by performing an intelligent phase-shift to the desired direction [50, 51, 52, 62, 63, 144, 145, 146], and are defined as a planar (2-D) surface with a large number of independent reflective elements, in which they can be fully passive or with some active elements [65, 66, 147]. The IRS elements are connected to a smart controller that sets the desired phase-shift for each reflective element, by applying bias voltages at the elements e.g., PIN diodes. The main advantage of fully passive IRSs is its full-duplex nature, i.e., no noise amplification is observed since no signal processing is possible. However, the fully passive nature of the IRSs makes the CSI acquisition process difficult, since no pilots are processed, thus only the cascade channel can be estimated. Nevertheless, in the case of employing a few active elements in the IRS, this issue is suppressed and channel can be estimated using, for example, CS tools [147]. Another advantage of an IRS with fully passive elements is that the power consumption is concentrated at the controller. This makes the IRS a more attractive technology in terms of energy efficiency compared to alternative technologies, e.g., amplify-and-forward and decode-and-forward relays [54, 148, 149].

Several works in the literature have addressed the CSI acquisition problem in IRS-assisted networks, as discussed in Section 3.4. However, since they consider passive IRSs, the active (precoder and combiner) and the passive beamformers (IRS phase-shifts) are computed at different system node, which means that they need to be fed back to the IRS controller and the TX, and since the IRS may contain several hundreds to thousand of elements, this feedback causes a control signaling overhead. On this issue, as discussed in 3.6, two works in the literature focused on two different strategies have addressed the control signaling overhead. The work of [117] proposed a grouping strategy to reduce the CSI feedback, while in [116] a resource allocation framework was proposed to mitigate the IRS phase-shift feedback overhead.

In this chapter, we propose a overhead-aware model for designing the IRS phase-shifts. Our idea is to represent the IRS phase-shift vector with a low-rank model. This is achieved by factorizing a *tensorized* version of the IRS phase-shift vector, where each component is modelled as the Kronecker product of a predefined number of factors. These factors are estimated using tensor decompositions such as the PARAFAC [25] and Tucker [26]. After the estimation process, the phases of the factors are quantized and fed back to the IRS controller, which can reconstruct the IRS phase-shift vector based on the chosen low-rank tensor model. The main contributions of this work are the following:

1) Our proposed IRS phase-shift factorization allows to save network resources by

reducing the total IRS phase-shift feedback overhead. This allows a more frequent IRS phase-shift feedback, for a fixed feedback load, which can significantly improve the end-to-end latency, crucial in a fast varying channels, high mobility scenarios and/or the cases with moderate/large sizes of the IRS. Also, thanks to the significant reduction on the feedback overhead, the IRS-assisted network can decide to multiplex phase-shifts associated with a higher number of users in the same feedback channel.

2) The proposed IRS phase-shift factorization provides a flexible feedback design by controlling the parameters of the low-rank factorization model, such as the number of components, the number and the size of the factors, as well as their respective resolution. This is an important feature of our proposed feedback-aware model, since for limited feedback control links, the low-rank model and its factorization parameters can be efficiently adjusted to the available capacity of the feedback link, providing more degrees of freedom to system design.

3) The proposed tensor-based factorization approach relies on the optimum IRS phase-shift vector, which means that it can be implemented in every IRS-assisted network and in multiple communication links, i.e., downlink or uplink, in single-input single-output, multiple-input single-output, as well in MIMO systems.

5.1.1 Related works

Different from the works of [117] and [116], we aim to reduce the IRS phase-shifts feedback overhead by conveying to the IRS controller only the factors of our proposed low-rank model. Our approach is analytical and provides a systematic way of controlling the feedback overhead by adjusting the parameters of the low-rank IRS model, namely, its rank and the corresponding number of factors of each rank-one component. Our simulations show that the proposed low-rank model for the IRS phase-shifts can achieve the same SE as the state-of-the-art [116] in LOS scenarios, while the feedback payload (number of bits to be fed back) is dramatically reduced. For example, taking an IRS with $N = 1024$ elements, the feedback duration can be 50 times smaller than the state-of-the-art [116], depending on the low-rank model parameters. Also, when taking into account the total system SE and EE, i.e., both the IRS phase-shift feedback duration, and the channel estimation duration, our proposed model outperforms the state-of-the-art.

5.2 System Model

We consider the system illustrated in Fig. 5.1, where the TX is equipped with a uniform linear array (ULA) with M_T antenna elements, the RX is equipped with ULA with M_R antenna elements and the IRS has N reflective elements. To simplify the discussion, let us consider a single stream transmission, and assume that there is no direct link between the TX and RX, e.g., BS. First, the TX sends a pilot signal to the RX with the aid of the IRS. Since the IRS has no signal processing capabilities, the channel estimation and the IRS phase-shifts

Figure 5.1 – System model illustration.

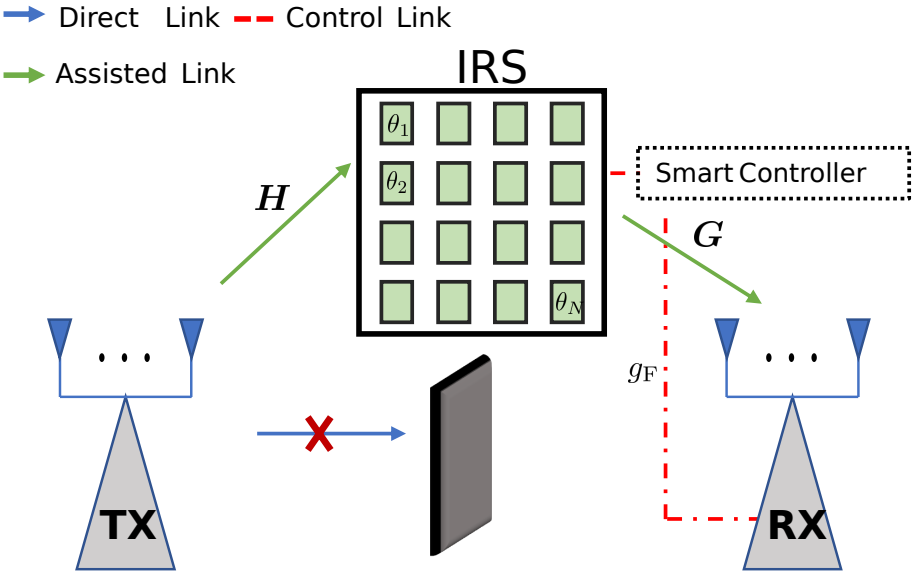

Source: Created by the author.

optimization are performed at the RX. The received signal after processing the pilots is given by

$$y = \boldsymbol{w}^{\mathrm{H}}\boldsymbol{G}\mathrm{diag}\,(\boldsymbol{s})\,\boldsymbol{H}\boldsymbol{q} + \boldsymbol{w}^{\mathrm{H}}\boldsymbol{b}, \tag{5.1}$$

where $\boldsymbol{b} \in \mathbb{C}^{M_R \times 1}$ is the additive noise at the receiver with $\mathbb{E}[\boldsymbol{b}\boldsymbol{b}^{\mathrm{H}}] = \sigma_b^2 \boldsymbol{I}_{M_r}$, $\boldsymbol{w} \in \mathbb{C}^{M_R \times 1}$ and $\boldsymbol{q} \in \mathbb{C}^{M_T \times 1}$ are the receiver and transmitter combiner and precoder (active beamformers), respectively. $\boldsymbol{H} \in \mathbb{C}^{N \times M_T}$ and $\boldsymbol{G} \in \mathbb{C}^{M_R \times N}$ are the TX-IRS and IRS-RX involved channels, and $\boldsymbol{s} = [e^{j\theta_1}, \ldots, e^{j\theta_N}] \in \mathbb{C}^{N \times 1}$ being the IRS phase-shift vector, and θ_n is the phase-shift applied to the n-th IRS element (passive beamformer). The channels in (5.1) are modelled as

$$\boldsymbol{H} = \sqrt{\alpha_H \frac{K_H}{K_H + 1}}\boldsymbol{H}_{\mathrm{LOS}} + \sqrt{\alpha_H \frac{1}{K_H + 1}}\boldsymbol{H}_{\mathrm{NLOS}}, \tag{5.2}$$

$$\boldsymbol{G} = \sqrt{\alpha_G \frac{K_G}{K_G + 1}}\boldsymbol{G}_{\mathrm{LOS}} + \sqrt{\alpha_G \frac{1}{K_G + 1}}\boldsymbol{G}_{\mathrm{NLOS}}, \tag{5.3}$$

where α_H and α_G are the path-loss components of the TX-IRS and IRS-RX links, respectively. The scalars K_H and K_G are the Rician factors associated with the channel matrices $\boldsymbol{H}$ and $\boldsymbol{G}$, respectively. $\boldsymbol{H}_{\mathrm{LOS}}$, $\boldsymbol{G}_{\mathrm{LOS}}$ follow a geometric-based channel model, while the entries of $\boldsymbol{H}_{\mathrm{NLOS}}$, $\boldsymbol{G}_{\mathrm{NLOS}}$ are modeled as circularly symmetric complex Gaussian random variables, with zero mean and unit variance, i.e., $\boldsymbol{H}_{\mathrm{NLOS}} \sim \mathcal{CN}(0, \boldsymbol{I}_{M_T})$ and $\boldsymbol{G}_{\mathrm{NLOS}} \sim \mathcal{CN}(0, \boldsymbol{I}_{M_R})$. The the LOS components are given as

$$\boldsymbol{H}_{\mathrm{LOS}} = \boldsymbol{b}_{\mathrm{IRS}} \cdot \boldsymbol{a}_{\mathrm{TX}}^{\mathrm{H}} \in \mathbb{C}^{N \times M_T}, \tag{5.4}$$

$$\boldsymbol{G}_{\mathrm{LOS}} = \boldsymbol{b}_{\mathrm{RX}} \cdot \boldsymbol{a}_{\mathrm{IRS}}^{\mathrm{H}} \in \mathbb{C}^{M_R \times N}. \tag{5.5}$$

Assuming that the TX and the RX are equipped with ULAs with half-wavelength inter-element spacing, their steering vectors can be written as

$$\boldsymbol{a}_{\mathrm{TX}} = \left[1, e^{j\pi\sin\theta_{\mathrm{TX}}}, \ldots, e^{j\pi(M_T-1)\sin\theta_{\mathrm{TX}}}\right]^{\mathrm{T}} \in \mathbb{C}^{M_T\times 1}, \tag{5.6}$$

$$\boldsymbol{b}_{\mathrm{RX}} = \left[1, e^{j\pi\sin\theta_{\mathrm{RX}}}, \ldots, e^{j\pi(M_R-1)\sin\theta_{\mathrm{RX}}}\right]^{\mathrm{T}} \in \mathbb{C}^{M_R\times 1}, \tag{5.7}$$

where θ_{TX} and θ_{RX} are the TX and RX angle of departure (AOD) and angle of arrival (AOA), respectively, which are generated from a uniform random distribution with $\{\theta_{\mathrm{TX}}, \theta_{\mathrm{RX}}\} \in [-\pi, \pi]$. Since the IRS is a 2-D panel, the steering vectors associated with arrival and departure angles can be factorized as the Kronecker product of horizontal and vertical component vectors, respectively, $\boldsymbol{b}_{\mathrm{IRS}} = \boldsymbol{b}_{\mathrm{IRS}}^{(\upsilon)} \otimes \boldsymbol{b}_{\mathrm{IRS}}^{(h)} \in \mathbb{C}^{N_h N_\upsilon \times 1}$, and $\boldsymbol{a}_{\mathrm{IRS}} = \boldsymbol{a}_{\mathrm{IRS}}^{(\upsilon)} \otimes \boldsymbol{a}_{\mathrm{IRS}}^{(h)} \in \mathbb{C}^{N_h N_\upsilon \times 1}$, where $N = N_h N_\upsilon$, $\boldsymbol{b}_{\mathrm{IRS}}^{(h)} \in \mathbb{C}^{N_h\times 1}$ and $\boldsymbol{b}_{\mathrm{IRS}}^{(\upsilon)} \in \mathbb{C}^{N_\upsilon\times 1}$ are the AOA steering vectors in the azimuth and elevation directions, respectively. Likewise, $\boldsymbol{a}_{\mathrm{IRS}}^{(h)} \in \mathbb{C}^{N_h\times 1}$ and $\boldsymbol{a}_{\mathrm{IRS}}^{(\upsilon)} \in \mathbb{C}^{N_\upsilon\times 1}$ are the AOD steering vectors in the azimuth and elevation directions, respectively. The vertical and horizontal vectors are given as

$$\boldsymbol{b}_{\mathrm{IRS}}^{(h)} = [1, e^{j\pi\sin\psi_{\mathrm{IRS}}^{\mathrm{AOA}}\cos\phi_{\mathrm{IRS}}^{\mathrm{AOA}}}, \ldots, e^{j\pi(N_h-1)\sin\psi_{\mathrm{IRS}}^{\mathrm{AOA}}\cos\phi_{\mathrm{IRS}}^{\mathrm{AOA}}}], \tag{5.8}$$

$$\boldsymbol{b}_{\mathrm{IRS}}^{(\upsilon)} = [1, e^{j\pi\cos\phi_{\mathrm{IRS}}^{\mathrm{AOA}}}, \ldots, e^{j\pi(N_h-1)\cos\phi_{\mathrm{IRS}}^{\mathrm{AOA}}}], \tag{5.9}$$

$$\boldsymbol{a}_{\mathrm{IRS}}^{(h)} = [1, e^{j\pi\sin\psi_{\mathrm{IRS}}^{\mathrm{AOD}}\cos\phi_{\mathrm{IRS}}^{\mathrm{AOD}}}, \ldots, e^{j\pi(N_h-1)\sin\psi_{\mathrm{IRS}}^{\mathrm{AOD}}\cos\phi_{\mathrm{IRS}}^{\mathrm{AOD}}}], \tag{5.10}$$

$$\boldsymbol{a}_{\mathrm{IRS}}^{(\upsilon)} = [1, e^{j\pi\cos\phi_{\mathrm{IRS}}^{\mathrm{AOD}}}, \ldots, e^{j\pi(N_h-1)\cos\phi_{\mathrm{IRS}}^{\mathrm{AOD}}}], \tag{5.11}$$

where $\phi_{\mathrm{IRS}}^{\mathrm{AOA}}$ and $\phi_{\mathrm{IRS}}^{\mathrm{AOD}}$ are the elevation angles of arrival and departure, while $\psi_{\mathrm{IRS}}^{\mathrm{AOA}}$ and $\psi_{\mathrm{IRS}}^{\mathrm{AOD}}$ are the azimuth angles of arrival and departure. The azimuth angles $\psi_{\mathrm{IRS}}^{\mathrm{AOA}}$ and $\psi_{\mathrm{IRS}}^{\mathrm{AOD}}$ are generated from a uniform random distribution with $\{\psi_{\mathrm{IRS}}^{\mathrm{AOA}}, \psi_{\mathrm{IRS}}^{\mathrm{AOD}}\} \in [-\pi, \pi]$, while the elevation angles $\phi_{\mathrm{IRS}}^{\mathrm{AOA}}$ and $\phi_{\mathrm{IRS}}^{\mathrm{AOD}}$ are generated from an uniform random distribution with $\{\phi_{\mathrm{IRS}}^{\mathrm{AOA}}, \phi_{\mathrm{IRS}}^{\mathrm{AOD}}\} \in [0, \pi/2]$.

5.2.1 Channel Estimation and Beamforming Optimization

In this chapter, we focus on the IRS phase-shifts feedback overhead problem, thus the channels $\boldsymbol{G}$ and $\boldsymbol{H}$ are available at the receiver and have been obtained using a prior art method, e.g., [22] discussed in Section 3.4. Also, we assume that the Upper Bound algorithm [116], discussed in Section 3.5.3, is used to obtain the joint optimization of the active and passive beamformers $\boldsymbol{q}$, $\boldsymbol{w}$, and $\boldsymbol{s}$. Different optimization algorithms can be found in, e.g., [50, 114].

5.2.2 Feedback Overhead Model

In this section we provide an elaborate discussion on the proposed IRS phase-shift feedback overhead reduction methods, where we aim to reduce the IRS phase-shift feedback duration given by

$$T_{\mathrm{F}} = \frac{N b_{\mathrm{F}}}{B_{\mathrm{F}} \log\left(1 + \frac{p_{\mathrm{F}}|g_{\mathrm{F}}|^2}{B_{\mathrm{F}} N_0}\right)}. \tag{5.12}$$

As discussed in Section 3.6, the authors in [116] proposed a method for reducing the total IRS feedback overhead by optimizing the network resources, i.e., the feedback bandwidth B_{F}, feedback power p_{F}. The proposed methods focus on the feedback overhead reduction by factorizing the numerator of (5.12). In other words, we proposed two tensor-based models, namely, PARAFAC-IRS and Tucker-IRS, to reduce the feedback overhead by factorizing the IRS phase-shift vector into smaller factors, as explained in the following section.

5.3 Proposed Feedback Overhead Model

In this section, we describe the proposed tensor low-rank approximation based feedback-aware methods that focus on reducing the feedback duration T_{F} given in (5.12). Our initial idea [150] consists of factorizing $\boldsymbol{s}$ (optimized in (3.17)) as the Kronecker product of P factors, i.e.,

$$\boldsymbol{s} \approx \boldsymbol{s}^{(P)} \otimes \ldots \otimes \boldsymbol{s}^{(1)} \in \mathbb{C}^{N_P \cdots N_1 \times 1}, \tag{5.13}$$

where $\boldsymbol{s}^{(p)} \in \mathbb{C}^{N_p \times 1}$ is the p-th factor and $N = \prod_{p=1}^{P} N_p$. The equality in (5.13) only occurs when $(K_H, K_G) \rightarrow \infty$, since, in this case, the channels are composed only by their LOS components. Noting that, the LOS components are separable, according to (5.6)-(5.11), with a Vandermonde structure, and every Vandermonde vector of size N can be factorized as the Kronecker product of P smaller factors [130], such that $N = \prod_{p=1}^{P} N_p$, with N_p being the size of the p-th factor. In order to estimate the factors in (5.13), first we tensorize $\boldsymbol{s}$ as a P-th order tensor $\mathcal{S} \in \mathbb{C}^{N_1 \times \ldots \times N_P}$. In other words, since $\boldsymbol{s}$ is a Kronecker structure vector, we have similar to (2.46), a rank-one tensor

$$\mathcal{S} = \mathcal{T}\{\boldsymbol{s}\} \approx \boldsymbol{s}^{(1)} \circ \ldots \circ \boldsymbol{s}^{(P)}. \tag{5.14}$$

The Algorithm 2 can be used to perform a rank-one approximation to find the P factors $\boldsymbol{s}^{(1)}, \ldots, \boldsymbol{s}^{(P)}$. This means that, instead of feedback to the IRS controller $N = \prod_{p=1}^{P} N_p$ phase-shifts, we only convey the phase-shifts of the individual factors, i.e., $\sum_{p=1}^{P} N_p$.

Example: To get the first insight into the impact of this factorization on the IRS phase-shift feedback overhead, let us consider a simple scenario with $N = 1024$ phase-shifts, and we apply our factorization method by choosing $P = 3$ factors. Consider, as one example, the following factors $\boldsymbol{s}^{(1)} = [e^{j\theta_1^{(1)}}, \ldots, e^{j\theta_{32}^{(1)}}] \in \mathbb{C}^{32\times 1}$, $\boldsymbol{s}^{(2)} = [e^{j\theta_1^{(2)}}, \ldots, e^{j\theta_8^{(2)}}] \in \mathbb{C}^{8\times 1}$ and $\boldsymbol{s}^{(3)} = [e^{j\theta_1^{(3)}}, \ldots, e^{j\theta_4^{(3)}}] \in \mathbb{C}^{4\times 1}$, i.e., $N_1 = 32$, $N_2 = 8$ and $N_3 = 4$. Note that, N_1, N_2, N_3 can have every size as long $N_1 \times N_2 \times N_3 = N = 1024$. In this scenario, instead of conveying to the IRS controller 1024 phase-shifts, we only need to convey the phase-shifts of the factors, i.e., $32 + 8 + 4 = 44$, reducing drastically the total amount of phase-shift overhead. Physically, the Kronecker product in (5.13) represents a summation of the factors phase-shifts. It is clear that, in a general model for a large N, and based on the choice of P, we have that $\sum_{p=1}^{P} N_P << N = \prod_{p=1}^{P} N_P$. The discussed example is illustrated in Fig. 5.2. ■

Figure 5.2 – (a) IRS with $N = 1024$ elements without factorization, (b) IRS with $N = 1024$ elements factorized into $P = 3$ factors.

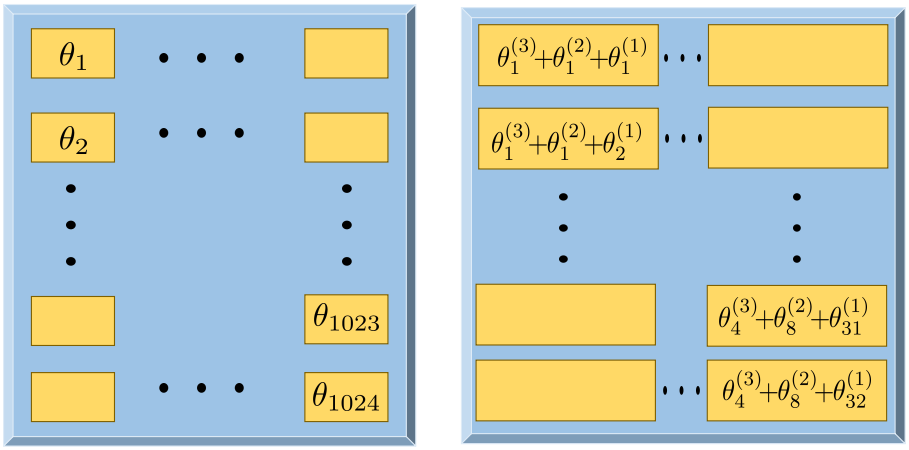

(a) (b)

Source: Created by the author.

In the following, we generalize the model (5.13) by factorizing the IRS phase-shift vector $\boldsymbol{s} \in \mathbb{C}^{N\times 1}$ based on the PARAFAC and Tucker LRA models.

5.3.1 PARAFAC-IRS Low-Rank Approximation

In (5.14), the IRS phase-shift vector is approximated by a rank-one tensor. In this section, we generalize this model to a rank-R tensor approximation. More specifically, the optimum phase-shift vector $\boldsymbol{s}$ is factorized according to a PARAFAC model, i.e.,

$$\boldsymbol{s} \approx \sum_{r=1}^{R} \boldsymbol{s}_r^{(P)} \otimes \ldots \otimes \boldsymbol{s}_r^{(1)} \in \mathbb{C}^{N_1 \cdots N_P \times 1}, \tag{5.15}$$

which, using (2.46) and (2.47), implies that

$$\mathcal{S} \approx \sum_{r=1}^{R} \boldsymbol{s}_r^{(1)} \circ \ldots \circ \boldsymbol{s}_r^{(P)} \in \mathbb{C}^{N_1 \times \cdots \times N_P}, \tag{5.16}$$

where $\mathcal{S} = \mathcal{T}\{\boldsymbol{s}\}$, R is the number of components (or tensor rank) and $\boldsymbol{s}_r^{(p)} \in \mathbb{C}^{N_p \times r}$ is the r-th column of the p-th factor matrix $\boldsymbol{S}^{(p)} = [\boldsymbol{s}_1^{(1)}, \ldots, \boldsymbol{s}_R^{(p)}] \in \mathbb{C}^{N_p \times R}$, for $p = \{1, \ldots, P\}$.

The main idea of adding components is to mitigate the approximation error when having strong non-line-of-sight (NLOS) components in the channels. Ideally, when considering continuous phase-shifts, the approximation error will decrease as the number of components R increase. However, in practice, we have to quantize the phase-shift and the weights of each component, inducing a quantization error. Also, increasing R implies a higher feedback overhead payload, since more components are required to be conveyed. A detailed discussion on the choice and the physical impact of the number of components R, the number of factors P, and the size of each factor N_p for $p = \{1, \ldots, P\}$ is given in Section 5.4 and 5.5.

Algorithm 9 PARAFAC-IRS ALS

1: **Inputs**: Tensor $\mathcal{S} \in \mathbb{C}^{N_1 \times \cdots \times N_P}$, the number of components R, and maximum number of iterations I.
2: Randomly initialize the factors $\hat{\boldsymbol{S}}_0^{(2)}, \ldots, \hat{\boldsymbol{S}}_0^{(P)}$. Iteration $i = 0$.
3: Define a maximum number of iteration I.
4: **for** $i = 1 : I$ **do**
5: **for** $p = 1 : P$ **do**
6: Compute an estimate of the p-th factor $\boldsymbol{S}_{\mathrm{i}}^{(p)}$ as

$$\hat{\boldsymbol{S}}_i^{(p)} = [\mathcal{S}]_{(p)} \left(\left(\hat{\boldsymbol{S}}_{i-1}^{(P)} \diamond \ldots \diamond \hat{\boldsymbol{S}}_{i-1}^{(p+1)} \diamond \hat{\boldsymbol{S}}_{i-1}^{(p-1)} \diamond \ldots \diamond \hat{\boldsymbol{S}}_{i-1}^{(1)} \right)^{\mathrm{T}} \right)^{+}$$

7: **for** $r = 1 : R$ **do**
8: Normalize the r-th column of $\hat{\boldsymbol{S}}_{(i)}^{(p)}$, defined as $\boldsymbol{s}_{r,(i)}^{(p)}$, and store its norm as the r-th element of the vector $\boldsymbol{\lambda}^{(p)} \in \mathbb{R}^{R \times 1}$

$$\lambda_r^{(p)} = \left\| \hat{\boldsymbol{s}}_{r,(i)}^{(p)} \right\|_2, \qquad \hat{\boldsymbol{s}}_{r,(i)}^{(p)} = \frac{\hat{\boldsymbol{s}}_{r,(i)}^{(p)}}{\lambda_r^{(p)}}.$$

9: **end for**
10: **end for**
11: Define the weighting vector $\boldsymbol{\lambda} = \boldsymbol{\lambda}^{(1)} \odot \cdots \odot \boldsymbol{\lambda}^{(P)} \in \mathbb{C}^{R \times 1}$.
12: **end for**
13: Return $\hat{\boldsymbol{S}}^{(1)}, \ldots, \hat{\boldsymbol{S}}^{(P)}$ and $\boldsymbol{\lambda}$.

The RX estimates the factor components solving the following problem

$$\left[\hat{\boldsymbol{s}}_r^{(1)}, \ldots, \hat{\boldsymbol{s}}_r^{(P)} \right]_{\text{for } r=1,\ldots,R} = \underset{\boldsymbol{s}_r^{(1)}, \ldots, \boldsymbol{s}_r^{(P)}}{\operatorname{argmin}} \left\| \mathcal{S} - \sum_{r=1}^{R} \boldsymbol{s}_r^{(1)} \circ \ldots \circ \boldsymbol{s}_r^{(P)} \right\|_{\mathrm{F}}^2, \tag{5.17}$$

where $\boldsymbol{s}_r^{(p)} \in \mathbb{C}^{N_p \times 1}$ is the p-th factor component. Let us define $\boldsymbol{S}^{(p)} = \left[\boldsymbol{s}_1^{(p)}, \ldots, \boldsymbol{s}_R^{(p)} \right] \in \mathbb{C}^{N_p \times R}$ as the p-th factor matrix, for $p = \{1, \ldots, P\}$. From (2.50), the p-mode unfolding of $\mathcal{S}$, defined as $[\mathcal{S}]_{(p)} \in \mathbb{C}^{N_p \times N_1 \cdots N_{p-1} N_{p+1} \cdots N_P}$, is given as

$$[\mathcal{S}]_{(p)} \approx \boldsymbol{S}^{(p)} \left(\boldsymbol{S}^{(P)} \diamond \ldots \diamond \boldsymbol{S}^{(p+1)} \diamond \boldsymbol{S}^{(p-1)} \diamond \ldots \diamond \boldsymbol{S}^{(1)} \right)^{\mathrm{T}}. \tag{5.18}$$

To solve the problem in (5.17), the RX can use the ALS algorithm [23], described in Algorithm 9. Different from Algorithm 1, the Algorithm 9 normalize each factor to unit norm and collecting the result as a weighting factor. The ALS algorithm contains I iterations, where, in each iteration, P LS problems are solved. The p-th LS problem is defined as

$$\hat{\boldsymbol{S}}^{(p)} = \underset{\boldsymbol{S}^{(p)}}{\operatorname{argmin}} \left\| [\mathcal{S}]_{(p)} - \boldsymbol{S}^{(p)} \left(\boldsymbol{S}^{(P)} \diamond \ldots \diamond \boldsymbol{S}^{(p+1)} \diamond \boldsymbol{S}^{(p-1)} \diamond \ldots \diamond \boldsymbol{S}^{(1)} \right)^{\mathrm{T}} \right\|_{\mathrm{F}}^2 \tag{5.19}$$

where its solution is given by

$$\hat{\boldsymbol{S}}^{(p)} = [\mathcal{S}]_{(p)} \left(\left(\boldsymbol{S}^{(P)} \diamond \ldots \diamond \boldsymbol{S}^{(p+1)} \diamond \boldsymbol{S}^{(p-1)} \diamond \ldots \diamond \boldsymbol{S}^{(1)} \right)^{\mathrm{T}} \right)^{+}. \tag{5.20}$$

In the first iteration, the first step is to estimate $[\mathcal{S}]_{(1)}$ based on (5.20), for $p = 1$. Then, its R columns are normalized to unit norm and stored in as elements of the vector $\boldsymbol{\lambda}^{(1)} \in \mathbb{R}^{R\times 1}$. After the normalization, the estimated $\left[\hat{\mathcal{S}}\right]_{(1)}$ is plugged in the LS solution (5.20) for $p = 2$. Likewise, the columns of the estimated factor $\left[\hat{\mathcal{S}}\right]_{(2)}$ are normalized and stored in a vector defined $\boldsymbol{\lambda}^{(2)} \in \mathbb{R}^{R\times 1}$, and then, the normalized estimations $\left[\hat{\mathcal{S}}\right]_{(1)}$ and $\left[\hat{\mathcal{S}}\right]_{(2)}$ are plugged into the LS solution (5.20) for $p = 3$. This process continues for the $P-3$ remaining LS problems. Then, we compute the weighting vector $\boldsymbol{\lambda} \in \mathbb{R}^{R\times 1}$ as the Hadamard product of all P factors norms, i.e., $\boldsymbol{\lambda} = \boldsymbol{\lambda}^{(1)} \odot \boldsymbol{\lambda}^{(2)} \odot \cdots \odot \boldsymbol{\lambda}^{(P)}$, finalizing the first iteration of the ALS. Then, the process repeats for all I iterations or until reaching a convergence threshold by checking the NMSE of the reconstructed tensor in a window of consecutive iterations. The NMSE at the i-th iteration is given as

$$\mathrm{e}_{(i)} = \frac{\left\| [\mathcal{S}]_{(1),(i)} - \left[\hat{\mathcal{S}}\right]_{(1),(i)} \right\|_{\mathrm{F}}^2}{\left\| [\mathcal{S}]_{(1),(i)} \right\|_{\mathrm{F}}^2},$$

where $\left[\hat{\mathcal{S}}\right]_{(1),(i)}$ is the reconstructed 1-mode unfolding at the i-th ALS iteration, given by

$$\left[\hat{\mathcal{S}}\right]_{(1),(i)} = \hat{\boldsymbol{S}}^{(1)} \mathrm{diag}\left(\boldsymbol{\lambda}\right) \left(\hat{\boldsymbol{S}}^{(P)} \diamond \ldots \diamond \hat{\boldsymbol{S}}^{(2)}\right)^{\mathrm{T}}. \tag{5.21}$$

If $|\mathrm{e}_{(i)} - \mathrm{e}_{(i-1)}| \leq \epsilon$, where ϵ is a pre-defined threshold, the algorithm stops [23]. In this document, we consider $\epsilon = 10^{-6}$.

After the ALS algorithm, the phase-shifts of each factor and the weighting vector $\boldsymbol{\lambda}$ are quantized to be conveyed to the IRS controller. In this case, the feedback duration is given by

$$T_{\mathrm{F}}^{(\mathrm{PARAFAC})} = \frac{\mathrm{T_{PR}} + R \sum\limits_{p=1}^{P} N_p \cdot b_{\mathrm{F}}^{(p)} + (R-1) \cdot b_{\mathrm{F}}^{(\mathrm{w})}}{B_{\mathrm{F}} \log\left(1 + \frac{p_{\mathrm{F}} |g_{\mathrm{F}}|^2}{B_{\mathrm{F}} N_0}\right)}, \tag{5.22}$$

where $\mathrm{T_{PR}}$ is the number of bits required for a preamble of the frame, in order to inform the IRS controller the factorization parameters, such as P, R and the quantization bits $b_{\mathrm{F}}^{(p)}$, and $b_{\mathrm{F}}^{(\mathrm{w})}$, where the $b_{\mathrm{F}}^{(p)}$ is the number of bits used for quantize the phase-shifts of the p-th factor, while $b_{\mathrm{F}}^{(\mathrm{w})}$ is the number of bits for quantizing the elements of the weighting vector $\boldsymbol{\lambda}$.

As one example, Fig. 5.3 illustrates the ratio between the state-of-the-art [116], where N IRS phase-shifts are fed back, with the proposed PARAFAC-IRS approach where we have $R \sum\limits_{p=1}^{P} N_P$ phase-shifts, i.e., we analyse the ratio $N/(R \sum\limits_{p=1}^{P} N_P)$. To this end, let us define a vector $\boldsymbol{N}_{\mathrm{P}} = [N_1 \ldots N_P] \in \mathbb{R}^{P\times 1}$ that contains the factor's size for a certain P. We can observe that, for $R = 1$, the feedback duration of the proposed approach for the case of $P = 2$, $N_1 = 256$, $N_2 = 4$, is almost five times smaller than the state-of-the-art. In addition, when we increase the number of factors P, the size of the factors can be reduced, thus decreasing the feedback duration. In the

Figure 5.3 – PARAFAC-IRS feedback payload ratio for $N = 1024$.

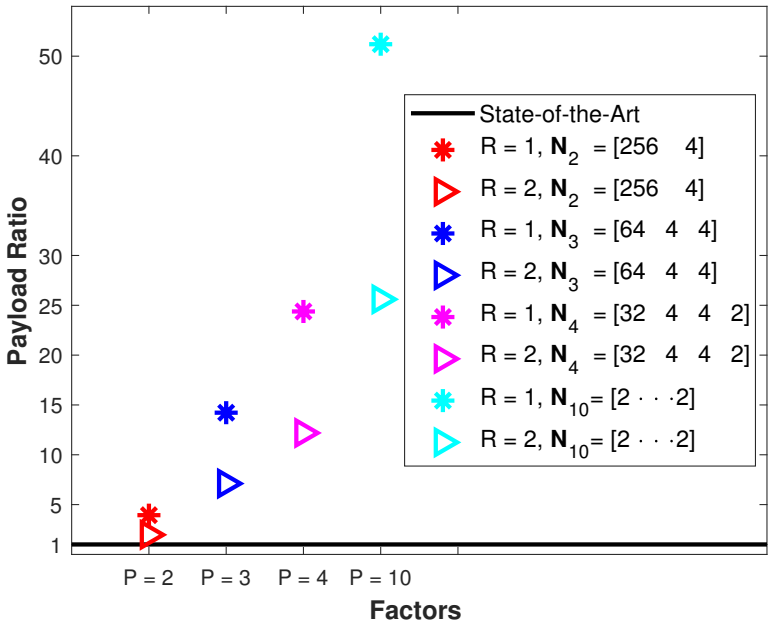

Source: Created by the author.

case of $P = 10$ and $N_p = 2$, for $p = \{1, \ldots, P\}$, the feedback overhead of the proposed approach is approximately fifty times smaller than the state-of-the art [116]. As noticed, with increasing P, the feedback duration of our proposed approach decreases, but also, as it will be discussed in Section 5.5, the SE in NLOS scenarios. Thus, to overcome this loss the RX can increase the number of components R at the cost of a higher feedback overhead. In this way, the proposed overhead-aware method shows off a trade-off between SE and feedback overhead.

5.3.2 Tucker-IRS Low-Rank Approximation

In this section, we consider the case where the RX node chooses to fit the phase-shift tensor $\mathcal{S}$ as a Tucker model, i.e.,

$$\mathcal{S} \approx \sum_{r_1=1}^{R_1} \cdots \sum_{r_P=1}^{R_P} \mathcal{G}_{r_1,\ldots,r_P} \left(\boldsymbol{s}_{r_1}^{(1)} \circ \ldots \circ \boldsymbol{s}_{r_P}^{(P)} \right) \in \mathbb{C}^{N_1 \times \ldots \times N_P}, \tag{5.23}$$

where $\mathcal{G} \in \mathbb{C}^{R_1 \times \ldots \times R_P}$ is the P-th order core tensor and $\boldsymbol{s}_{r_p}^{(p)} \in \mathbb{C}^{N_p \times}$ is the r_p-th column of the p-th factor matrix $\boldsymbol{S}^{(p)} \in \mathbb{C}^{N_p \times R_p}$, for $p = \{1, \ldots, P\}$ and $r_p = \{1, \ldots, R_p\}$. The main idea of using the Tucker model is to add more degrees of freedom to fit the IRS phase-shift tensor $\mathcal{S}$. In other words, comparing (5.16) with (5.23), in the P-th order Tucker tensor each factor can have different numbers of components which are combined based on the elements of a core tensor $\mathcal{G}$. The added degrees of freedom provided by the Tucker-IRS model results in a better SE than the PARAFAC-IRS model in NLOS scenarios, at the cost of a higher feedback overhead, as will be discussed in Section 5.5.

Figure 5.4 – Tucker-IRS feedback payload ratio for $N = 1024$.

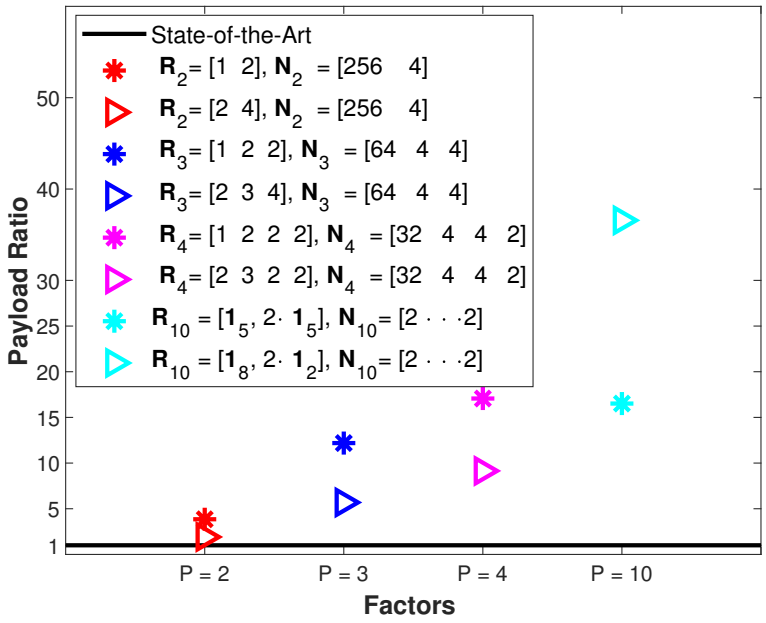

Source: Created by the author.

According to (2.74), the p-th mode unfolding of $\mathcal{S}$ is given by

$$[\mathcal{S}]_{(p)} \approx \boldsymbol{S}^{(p)} [\mathcal{G}]_{(p)} \left(\boldsymbol{S}^{(P)} \otimes \ldots \otimes \boldsymbol{S}^{(p+1)} \otimes \boldsymbol{S}^{(p-1)} \otimes \ldots \otimes \boldsymbol{S}^{(1)}\right)^{\mathrm{T}}. \tag{5.24}$$

Based on the Tucker-IRS model, the RX estimates each factor matrix $\boldsymbol{S}^{(p)} \in \mathbb{C}^{N_p \times R}$, for $p = \{1, \ldots, P\}$, and the core tensor $\mathcal{G}$. This estimation procedure can be performed using, e.g., the HOSVD algorithm [41] given in Algorithm 10. In this case, the RX estimates the factors matrices by computing the SVD of all P-mode unfolding matrices of $\mathcal{S}$ independently. Defining the SVD of $[\mathcal{S}]_{(p)}$ as $\boldsymbol{U}^{(p)}\Sigma^{(p)}\boldsymbol{V}^{\mathrm{H}}$, an estimate of $\boldsymbol{S}^{(p)}$ is given by

$$\hat{\boldsymbol{S}}^{(p)} = \boldsymbol{U}^{(p)}_{:1:R_p} \in \mathbb{C}^{N_p \times R_p}, \tag{5.25}$$

which is the truncation of the left singular matrix $\boldsymbol{U}^{(p)}$ to its first R_P columns, $p = \{1, \ldots, P\}$. The diagonal of the truncated singular matrix $\Sigma^{(p)}$, defined as $\boldsymbol{\sigma}^{(p)} = \mathrm{diag}(\Sigma^{(p)}_{1:R_p,1:R_p}) \in \mathbb{C}^{R_p \times 1}$, is stored to provide the weights to the R_p components in the quantization procedure. Once the P factor matrices are estimated, the RX obtains an estimate of the core tensor $\mathcal{G}$ as

$$\hat{\boldsymbol{g}} = \left(\hat{\boldsymbol{S}}^{(P)} \otimes \ldots \hat{\boldsymbol{S}}^{(1)}\right)^{\mathrm{H}} \boldsymbol{s}, \in \mathbb{C}^{R_1 \cdots R_P \times 1}, \tag{5.26}$$

where $\hat{\boldsymbol{g}} = \mathrm{vec}\left(\hat{\mathcal{G}}\right)$ and $\boldsymbol{s} = \mathrm{vec}\left(\mathcal{S}\right)$ are the vectorization of the core tensor and the IRS phase-shift tensor, respectively. The feedback duration of the Tucker-IRS model is given as

$$T_{\mathrm{F}}^{(\mathrm{Tucker})} = \frac{\mathrm{T}_{\mathrm{PR}} + \left(\sum_{p=1}^{P} R_p N_p b_{\mathrm{F}}^{(p)}\right) + \prod_{p=1}^{P} R_p b_{\mathrm{F}}^{(p)} + b_{\mathrm{F}}^{(\mathrm{w})} \sum_{p=1}^{P} (R_p - 1)}{B_{\mathrm{F}} \log\left(1 + \frac{p_{\mathrm{F}}|g_{\mathrm{F}}|^2}{B_{\mathrm{F}} N_0}\right)}, \tag{5.27}$$

Algorithm 10 Tucker-IRS HOSVD

1: **Inputs**: Tensor $\mathcal{S}$, the number of components R_p, for $p = \{1, \ldots, P\}$.
2: **for** $p = 1 : P$ **do**
3: Compute the SVD of the p-mode unfolding of $\mathcal{S}$ as

$$[\mathcal{S}]_{(p)} = \boldsymbol{U}^{(p)} \Sigma^{(p)} \boldsymbol{V}^{(p)\mathrm{H}}.$$

4: Store the diagonal of the truncated singular matrix defined as $\boldsymbol{\sigma}^{(p)} = \mathrm{diag}\left(\Sigma^{(p)}_{1:R_p,1:R_p}\right) \in \mathbb{C}^{R_p \times 1}$.
5: Set an estimation of $\boldsymbol{S}^{(p)}$ by truncating the left singular matrix to its first R_p columns

$$\hat{\boldsymbol{S}}^{(p)} = \boldsymbol{U}^{(p)}_{.1:R_p}.$$

6: **end for**
7: Compute an estimate of the core tensor $\boldsymbol{g} = \mathrm{vec}\,(\mathcal{G})$ as

$$\hat{\boldsymbol{g}} = \left(\hat{\boldsymbol{S}}^{(P)\mathrm{H}} \otimes \ldots \otimes \hat{\boldsymbol{S}}^{(1)\mathrm{H}}\right) \mathrm{vec}\,(\mathcal{S})\,.$$

8: Define $\hat{\mathcal{G}} = \mathcal{T}\{\mathrm{vec}\,(\hat{\boldsymbol{g}})\}$.
9: Return $\hat{\boldsymbol{S}}^{(1)}, \ldots, \hat{\boldsymbol{S}}^{(P)}$ and $\hat{\mathcal{G}}$.

where $\mathrm{T_{PR}}$ is the preamble cost that informs to the IRS controller the chosen tensor-based model, the number of factors P, and the number of components R_p, for $p = \{1, \ldots, P\}$. The term $\sum_{p=1}^{P} R_p N_p b_{\mathrm{F}}^{(p)}$ represents the cost, in bits, of the conveyed phase-shifts, $\prod_{p=1}^{P} R_p$ is the cost of the phase-shifts of the core tensor, and $b_{\mathrm{F}}^{(\mathrm{w})} \sum_{p=1}^{P} (R_p - 1)$ is the term related to the cost of the weighting factors.

Fig. 5.4 illustrates the ratio between state-of-the-art [116] and the Tucker-IRS model. First, we define the vector $\boldsymbol{R}_P = [R_1, \ldots, R_P] \in \mathbb{R}^{P \times 1}$ that contains the number of components for a certain number of factors P and $\boldsymbol{N}_P = [N_1, \ldots, N_P] \in \mathbb{R}^{P \times 1}$ the vector that contains the size of the factors for a certain number of factors P. We compare the ratio $N / \left(\boldsymbol{N}_p^{\mathrm{T}} \boldsymbol{R}_p + \prod_{p=1}^{P} R_p\right)$. Similar to the results of Fig. 5.3, when the number of factors P increases, the feedback overhead decreases, where in this case, for the Tucker-IRS model, we have almost forty times less than the state-of-the-art in the case of $P = 10$, $\boldsymbol{R}_{10} = [\mathbf{1}_8, 2 \cdot \mathbf{1}_2]$ and $\boldsymbol{N}_{10} = 2 \cdot \mathbf{1}_{10} \in \mathbb{R}^{10 \times 1}$. Comparing to the PARAFAC-IRS model, the Tucker-IRS in general have a higher feedback payload due the core tensor phase-shift feedback, costing $\prod_{p=1}^{P} R_p$ bits. However, as will be discussed in Section 5.5, the Tucker-IRS has more degrees of freedom, resulting a better parameter adjusting which increases the performance in NLOS scenarios.

5.4 Discussion on Quantization, Reconstruction and Parameter Choices

5.4.1 Phase-shift Quantization

After estimating the factors in Algorithms 9 or 10, the RX quantizes the phase-shifts of each factor with $b_F^{(p)}$ bits. Let us define $\tilde{\boldsymbol{a}} = Q\{\boldsymbol{a}, b\}$ as the quantization operation, which quantizes a phase-shift vector $\boldsymbol{a}$ with b bits. For the PARAFAC-IRS model, we have the following quantized factors $\tilde{\boldsymbol{s}}_r^{(p)} = Q\left\{\hat{\boldsymbol{s}}_r^{(p)}, b_{\mathrm{F}}^{(p)}\right\}$ for $p = \{1, \ldots, P\}$ and $r = \{1, \ldots, R\}$. In addition, for the Tucker-IRS model, we have the following quantized factors and core tensor $\tilde{\boldsymbol{s}}_{r_p}^{(p)} = Q\left\{\hat{\boldsymbol{s}}_{r_p}^{(p)}, b_{\mathrm{F}}^{(p)}\right\}$ and $\tilde{\mathcal{G}}_{r_1,\ldots,r_P} = Q\left\{\hat{\mathcal{G}}_{r_1,\ldots,r_P}, b_{\mathrm{F}}^{(p)}\right\}$, for $p = \{1, \ldots, P\}$ and $r_p = \{1, \ldots, R_p\}$. We use the following codebook to quantize the phase-shifts of the p-th factor,

$$C_{\phi}^{(p)} = \left\{-\pi + \frac{2\pi}{2^{b_{\mathrm{F}}^{(p)}}},\ -\pi + \frac{4\pi}{2^{b_{\mathrm{F}}^{(p)}}},\ \ldots,\ \pi\right\}.$$

5.4.2 Weighting Factor Quantization

For the PARAFAC-IRS model, let us define $\lambda_{\max}$ as the largest element of $\boldsymbol{\lambda}$. Normalizing $\boldsymbol{\lambda}$ by $\lambda_{\max}$ we have $\boldsymbol{\lambda}' = \boldsymbol{\lambda}/\lambda_{\max} \in \mathbb{R}^{R\times 1}$. Since the largest element of $\boldsymbol{\lambda}'$ is one, we do not need to quantize this element. Hence, we define a new vector $\bar{\boldsymbol{\lambda}} \in \mathbb{R}^{R-1\times 1}$ that contains all elements of $\boldsymbol{\lambda}'$, with the exception the of the largest one. Then, we quantize the weighting vector by defining $\tilde{\bar{\boldsymbol{\lambda}}} = Q\left\{\bar{\boldsymbol{\lambda}}, b_{\mathrm{F}}^{(\mathrm{w})}\right\}$. Finally, we define $\tilde{\boldsymbol{\lambda}} \in \mathbb{R}^{R\times 1}$ as the quantized weighting vector by inserting in the correct position the largest element of $\boldsymbol{\lambda}'$ (one) in $\tilde{\bar{\boldsymbol{\lambda}}} \in \mathbb{R}^{R-1\times 1}$. At the end, the weighting vector quantization for the PARAFAC-IRS model cost $(R-1)b_{\mathrm{F}}^{(\mathrm{w})}$ bits.

For the Tucker model, a similar approach is made, with the difference that there are P weighting vectors sorted by their largest value due to the SVD procedure. Considering the p-th weighting vector $\boldsymbol{\sigma}^{(p)} \in \mathbb{R}^{R_p\times 1}$, we normalize it by the first element, yielding $\boldsymbol{\sigma}^{(p)\prime} = \boldsymbol{\sigma}^{(p)}/\sigma_1^{(p)}$. For the quantization, we define a vector $\bar{\boldsymbol{\sigma}}^{(p)} \in \mathbb{R}^{R_p-1\times 1}$ that contains all elements of $\boldsymbol{\sigma}^{(p)\prime}$ with exception of the first one. Then, we define the quantized p-th weighting factor as $\tilde{\bar{\boldsymbol{\sigma}}}^{(p)} = Q\left\{\bar{\boldsymbol{\sigma}}^{(p)}, b_{\mathrm{F}}^{(\mathrm{w})}\right\} \in \mathbb{R}^{R_p-1\times 1}$. Finally, for the p-th quantized vector, we define the quantized vector $\tilde{\boldsymbol{\sigma}}^{(p)} = [1, \tilde{\boldsymbol{\sigma}}^{(p)\prime}] \in \mathbb{R}^{R_p\times 1}$. At the end, the quantization of the P weighting factors for the Tucker model costs $b_{\mathrm{F}}^{(\mathrm{w})} \cdot \sum_{p=1}^{P}\left(R_p - 1\right)$ bits. For both PARAFAC-IRS and Tucker-IRS models, we define the following amplitude codebook

$$C_{\mathrm{w}} = \{0.01,\ 0.01 + l,\ 0.01 + 2l,\ \ldots,\ 1\}, \tag{5.28}$$

where $l = \frac{1-0.01}{2^{b_{\mathrm{F}}^{(\mathrm{w})}}-1}$ is a pre-defined step. For simplicity, the values of the amplitudes in (5.28) are rounded to the second decimal point.

5.4.3 IRS Phase-shift Vector Reconstruction

After quantization, the RX conveys the factors to the IRS controller. Then, the phase-shift vector is reconstructed as

$$\boldsymbol{s} = e^{j\angle\hat{\boldsymbol{s}}} \in \mathbb{C}^{N\times 1}, \tag{5.29}$$

where $\hat{\boldsymbol{s}}$ is given by

$$\hat{\boldsymbol{s}} = \sum_{r=1}^{R} \tilde{\lambda}_r \left(\tilde{\boldsymbol{s}}_r^{(P)} \otimes \ldots \otimes \tilde{\boldsymbol{s}}_r^{(1)} \right), \tag{5.30}$$

for the PARAFAC-IRS model, while for the Tucker-IRS model, $\hat{\boldsymbol{s}}$ is rebuilt as

$$\hat{\boldsymbol{s}} = \sum_{r_1=1}^{R_1} \ldots \sum_{r_P=1}^{R_P} \tilde{\mathcal{G}}_{r_1,\ldots,r_P} \left[\left(\tilde{\sigma}_{r_P}^{(P)} \tilde{\boldsymbol{s}}_{r_P}^{(P)} \right) \otimes \ldots \otimes \left(\tilde{\sigma}_{r_1}^{(1)} \tilde{\boldsymbol{s}}_{r_1}^{(1)} \right) \right]. \tag{5.31}$$

5.4.4 On the Effect of the Factorization Parameters

In this section, we discuss the choice of the factorization parameters and the system performance implications.

- **Number of factors** P: This parameter defines the total number of factors used in the LRA. Its minimum value for the proposed factorization is $P = 2$, i.e., $P = 1$ means that no factorization is employed, its maximum value is $\log_2(N)$, for the case where all the factors have size $N_p = 2$ for $p = \{1, \ldots, P\}$. By increasing the value of P, the number of factors increases, allowing to reduce the size of the factor components N_p. Consequently, increasing P reduces the phase-shift feedback overhead. Nevertheless, by selecting the minimum value of P, the size of each factor component increases, which increases the SE at the cost of a higher feedback overhead.
- **Number of components**: For the PARAFAC model, we have R components, while for the Tucker model we have $\sum_{p=1}^{P} R_p$ components. For both models, the number of components is a performance indicator since when it is increased, the approximation error of the LRA in (5.16) and (5.23) decreases. The RX selects its value based on the estimated channels. For example, if the channels have low-rank, or in the presence of a moderate/strong LOS component, the RX may choose $R = 1$. Also, $R = 1$ (PARAFAC model) or $R_p = 1$ (for the Tucker model) are the choices that minimizes the feedback overhead. On the other hand, by increasing R (or R_p), the SE increases at the cost of a higher feedback load.
- **Size of factor components** N_p: The size of the factor components indicates the total number of independent phase-shifts in the proposed solution, which it also affects the performance. For example, for $N = 256$, $P = 2$ and $R = 1$, two possible configurations are $(N_1 = 128, N_2 = 2)$ and $(N_1 = N_2 = 16)$. For the first choice, the

system has more independent phase-shifts (130), thus a higher SE. However, its feedback overhead is higher than the second configuration that requires only 32 phase-shifts to be reported in the feedback channel.

5.4.5 On the Effect of the Phase-shift and Weighting Factor Quantization

After the factorization step, the phase-shifts of the factor matrices $\boldsymbol{S}^{(p)}$ are quantized before being conveyed to the IRS controller. From the fact that the proposed method factorizes the IRS phase-shift vector into P smaller factors, we can select different numbers of bits for the quantization of each factor, unlike the conventional IRS-assisted systems, where the RX (or TX) conveys the N phase-shifts with the same quantization resolution of b_{F} bits. The proposed method allows the system to adapt the phase-shift resolution of the factors to the available control link capacity, i.e., for each factor we may have a different resolution of $b_{\mathrm{F}}^{(p)}$ in bits, $p = \{1, \ldots, P\}$, providing more flexibility to the system design. Regarding the weighting factors, they play a more important role when the number of components $R > 1$ (in the PARAFAC model), or $R_p > 1$, $p = \{1, \ldots, P\}$ (in the Tucker model), since they control the importance of the rank-one components in each model.

5.5 Simulation Results

In this section, we evaluate the performance of the proposed IRS phase-shift overhead-aware feedback model in terms of feedback duration, achievable data rate, SE and EE. To this end, $L = 5 \cdot 10^3$ Monte Carlo runs were performed, where in each trial the channels are generated according (5.3) and (5.2). In Figs. 5.5-5.9, we set $\alpha_H = \alpha_G = 1$, and consider $K_H = K_G = K$ to simplify the presentation of the figures. However, we have tested the results for a broad range of channel models and parameter settings and observed the same qualitative conclusions as those presented.

5.5.1 IRS Phase-shift Normalized Mean Square Error

In this section we discuss the accuracy of the PARAFAC-IRS and the Tucker-IRS LRA models. To this end, we compare the NMSE of the optimized IRS phase-shift vector, given in (3.17), with the proposed LRA models, the PARAFAC-IRS model and the Tucker-IRS model, after the phase-shift vector reconstruction in the IRS controller. For the sake of illustration, we consider continuous phase-shifts and weighting factors, thus being an ideal scenario. The NMSE is calculated as

$$\mathrm{NMSE} = \frac{1}{L} \sum_{l=1}^{L} \frac{||\boldsymbol{s}_l - \hat{\boldsymbol{s}}_l||_2^2}{||\boldsymbol{s}_l||_2^2}, \tag{5.32}$$

where L is the total number of Monte Carlo trials, and $\hat{\boldsymbol{s}}_l$ is the reconstructed IRS phase-shift vector using the PARAFAC-IRS and the Tucker-IRS models, in (5.30) and (5.31), respectively.

Figure 5.5 – NMSE between the optimum IRS phase-shift vector given in (3.17) and the PARAFAC-IRS (a) and Tucker-IRS (b) LRA models, in (5.30) and (5.31), for different number of components.

(a) NMSE PARAFAC-IRS model.

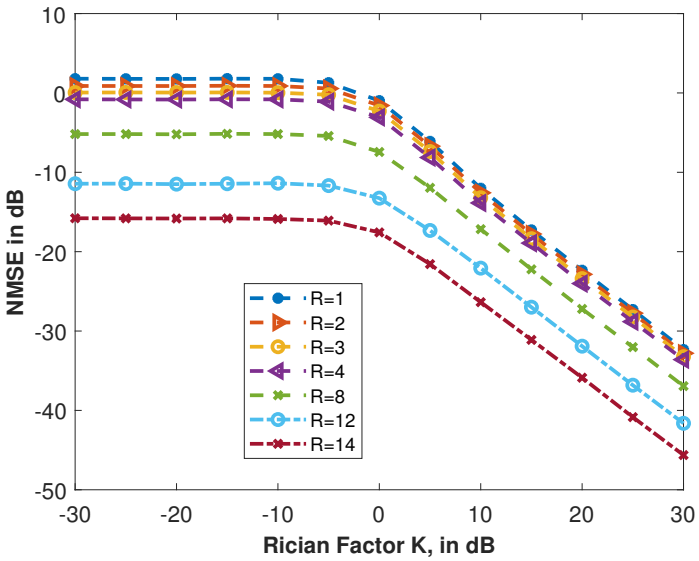

(b) NMSE Tucker-IRS model.

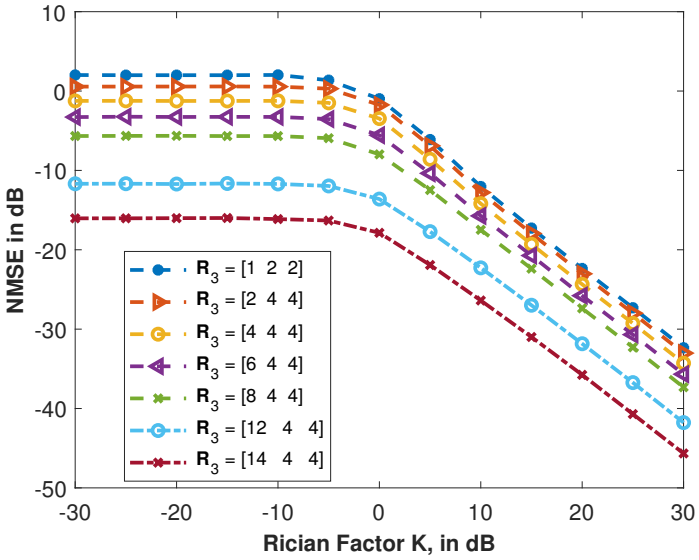

Source: Created by the author.

Assuming the setup $N = 1024$ elements, $P = 3$ factors with sizes $N_1 = 64$, $N_2 = 4$, and $N_3 = 4$, from Figs. 5.5 (a) and (b), it becomes clear that as the number of components R (for the PARAFAC-IRS model) and the number of components in $\boldsymbol{R}_3$ (for the Tucker-IRS model) increases, the NMSE decreases. This is from the fact that we are adding more components to the tensor model to fit the IRS phase-shift vector. Also, when the Rician factor K increases, the NMSE decreases. This is explained by the fact that the LOS components of the channels $\boldsymbol{G}$ and $\boldsymbol{H}$ are separable with a Vandermonde structure, and every Vandemonde vector can be decomposed as the Kronecker product of smaller factors, which is the main idea of the proposed models. In

Figure 5.6 – Illustration of the ratio of the weighting factors.

(a) Ratio of the weighting factors of the PARAFAC-IRS model.

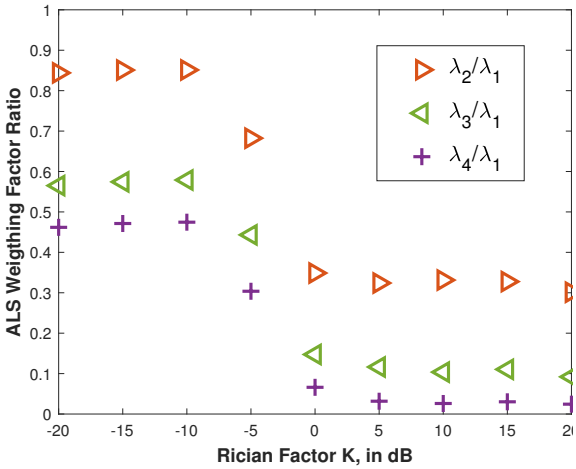

(b) Ratio of the weighting factors of the Tucker-IRS model for $[\mathcal{S}]_{(1)}$.

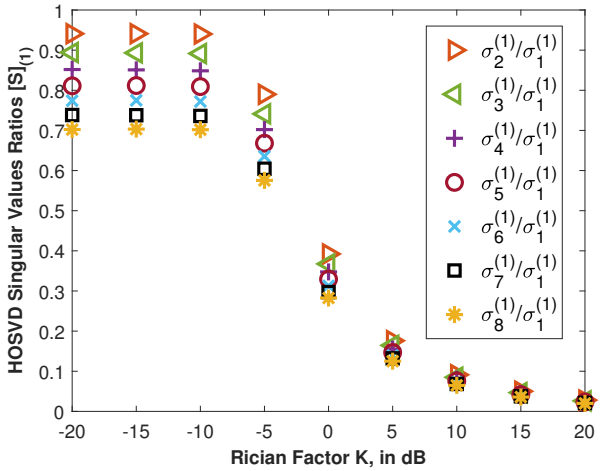

(c) Ratio of the weighting factors of the Tucker-IRS model for $[\mathcal{S}]_{(2)}$.

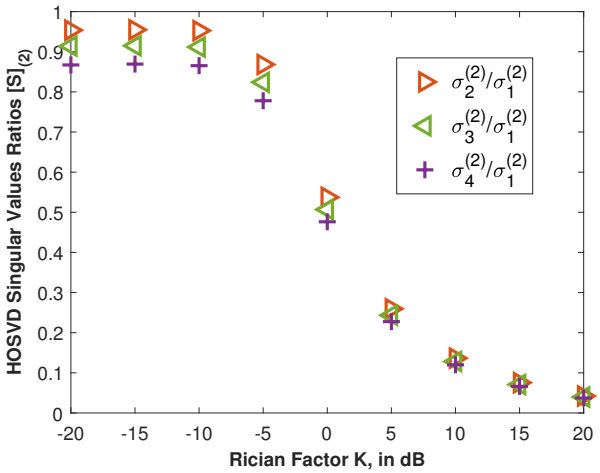

(d) Ratio of the weighting factors of the Tucker-IRS model for $[\mathcal{S}]_{(3)}$.

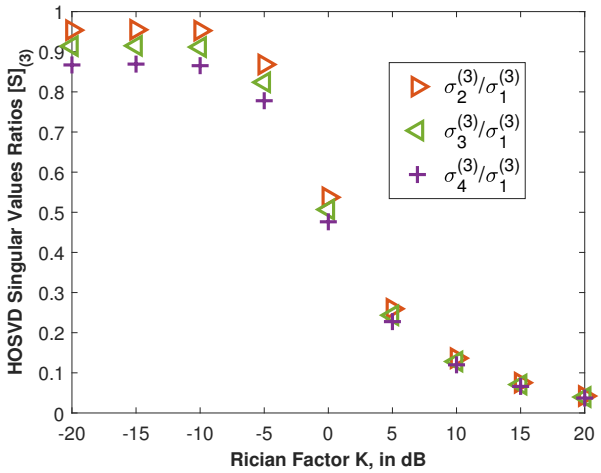

Source: Created by the author.

other words, when $K \to \infty$ the optimization of the IRS vector aligns the IRS phase-shifts with the LOS components of the channels $\boldsymbol{G}$ and $\boldsymbol{H}$, which are separable and can be approximated using a low-rank tensor model.

5.5.2 Distribution of the Weighting Factors in the PARAFAC-IRS and the Tucker-IRS models

In this section, the relationship between the weighting factors in the PARAFAC-IRS and the Tucker-IRS models are discussed. To this end, we assume $P = 3$ factors, $R = 4$ components for the PARAFAC-IRS, and for the Tucker-IRS model, we consider the vector of components $\boldsymbol{R}_3 = [R_1, R_2, R_3]^{\mathrm{T}} = [8,4,4]^{\mathrm{T}}$. In Fig. 5.6 (a), we assume that the weighting factor vector $\boldsymbol{\lambda} = [\lambda_1, \lambda_2, \lambda_3, \lambda_4]$ of the PARAFAC-IRS model components are sorted such that $\lambda_1 > \lambda_2 > \lambda_3 > \lambda_4$. As expected we can notice that the weighting factor ratio decreases when K increases. However, the gap between the ratios of, e.g., λ_2/λ_1 and λ_3/λ_1 are not negligible,

indicating a sensitivity in the quantization process, even in the LOS regime. In Figs. 5.6 (b)-(d), we illustrate the distribution of the weighting factor ratios in the Tucker-IRS model using the HOSVD Algorithm 10, i.e., for all factors $[\mathcal{S}]_{(1)}$, $[\mathcal{S}]_{(2)}$, and $[\mathcal{S}]_{(3)}$ the weights (singular values) are sorted as $\sigma_1^{(p)} > \sigma_2^{(p)} > \ldots > \sigma_{r_p}^{(p)}$, for $p = \{1,2,3\}$ and $r_p = \{1,\ldots R_p\}$. In Fig. 5.6 (b) illustrates the ratio distribution of the first factor $[\mathcal{S}]_{(1)} \in \mathbb{C}^{64\times 16}$, assuming the truncation in $R_1 = 8$ components, while in Fig. 5.6 (c) we have the ratio for the second factor $[\mathcal{S}]_{(2)} \in \mathbb{C}^{4\times 256}$, assuming the truncation in $R_2 = 4$ components, and finally, in Fig. 5.6 (d) we show the weighting factors ratio for the third factor $[\mathcal{S}]_{(3)} \in \mathbb{C}^{4\times 256}$, assuming the truncation in $R_3 = 4$ components. As expected, in Figs. 5.6 (b)-(d), as K increases, the relative importance of the components decreases. But, different from the PARAFAC-IRS model, the gap between the ratios of the components is pratically negligible for $K > 0$ dB, indicating that the Tucker-IRS model is less sensitive than the PARAFAC-IRS model in the weighting factor quantization process.

5.5.3 PARAFAC-IRS vs Tucker-IRS

As a first experiment, we compare, in terms of achievable data rate, the two proposed strategies, PARAFAC-IRS and Tucker-IRS, with the state-of-the-art method [116], where the IRS phase-shift vector is not factorized. The achievable data rate is given by

$$\log_2\left(1+\frac{|\boldsymbol{w}^{\mathrm{H}}\boldsymbol{G}\mathrm{diag}\,(\boldsymbol{s})\,\boldsymbol{H}\boldsymbol{q}|^2}{\sigma_b^2}\right), \text{in bits/s/Hz}, \tag{5.33}$$

where $\boldsymbol{s} \in \mathbb{C}^{N\times 1}$ is the the optimum IRS phase-shift vector, which is given in (5.30) for the PARAFAC-IRS model and in (5.31) for the Tucker model.

In Fig. 5.7, we assume $P = 3$ for the proposed IRS factorization models, with $N_1 = 64$, and $N_2 = N_3 = 4$. In Fig. 5.7 (a), we compare the models in an ideal scenario with continuous phase-shift and continuous values for the weighting factors. As expected, when the number of components R or in $\boldsymbol{R}_{(3)}$ increases, the achievable data rate also increases, and we can observe that for the PARAFAC-IRS model with $R = 16$ and for the Tucker-IRS model with $\boldsymbol{R}_3 = [16,4,4]$, the proposed models achieves the optimum performance of the benchmark method [116], i.e., the tensor models fits.

However, in practice, both the phase-shift and the weighting factors have to be quantized. As illustrated in Fig. 5.7 (b), there is an optimal point for the PARAFAC ($R = 4$, for this case) since when $R > 4$ the performance degrades due to an overfitting. For the Tucker model, when the number of components of $\boldsymbol{R}_3$ increases, the performance in the NLOS region ($K < -5$ dB) also improves, but at the cost of a higher feedback overhead. Note that, for the moderate/strong LOS scenario ($K > 5$ dB), the number of components for both models does not give a noticeable performance enhancement. In this way, a proper model for a NLOS scenario would be the Tucker one, while PARAFAC is preferable in moderate/strong LOS cases, since it leads to the best performance with the lowest feedback cost.

Figure 5.7 – Comparison between the state-of-the-art [116], PARAFAC-IRS and Tucker-IRS models with different numbers of components. $N = 1024$, $P = 3$, with $N_1 = 64$, $N_2 = 4$, and $N_3 = 4$.

(a) Ideal scenario with no quantization.

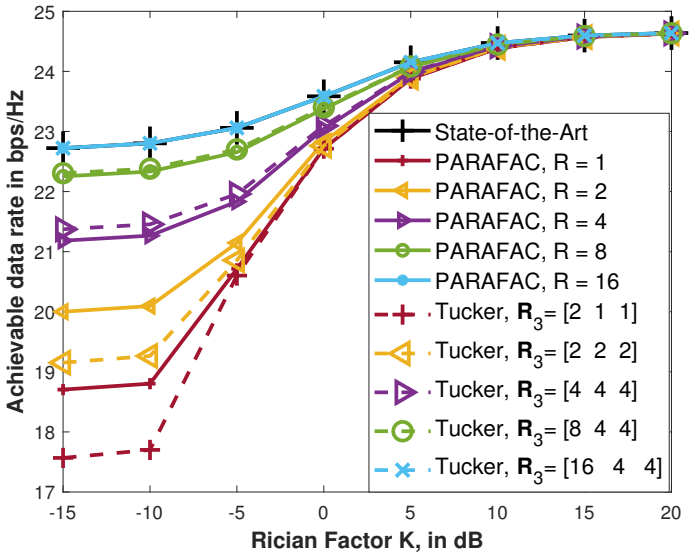

(b) Feedback payload (F.P.) in bits.

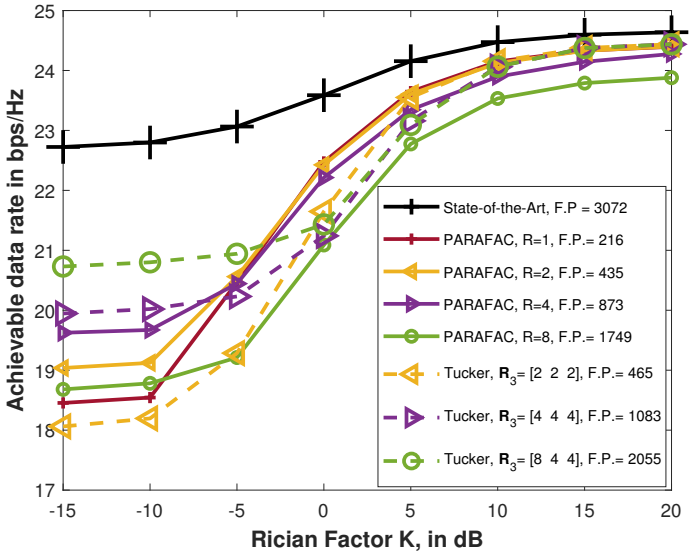

Source: Created by the author.

In the following experiments, we consider the PARAFAC-IRS model, due its simplicity and lower phase-shift and weight feedback cost. However, we have tested the results for the cases with Tucker method and observed the same qualitative conclusions as those presented.

5.5.4 On the Effect of the Number of Factors P

In Fig. 5.8, we compare the achievable data rate of the PARAFAC-IRS model with $R = 1$, by varying the number of factors. We can observe that, for the NLOS region ($K < -5$ dB), increasing P leads to a degradation on the performance. This is due to the fact that, for a

Figure 5.8 – For an IRS with $N = 1024$, TX and RX with $M_R = M_T = 2$ and $b_{\mathrm{F}}^{(p)} = b_{\mathrm{F}} = 3$ bits, for the IRS phase-shift quantization resolution, for $p = \{1, \ldots, P\}$.

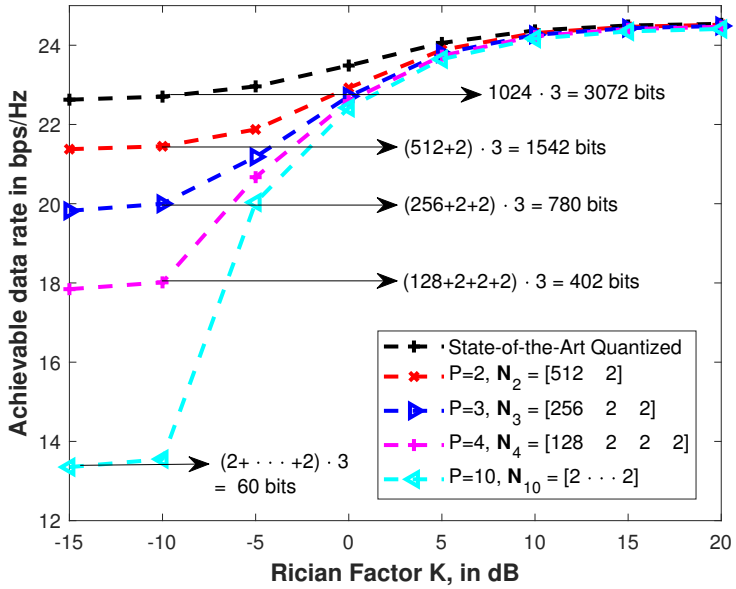

Source: Created by the author.

Figure 5.9 – Feedback payload for the PARAFAC-IRS model with $R = 1$, varying the number of IRS elements.

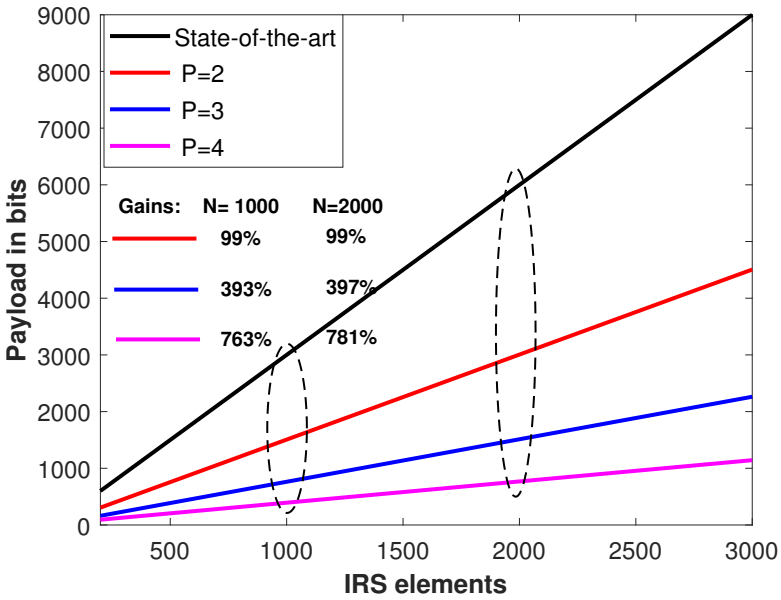

Source: Created by the author.

larger P, we have less independents phase-shifts. For example, for $P = 10$, the phase-shifts of the IRS elements are given by the sum of 10 factorized phase-shifts. However, when the Rician factor K increases, the performance gap between our proposed model and the state-of-the-art [116] reduces. This is explained by the fact that, the IRS phase-shift optimization is based on the channel estimation, thus when K increases, the LOS components becomes stronger, and we have a better approximation of the PARAFAC-IRS model. In terms of feedback overhead, when

Figure 5.10 – Performance of the PARAFAC-IRS method by varying the resolution $b_{\mathrm{F}}^{(p)}$ per factor, for fixed control link of 1024 bits.

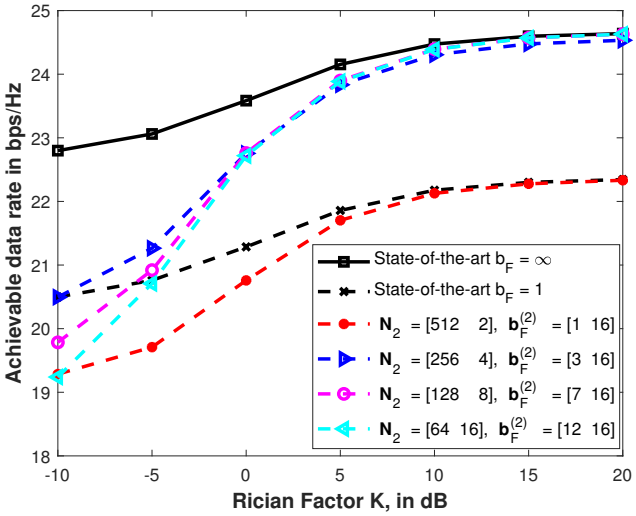

Source: Created by the author.

$P = 2$ and for the $K < -5$ dB region, our proposed method has a data rate loss of approximately 1bps/Hz. However, the feedback overhead is 50% less than that of the benchmark solution [116]. On the other hand, when the scenario changes to $K > 5$ dB, the proper parameter choice is $P = 10$, since this configuration has a negligible performance loss compared to the state-of-the-art one, while having a lower feedback cost compared to the other proposed configurations ($P = 2, 3, 4$).

Physically, the results illustrated on Fig. 5.8 can be interpreted as a performance adaptation in the NLOS case, i.e., the RX can properly choose the factorization parameters to meet a required data rate performance or feedback saving. For instance, in this example, by choosing $P = 10$, the RX can afford more often feedback than configurations with smaller values of P.

For a better understanding of the merits of the proposed method, Fig.5.9 shows the feedback payload in bits by varying the number of IRS elements. As shown, for different methods the payload increases linearly with the number of IRS elements. For a given P, we may have different sets of factor sizes defined by $\boldsymbol{N}_{\mathrm{P}} = [N_1, \ldots, N_P]^{\mathrm{T}} \in \mathbb{R}^{P \times 1}$, where the values of P are set to $P = 2, 3, 4$. We select the size configuration that leads to the better performance, which is the one that has the maximum possible number of independent phase-shifts. For example, assuming $N = 1000$, the size configuration is $\boldsymbol{N}_2 = [500, 2]$ when $P = 2$, $\boldsymbol{N}_3 = [250, 2, 2]$ for $P = 3$, and $\boldsymbol{N}_4 = [125, 2, 2, 2]$ for $P = 4$. Thus, it becomes clear that increasing P drastically reduces the feedback overhead.

5.5.5 On the Effect of the Factor Quantization

Here, we evaluate the performance of the proposed method in a limited feedback channel, i.e., we assume that the feedback control link has a maximum capacity of 1024 bits. In

Table 5.1 – Network parameters.

$P_{\max}/P_{c,0}/P_{c,n}$	$B_{\max}$	N_0	α_H/α_G	μ/μ_{F}
45/45/10 dBm	100 MHz	-174 dBm/Hz	110/110 dB	1/1

Source: Created by the author.

this case, traditional quantization applied to the unconstrained IRS phase shift vector (without factorization) is limited to a one bit resolution. We assume this challenging scenario to observe the performance impact of the proposed method when the resolution of the individual factors are adapted. To this end, we assume $N \cdot b_{\mathrm{F}} \geq \boldsymbol{N}_{\mathrm{P}}^{\mathrm{T}} \cdot \boldsymbol{b}_{\mathrm{F}}^{(\mathrm{P})}$.

In Fig. 5.10, different sets of size configurations for $P = 2$ are evaluated, with different resolutions per factor. The configuration $\boldsymbol{N}_2 = [512, 2]$ has the worst performance since the first factor (512 elements) can only be quantized with 1 bit. However, when the size of the factors is reduced, the resolution per factor can be increased accordingly to meet the limited control link capacity limit. For instance, when $\boldsymbol{N}_2 = [256, 4]$ and $\boldsymbol{b}_{\mathrm{F}}^{(p)} = [3, 16]$, the total number of bits is $256 \cdot 3 + 4 \cdot 16 = 832$. We can observe that, by increasing the resolution of the factors, the performance gets closer to that of the state-of-the-art phase-shift without quantization (solid curve). In particular, note that for $K > -5$ dB, our approach provides the best results. Thus, the proposed method can not only reduce the feedback overhead, as illustrated in Figs. 5.8 and 5.9, but also it effectively provides higher data rates than traditional quantization over the unconstrained IRS phase shifts, approaching the continuous phase-shift case.

5.5.6 Total System SE and EE Evaluation

In this section, we evaluate the performance, in terms of SE and EE, of the proposed method by considering the total system rate, i.e., taking into account the channel estimation procedure duration and the IRS phase-shift feedback duration. To this end, we make use of the expressions given in (3.20) and (3.21). The channel estimation period, in (3.20), is given as $\mathrm{T}_E = (M_T N + 1)T_0$, where $T_0 = 0.8\mu$ seconds denotes the duration of the pilot tones [116]. The frame duration is given by $T = \mathrm{T}_{PD} + \mathrm{T}_{\mathrm{F}}$, where $\mathrm{T}_{PD} = \mathrm{T}_E + \mathrm{T}_D$, is divided into 30% for pilot transmissions (T_E) and 70% for data transmission T_D. Regarding the power parameters of (3.21), we have $P_{\mathrm{E}} = P_0(1 + NM_T)T_0/T$, where $P_0 = 0.8$ mW is the pilot tone power. Other parameter definitions can be found in Table 5.1. The feedback channel g_{F} is generated from a circular symmetric complex Gaussian distribution, normalized by $\sqrt{\beta_F} = \sqrt{\alpha_H} = \sqrt{\alpha_G}$ to account for the effects of pathloss and shadowing, as given in Table 5.1. In our next experiments, we assume $K = 10$ dB, $N = 1024$. For the proposed method, we consider the PARAFAC-IRS model with $R = 1$. As for the number of factors, we study three configurations, with $P = 2$, ($\boldsymbol{N}_2 = [512, 2]$), $P = 3$ ($\boldsymbol{N}_3 = [256, 2, 2]$) and $P = 10$ ($\boldsymbol{N}_{10} = [2, \ldots, 2] \in \mathbb{R}^{10\times 1}$).

In Figs.5.11 and 5.12, we analyze the total SE and EE of the proposed method with the state-of-the-art [116], by varying the feedback bandwidth $B_{\mathrm{F}} = B_{\max} - B$, where $B_{\max}$ is the total available bandwidth given in Table 5.1. As shown, in Figs. 5.11a and 5.11b, when the number of factors increases the feedback duration reduction pays off in the total system SE and

Figure 5.11 – SE and EE performance of the proposed method varying the feedback bandwidth, with $N = 1024$, $M_R = M_T = 16$, $b_{\mathrm{F}}^{(p)} = b_{\mathrm{F}} = 3$ bits, for $p = 2, 3, 10$, for a Rician factor $K = 10$ dB.

(a) SE performance of the state-of-the-art and the proposed method.

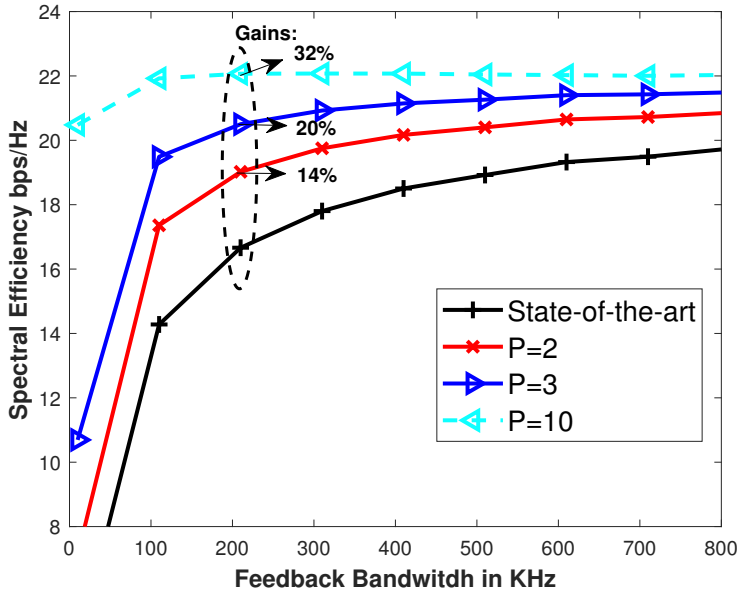

(b) EE performance of the state-of-the-art and the proposed method.

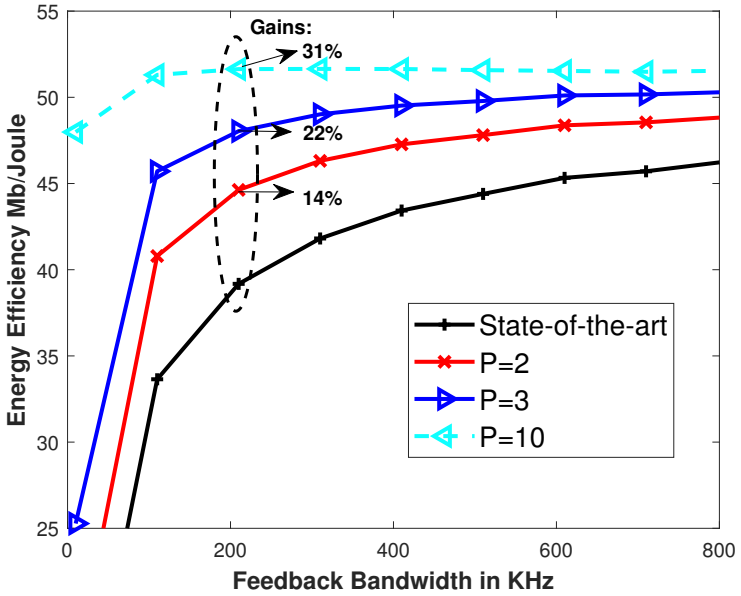

Source: Created by the author.

EE. The proposed method achieves a gain in the SE of 32% for $P = 10$, 20% for $P = 3$, and 14% for $P = 2$, over the state-of-the-art, considering the $B_{\mathrm{F}} = 200$ kHz, with a similar gain in the EE.

In Figs. 5.12a and 5.12b we compare the proposed PARAFAC-IRS model under $R = 1$ and $P = 10$ with the state-of-the-art by varying the number of antennas. In Fig. 5.12a, we

Figure 5.12 – SE and EE performance of the proposed method varying the feedback bandwidth, with $N = 1024$, $b_{\mathrm{F}}^{(p)} = b_{\mathrm{F}} = 4$ bits, for $p = 2, 3, 10$, for a Rician factor $K = 10$ dB.

(a) SE performance of the state-of-the-art and the proposed method.

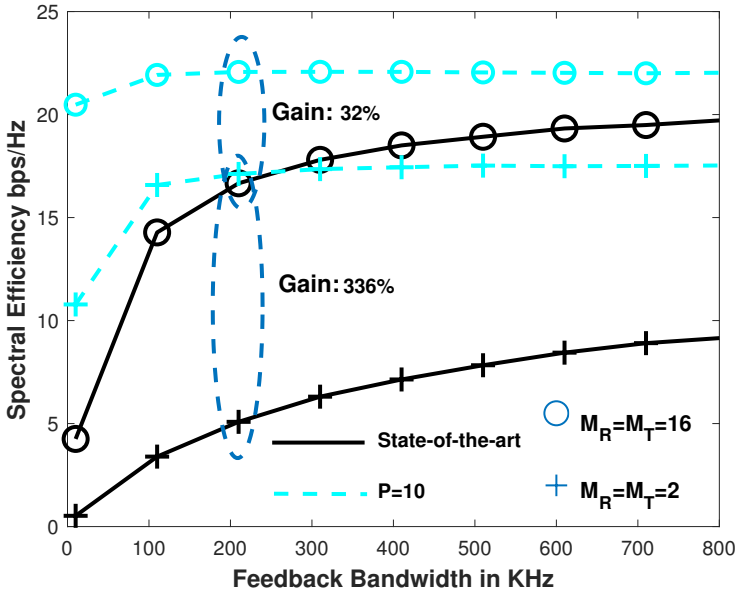

(b) EE performance of the state-of-the-art and the proposed method.

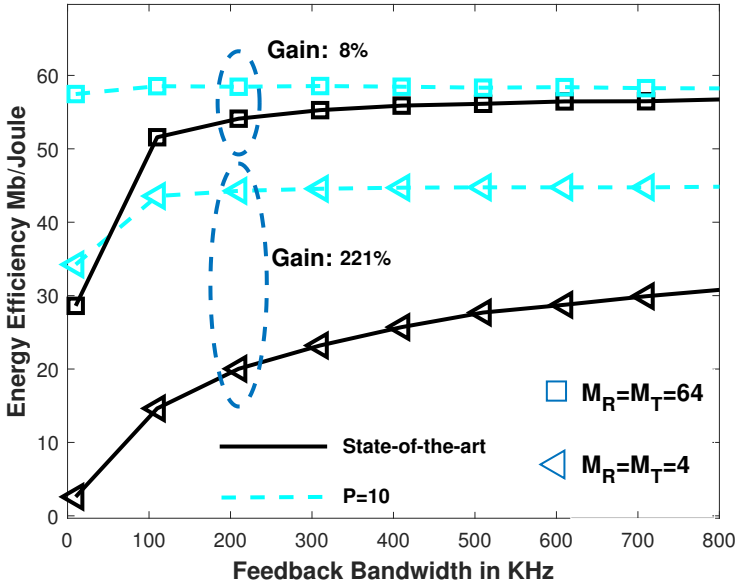

Source: Created by the author.

observe that, for a feedback bandwidth $B_{\mathrm{F}} \leq 200$ kHz, the proposed PARAFAC-IRS model with $M_R = M_T = 2$ antennas achieves the same performance as the state-of-the-art model equipped with $M_R = M_T = 16$ antennas. However, matching the number of antennas at the receiver and the transmitter sides, the proposed PARAFAC-IRS model has a gain of 336% for $M_R = M_T = 2$, and

Figure 5.13 – EE and SE performance of the proposed method varying the feedback power, with $N = 1024$, $M_R = M_T = 2$, $b_{\mathrm{F}}^{(p)} = b_{\mathrm{F}} = 3$ bits, for $p = 2, 3, 10$, Rician factor $K = 10$ dB.

(a) SE performance of the state-of-the-art and the proposed method.

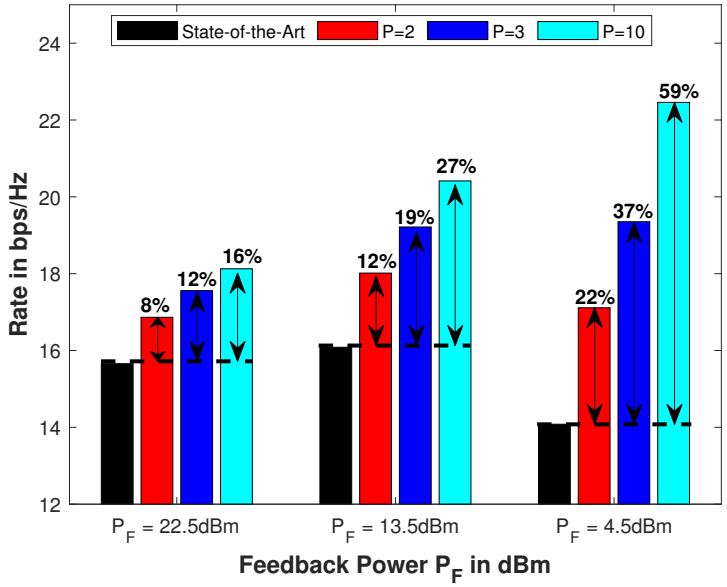

(b) EE performance of the state-of-the-art and the proposed method.

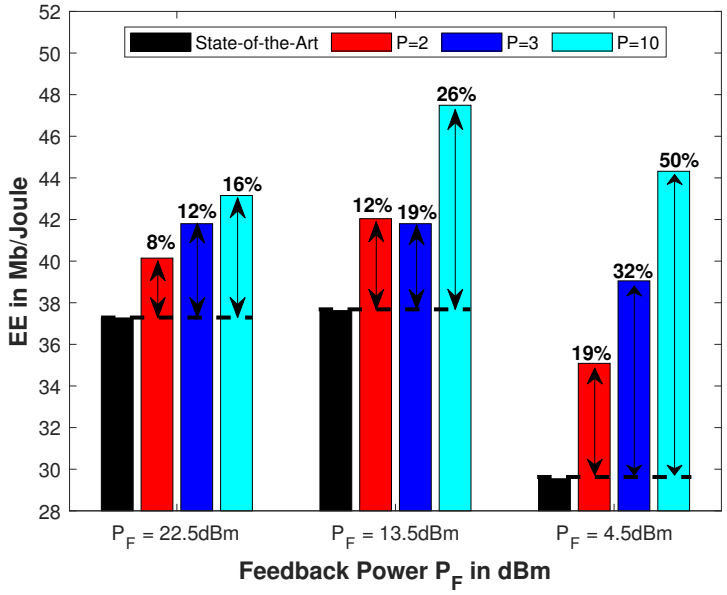

Source: Created by the author.

32% when $M_R = M_T = 16$. Likewise, in terms of EE, in Fig. 5.12b, for a feedback bandwidth $B_{\mathrm{F}} \leq 200$ kHz, the proposed PARAFAC-IRS model outperforms the state-of-the-art model in all antennas configuration, having a gain of 221% assuming $M_R = M_T = 4$, and 8% for the $M_R = M_T = 64$ configuration. Finally, Figs. 5.13a and 5.13b show the SE and EE performances

of the proposed method as a function of the feedback power p_{F}, with $p_{\mathrm{F}} = P_{\max} - p_{\mathrm{TX}}$. We notice that the proposed configurations provide the best results in all scenarios.

To summarize the results illustrated in Figs.5.11-5.13, we conclude that the proposed tensor-based LRA IRS phase-shift factorization models allows to reduce the number of phase-shifts to be conveyed to the IRS-controller, which significantly reduces the feedback overhead, resulting in SE and EE performance enhancements. In addition, our approach reaches similar performance to the non-factorized IRS, especially in moderate/strong LOS scenarios, as it can be seen in Figs. 5.7-5.10. Also, we show that the proposed PARAFAC-IRS model outperforms the state-of-the-art in SE and EE when takes into account the total system rate.

From a system-level viewpoint, the network can resort to the proposed overhead-aware IRS model to increase the feedback periodicity, i.e., by providing more frequent feedback, which is crucial in fast time-varying channels, where the IRS should be reconfigured more frequently to follow the environment changes. Moreover, the proposed IRS factorization methods allow the network to multiplex more IRS phase-shifts in the same feedback channel, which is useful to accommodate multi-user IRS-assisted communications.

5.6 Summary

In this chapter, we proposed two IRS phase-shift overhead-aware feedback methods based on tensor signal processing, namely, PARAFAC-IRS and Tucker-IRS. We showed that the proposed methods significantly reduce the IRS phase-shift feedback overhead, compared to the state-of-the-art approach, where the IRS phase-shifts are not factorized. The PARAFAC-IRS method is preferable in the case of moderate/strong LOS scenarios, achieving a spectral efficiency that is close to that of the state-of-the-art, while providing a feedback overhead reduction. Moreover, in NLOS scenarios, the Tucker-IRS model achieves a higher data rate than the PARAFAC-IRS model at the expense of a higher feedback overhead. By controlling the factorization parameters, we showed how to trade off data rate for feedback-overhead, allowing the network controller to adapt the IRS factorization parameters to meet a determined quality of service.

6 CONCLUSIONS AND PERSPECTIVES

This thesis has addressed the application of tensor-based signal processing in wireless communication systems. We have shown that by properly exploiting the multidimensional structure of the signals, efficient algorithms to improve the overall performance can be employed. More specifically, our contributions are tensor-based methods applied to the following research areas:

- Tensor algebra;
- MIMO-OFDM system operating under the presence of phase-noise impairments;
- Control signaling overhead reduction for MIMO IRS-assisted systems.

In tensor algebra, we have proposed a new tensor operator, namely selective Kronecker product (SKP). The SKP operator is a flexible Kronecker operator used to combine or spread specific in tensor products. We have shown its application in Chapter 4, where its used to derive the tensor-based received data signal model.

In MIMO-OFDM systems we have proposed a tensor-based receiver taking into account phase-noise impairments causing ICI. In detail, we have proposed a two-stage tensor-based receiver, where in the first stage, the received signal at the pilots subcarriers is modelled as a PARAFAC tensor. This tensor-based approach, allowed us to develop two algorithms to jointly estimate the channel and the phase-noise impairments. The proposed algorithms are based on iterative (BALS) and closed-form (LSKRF) solutions, and they show that, by separating the phase-noise impairments from the channel gains, the data estimation process is improved, where the LSKRF algorithm being preferable than the BALS algorithm, when the number of antennas at the received side increases. In the second stage, thanks to the proposed SKP operator, a structure Tucker model is derived for the received data signal. Based on this modeling, we proposed a ZF filter, namely ZFSKP, which is capable of estimating the transmitted symbols at all-at-once, and compared to the competitors matrix-based schemes, the proposed receiver efficiently estimates the transmitted symbols in the presence of a high ICI.

Finally, we have derived a tensor-based method to reduce the feedback overhead in IRS-assisted systems. We show that thanks to the imposed tensor-based structure on the optimized IRS phase-shift vector, the number of phase-shifts that are required to be conveyed to the IRS controller are drastically reduced. More specifically, we proposed a low-rank approximation of the *tensorized* version of the IRS phase-shift vector. This factorization depends on pre-determined parameters, such as the number of factors, the number of components, the size of each factor, and the quantization resolution. To this end, we proposed two tensor-based models, namely PARAFAC-IRS and Tucker-IRS. We have shown that, due to the array separability, when the Rician factor of the involved channels increases, the factorization achieves a close performance of the state-of-the-art model, with an extraordinary reduction of the cost for the IRS phase-shifts

feedback. In addition, based on the communication channels conditions, the Tucker-IRS model is preferable in the NLOS scenarios, while the PARAFAC-IRS model is the best option for scenarios with strong LOS components, in terms of SE and feedback overhead cost. Also, we have investigated the physical implications of the factorization parameters, where we have shown a trade-off between feedback cost and SE.

6.1 Perspectives

In the following, we list some perspectives from this thesis

- One perspective in the context of tensor algebra is a complete study of the proposed SKP operator. The starting point would be a generalization of the properties of the matrix-based Kronecker product to the tensor-based Kronecker product. For example, its relationship with the tensor contraction operator.
- A new tensor operator based on the generalization of the matrix Khatri-Rao product. Since the matrix Khatri-Rao product is the column-wise Kronecker product, one possible definition for the tensor Khatri-Rao product would be the tensor slice-wise (or mode-wise) Kronecker product. This operator can be applied in the design of generalized tensor codes.
- Based on the system model in Chapter 4, one perspective is to add an IRS to enhance the system performance. New strategies for the IRS passive beamforming should be developed. One idea is to use the passive beamforming of the IRS to mitigate the effects of phase-noise, CFO, and possible IRS hardware defects.
- Perspectives of Chapter 5 include a study of the impact of the proposed tensor-based models for reducing the IRS phase-shift feedback in a multi-user and multicell scenario. The idea is to identify use cases to implement the proposed factorization in 5G and 6G networks. One possible study case is to have more frequent user IRS phase-shift feedback, thanks to the proposed overhead-aware tensor-based models.
- Different tensor-based models to model the IRS phase-shift. In this scenario, tensor decompositions, such as the TT, can be used to perform the low-rank approximation of the IRS phase-shifts.

A TIME-TO-FREQUENCY SIGNAL DEVELOPMENT

Here, we show, step by step, how to derive equation (4.4) from (4.1), which is a key property to the tensor model in equation (4.5). The time-domain transmitted symbols are modelled as $s(t) = 1/F \sum_{f=0}^{F-1} S[f] e^{j2\pi \frac{f}{T_s} t}$, with $T_s = 1/d_{\mathrm{F}}$ being the symbol period and d_{F} the subcarrier spacing in Hertz. For notation simplicity, let us consider a scalar (single-antenna) version of the received signal, where $M_R = M_T = K = L_P = 1$ is assumed. The same derivation applies to the multiple-antenna case by introducing the transmit and receive antenna indices, without changing the developments. In order to simplify the notation, let us consider $c(t) = e^{j\phi^{[\mathrm{t}]}(t)} s(t)$, where $\phi^{[\mathrm{t}]}$ is the phase-noise term at the transmitter side. Assuming $t = \left(\frac{nT_s}{F} - \tau_l\right)$, the discrete-time received signal can be written as

$$
\begin{aligned}
y[n] &= \sum_{l=0}^{L-1} e^{j\phi^{[\mathrm{r}]}[n]} \bar{h}[l] c\left(\frac{nT_s}{F} - \tau_l\right) \\
&= \sum_{l=0}^{L-1} e^{j\phi^{[\mathrm{r}]}[n]} \bar{h}[l] \frac{1}{F} \sum_{p=0}^{F-1} C[p] e^{j2\pi \frac{p}{T_s}\left(\frac{nT_s}{F} - \tau_l\right)} \\
&= \frac{1}{F} \sum_{l=0}^{L-1} \sum_{p=0}^{F-1} e^{j\phi^{[\mathrm{r}]}[n]} \bar{h}[l] e^{-j2\pi p d_{\mathrm{F}} \tau_l} C[p] e^{j2\pi pn/F} \\
&= \frac{1}{F} \sum_{p=0}^{F-1} e^{j\phi^{[\mathrm{r}]}[n]} H[p] C[p] e^{j2\pi pn/F}.
\end{aligned} \tag{A.1}
$$

Applying the DFT, we have

$$Y[f] = \sum_{n=0}^{F-1} y[n] e^{-j2\pi fn/F} \tag{A.2}$$

$$= \sum_{n=0}^{F-1} \left(\frac{1}{F} \sum_{p=0}^{F-1} e^{j\phi^{[\mathrm{r}]}[n]} H[p] C[p] e^{j2\pi pn/F} \right) e^{-j2\pi fn/F} \tag{A.3}$$

$$= \sum_{n=0}^{F-1} \sum_{p=0}^{F-1} \frac{1}{F} e^{j\phi^{[\mathrm{r}]}[n]} e^{j2\pi pn/F} e^{-j2\pi fn/F} H[p] \sum_{q=0}^{F-1} \Phi^{[\mathrm{t}]}[p-q] S[q] \tag{A.4}$$

$$= \sum_{n=0}^{F-1} \sum_{p=0}^{F-1} \frac{1}{F} e^{j\phi^{[\mathrm{r}]}[n]} e^{-j2\pi (f-p)n/F} H[p] \sum_{q=0}^{F-1} \Phi^{[\mathrm{t}]}[p-q] S[q] \tag{A.5}$$

$$= \sum_{p=0}^{F-1} \Phi^{[\mathrm{r}]}[f-p] H[p] \sum_{q=0}^{F-1} \Phi^{[\mathrm{t}]}[p-q] S[q] \tag{A.6}$$

$$= \Phi^{[\mathrm{r}]}[0] H[f] \Phi^{[\mathrm{t}]}[0] S[f] + \sum_{p=0, p\neq f}^{F-1} \Phi^{[\mathrm{r}]}[f-p] H[p] \sum_{q=0, q\neq f}^{F-1} \Phi^{[t]}[p-q] S[q]$$

$$= \Phi^{[\mathrm{r}]}[0] H[f] \Phi^{[\mathrm{t}]}[0] S[f] + G[f] \tag{A.7}$$

where $G[f]$ is the ICI term. To derive equation (A.4) from (A.3), we note that

$$\begin{aligned} C[p] &= \sum_{n=0}^{F-1} e^{j\phi^{[\mathrm{t}]}[n]} s[n] e^{-j2\pi pn/F} \\ &= \sum_{n=0}^{F-1} e^{j\phi^{[\mathrm{t}]}[n]} \frac{1}{F} \sum_{q=0}^{F-1} S[q] e^{-j2\pi (p-q)n/F} \\ &= \sum_{q=0}^{F-1} \sum_{n=0}^{F-1} \frac{1}{F} e^{j\phi^{[\mathrm{t}]}[n]} e^{-j2\pi (p-q)n/F} S[q] \\ &= \sum_{q=0}^{F-1} \Phi^{[\mathrm{t}]}[p-q] S[q]. \end{aligned}$$

Applying the combiner $\boldsymbol{W} \in \mathbb{C}^{M_R \times M_R}$, and taking into account the AWGN tensor at the receiver $\mathcal{V}$, the received signal at the k-th block and f-th subcarrier in matrix slice notation can be written as

$$\mathcal{Y}_{..kf} = \boldsymbol{W} \mathrm{diag}_k \left(\Phi^{[\mathrm{r}]}[0] \right) \mathcal{H}_{..f} \mathrm{diag}_k \left(\Phi^{[\mathrm{t}]}[0] \right) \mathcal{S}^{\mathrm{T}}_{..f} + \boldsymbol{W} \mathcal{G}_{..kf} + \boldsymbol{W} \mathcal{V}_{..kf}, \tag{A.8}$$

where $\Phi^{[\mathrm{x}]}[0] \in \mathbb{C}^{K \times M_X}$, for $\mathrm{x} \in \{\mathrm{r}, \mathrm{t}\}$, is given by

$$\Phi^{[\mathrm{x}]}[0] = \begin{bmatrix} \Phi^{(\mathrm{x})}_{1,1}[0] & \dots & \Phi^{(\mathrm{x})}_{1,M_X}[0] \\ \vdots & \ddots & \vdots \\ \Phi^{(\mathrm{x})}_{K,1}[0] & \dots & \Phi^{(\mathrm{x})}_{K,M_X}[0] \end{bmatrix} \tag{A.9}$$

B DERIVATION OF THE ICI POWER

As in many works [121, 129], the ICI can be approximated as a Gaussian random variable with zero mean and variance σ^2_{ICI}, i.e., $G[f] \sim \mathcal{CN}(0, \sigma^2_{\text{ICI}})$. Considering the ICI term in equation (A.7), we have $\sigma^2_{\text{ICI}} = \mathbb{E}\left[G[f]G[f]^*\right]$, which can be computed as

$$\sigma^2_{\text{ICI}} = \mathbb{E}\left[\left|\sum_{p=0,p\neq f}^{F-1} \Phi^{[\text{r}]}[f-p]H[p] \sum_{q=0,q\neq f}^{F-1} \Phi^{[\text{t}]}[p-q]S[q]\right|^2\right].$$

Assuming $\mathbb{E}\left[S[q]S[q]^*\right] = 1$ and $\mathbb{E}\left[H[p]H[p]^*\right] = 1$, we get

$$\sigma^2_{\text{ICI}} = \mathbb{E}\left[\left|\sum_{p=0,p\neq f}^{F-1} \Phi^{[\text{r}]}[f-p] \sum_{q=0,q\neq f}^{F-1} \Phi^{[\text{t}]}[p-q]\right|^2\right]. \tag{B.1}$$

It is important to note that, when $q \neq p$, $\mathbb{E}\left[\left|\Phi^{[\text{r}]}[f-p]\Phi^{[\text{t}]}[p-q]\right|^2\right] \approx 0$, since the product between the non-DC terms (i.e., $p \neq f$ and $q \neq f$) of the phase-noise at the transmitter and the receiver is very small, even for $\sigma^2_{\phi^{[\text{t}]}} = \sigma^2_{\phi^{[\text{r}]}} = 5 \cdot 10^{-3}$. We can rewrite (B.1) as

$$\sigma^2_{\text{ICI}} \approx \mathbb{E}\left[\left|\sum_{p=0,p\neq f}^{F-1} \Phi^{[\text{r}]}[f-p]\Phi^{[\text{t}]}[0]\right|^2\right] \tag{B.2}$$

$$\approx \left(1 - \mathbb{E}\left[\left|\Phi^{[\text{r}]}[0]\right|^2\right]\right)\mathbb{E}\left[\left|\Phi^{[\text{t}]}[0]\right|^2\right]. \tag{B.3}$$

Adopting the same approach as in [126], in our model the ICI power can be calculated as

$$\sigma^2_{\text{ICI}} \approx \left(\text{trace}\{\boldsymbol{R}^{[\text{r}]}_{\Phi\Phi}\} - \boldsymbol{R}^{[\text{r}]}_{\Phi\Phi}(0,0)\right)\boldsymbol{R}^{[\text{t}]}_{\Phi\Phi}(0,0), \tag{B.4}$$

where $\boldsymbol{R}^{[\text{x}]}_{\Phi\Phi} \in \mathbb{C}^{F\times F}$, $\text{x} \in \{\text{r},\text{t}\}$, is given by

$$\begin{aligned}
\boldsymbol{R}^{[\text{x}]}_{\Phi\Phi}(i,m) &= E\left[\Phi^{[\text{x}]}[i]\Phi^{[\text{x}]*}[m]\right] \\
&= \frac{1}{F^2}E\left[\sum_{k=0}^{F-1}\sum_{l=0}^{F-1} e^{j(\phi^{[\text{x}]}[k]-\phi^{[\text{x}]}[l])}e^{-j2\pi(ik-ml)/F}\right] \\
&= \frac{1}{F^2}\sum_{k=0}^{F-1}\sum_{l=0}^{F-1} E\left[e^{j(\Delta\phi^{[\text{x}]}[k,l])}\right]e^{-j2\pi(ik-ml)/F},
\end{aligned} \tag{B.5}$$

with $i,m = \{0\ldots F-1\}$. Note that $\text{trace}\left(\boldsymbol{R}^{[\text{x}]}_{\Phi\Phi}\right) = 1$.

REFERENCES

1 BENGUA, J. A. et al. Efficient tensor completion for color image and video recovery: Low-rank tensor train. **IEEE Transactions on Image Processing**, IEEE, v. 26, n. 5, p. 2466–2479, 2017.

2 MENG, S.; HUANG, L.-T.; WANG, W.-Q. Tensor decomposition and PCA jointed algorithm for hyperspectral image denoising. **IEEE Geoscience and Remote Sensing Letters**, IEEE, v. 13, n. 7, p. 897–901, 2016.

3 CAI, J.; CAO, Z.; ZHANG, L. Learning a single tucker decomposition network for lossy image compression with multiple bits-per-pixel rates. **IEEE Transactions on Image Processing**, IEEE, v. 29, p. 3612–3625, 2020.

4 BAI, X. et al. Nonlocal similarity based nonnegative tucker decomposition for hyperspectral image denoising. **IEEE Journal of Selected Topics in Applied Earth Observations and Remote Sensing**, IEEE, v. 11, n. 3, p. 701–712, 2018.

5 ZHOU, G. et al. Linked component analysis from matrices to high-order tensors: Applications to biomedical data. **Proceedings of the IEEE**, IEEE, v. 104, n. 2, p. 310–331, 2016.

6 XIAO, L. et al. Online MECG compression based on incremental tensor decomposition for wearable devices. **IEEE Journal of Biomedical and Health Informatics**, IEEE, v. 25, n. 4, p. 1041–1051, 2020.

7 ZHANG, Y. et al. Tensor-based dictionary learning for spectral CT reconstruction. **IEEE transactions on medical imaging**, IEEE, v. 36, n. 1, p. 142–154, 2016.

8 BECKER, H.; COMON, P.; ALBERA, L. Tensor-based preprocessing of combined EEG/MEG data. In: 2012 PROCEEDINGS OF THE 20TH EUROPEAN SIGNAL PROCESSING CONFERENCE (EUSIPCO), 2012 2012, 2012 Proceedings of the 20th European Signal Processing Conference (EUSIPCO). **Proceedings [...]** [S.l.: s.n.], 2012. IEEE, p. 275–279.

9 SIDIROPOULOS, N. D.; BRO, R.; GIANNAKIS, G. B. Parallel factor analysis in sensor array processing. **IEEE transactions on Signal Processing**, IEEE, v. 48, n. 8, p. 2377–2388, 2000.

10 THAKRE, A. et al. Tensor-based spatial smoothing (TB-SS) using multiple snapshots. **IEEE Transactions on Signal Processing**, IEEE, v. 58, n. 5, p. 2715–2728, 2010.

11 CHEN, H. et al. Tensor decompositions in wireless communications and MIMO radar. **IEEE Journal of Selected Topics in Signal Processing**, IEEE, v. 15, n. 3, p. 438–453, 2021.

12 QIAN, C. et al. Tensor-based channel estimation for dual-polarized massive MIMO systems. **IEEE Transactions on Signal Processing**, IEEE, v. 66, n. 24, p. 6390–6403, 2018.

13 LIU, X. et al. A low-rank approximation-based transductive support tensor machine for semisupervised classification. **IEEE Transactions on Image Processing**, IEEE, v. 24, n. 6, p. 1825–1838, 2015.

14 JI, Y. et al. A survey on tensor techniques and applications in machine learning. **IEEE Access**, IEEE, v. 7, p. 162950–162990, 2019.

15 SINGH, A. et al. Deep-learning-based SDN model for Internet of Things: An incremental tensor train approach. **IEEE Internet of Things Journal**, IEEE, v. 7, n. 7, p. 6302–6311, 2019.

16 LUO, L.; XIE, L.; SU, H. Deep learning with tensor factorization layers for sequential fault diagnosis and industrial process monitoring. **IEEE Access**, IEEE, v. 8, p. 105494–105506, 2020.

17 SIDIROPOULOS, N. D.; GIANNAKIS, G. B.; BRO, R. Blind PARAFAC receivers for DS-CDMA systems. **IEEE Transactions on Signal Processing**, IEEE, v. 48, n. 3, p. 810–823, 2000.

18 ALMEIDA, A. L. F. de; FAVIER, G.; MOTA, J. C. M. A Constrained Factor Decomposition with Application to MIMO Antenna Systems. **IEEE Trans. Signal Process.**, IEEE, v. 56, n. 6, p. 2429–2442, 2008.

19 ALMEIDA, A. L. F. de; FAVIER, G. Double Khatri–Rao Space-Time-Frequency Coding Using Semi-Blind PARAFAC Based Receiver. **IEEE Signal Process. Lett.**, IEEE, v. 20, n. 5, p. 471–474, 2013.

20 ROEMER, F.; HAARDT, M. Tensor-based channel estimation and iterative refinements for two-way relaying with multiple antennas and spatial reuse. **IEEE Transactions on Signal Processing**, IEEE, v. 58, n. 11, p. 5720–5735, 2010.

21 SOKAL, B. et al. Tensor-Based Receiver for Joint Channel, Data, and Phase-Noise Estimation in MIMO-OFDM Systems. **IEEE Journal of Selected Topics in Signal Processing**, IEEE, v. 15, n. 3, p. 803–815, 2021.

22 ARAÚJO, G. T. de; ALMEIDA, A. L. F. de; BOYER, R. Channel Estimation for Intelligent Reflecting Surface Assisted MIMO Systems: A Tensor Modeling Approach. **IEEE J. Sel. Topics Signal Process.**, v. 15, n. 3, p. 789–802, Feb. 2021. DOI: 10.1109/JSTSP.2021.3061274.

23 KOLDA, T. G.; BADER, B. W. Tensor decompositions and applications. **SIAM review**, SIAM, v. 51, n. 3, p. 455–500, Aug. 2009.

24 KRUSKAL, J. B. Three-way Arrays: Rank and Uniqueness of Trilinear Decompositions, with Application to Arithmetic Complexity and Statistics. **Linear algebra and its applications**, Elsevier, v. 18, n. 2, p. 95–138, 1977.

25 HARSHMAN, R. A. et al. Foundations of the PARAFAC procedure: Models and conditions for an" explanatory" multimodal factor analysis. **UCLA working papes in Phonetics**, v. 16, p. 1–84, 1970.

26 TUCKER, L. R. Some Mathematical Notes on Three-mode Factor Analysis. **Psychometrika**, Springer, v. 31, n. 3, p. 279–311, Sept. 1966.

27 FAVIER, G. et al. Tensor space-time (TST) coding for MIMO wireless communication systems. **Signal Processing**, Elsevier, v. 92, n. 4, p. 1079–1092, 2012.

28 FAVIER, G.; FERNANDES, C. A. R.; ALMEIDA, A. L. F. de. Nested Tucker Tensor Decomposition with Application to MIMO Relay Systems Using Tensor Space–Time Coding (TSTC). **Signal Processing**, Elsevier, v. 128, p. 318–331, 2016.

29 XIMENES, L. R.; FAVIER, G.; ALMEIDA, A. L. F. de. Semi-Blind Receivers for Non-Regenerative Cooperative MIMO Communications Based on Nested PARAFAC Modeling. **IEEE Trans. Signal Process.**, IEEE, v. 63, n. 18, p. 4985–4998, 2015.

30 OSELEDETS, I. V. Tensor-Train Decomposition. **SIAM Journal on Scientific Computing**, SIAM, v. 33, n. 5, p. 2295–2317, 2011.

31 ZNIYED, Y. et al. High-order CPD estimation with dimensionality reduction using a tensor train model. In: 2018 26TH EUROPEAN SIGNAL PROCESSING CONFERENCE (EUSIPCO), 2018 2018, 2018 26th European Signal Processing Conference (EUSIPCO). **Proceedings [...]** [S.l.: s.n.], 2018. IEEE, p. 2613–2617.

32 _____. Tensor-train modeling for MIMO-OFDM tensor coding-and-forwarding relay systems. In: 2019 27TH EUROPEAN SIGNAL PROCESSING CONFERENCE (EUSIPCO), 2019 2019, 2019 27th European Signal Processing Conference (EUSIPCO). **Proceedings [...]** [S.l.: s.n.], 2019. IEEE, p. 1–5.

33 ZHANG, J. et al. Designing tensor-train deep neural networks for time-varying MIMO channel estimation. **IEEE Journal of Selected Topics in Signal Processing**, IEEE, v. 15, n. 3, p. 759–773, 2021.

34 ZOU, C.; YANG, F. Deep learning approach based on tensor-train for sparse signal recovery. **IEEE Access**, IEEE, v. 7, p. 34753–34761, 2019.

35 NASKOVSKA, K.; HAARDT, M.; ALMEIDA, A. L. F. de. Generalized tensor contractions for an improved receiver design in MIMO-OFDM systems. In: PROC. IEEE INTERNATIONAL CONFERENCE ON ACOUSTICS, SPEECH AND SIGNAL PROCESSING (ICASSP), 2018 2018, Proc. IEEE International Conference on Acoustics, Speech and Signal Processing (ICASSP). **Proceedings [...]** [S.l.: s.n.], 2018. P. 3186–3190.

36 ARAÚJO, D. C. et al. Tensor-based channel estimation for massive MIMO-OFDM systems. **IEEE Access**, IEEE, v. 7, p. 42133–42147, 2019.

37 ZHOU, Z. et al. Low-rank tensor decomposition-aided channel estimation for millimeter wave MIMO-OFDM systems. **IEEE J. Sel. Areas Commun.**, IEEE, v. 35, n. 7, p. 1524–1538, 2017.

38 NASKOVSKA, K.; HAARDT, M.; ALMEIDA, A. L. de. Generalized tensor contraction with application to Khatri-Rao coded MIMO OFDM systems. In: PROC. IEEE 7TH INTERNATIONAL WORKSHOP ON COMPUTATIONAL ADVANCES IN MULTI-SENSOR ADAPTIVE PROCESSING (CAMSAP), 2017 2017, Proc. IEEE 7th International Workshop on Computational Advances in Multi-Sensor Adaptive Processing (CAMSAP). **Proceedings [...]** [S.l.: s.n.], 2017. P. 1–5.

39 CICHOCKI, A. Era of big data processing: A new approach via tensor networks and tensor decompositions. **arXiv preprint arXiv:1403.2048**, 2014.

40 ROEMER, F. **Advanced algebraic concepts for efficient multi-channel signal processing**. 2012. PhD thesis – Ilmenau University of Technology, Germany.

41 DE LATHAUWER, L.; DE MOOR, B.; VANDEWALLE, J. On the best rank-1 and rank-(r 1, r 2,..., rn) approximation of higher-order tensors. **SIAM journal on Matrix Analysis and Applications**, SIAM, v. 21, n. 4, p. 1324–1342, Mar. 2000.

42 SIDIROPOULOS, N. D.; BRO, R. On the Uniqueness of Multilinear Decomposition of N-way Arrays. **Journal of Chemometrics**, v. 14, n. 3, 2000. ISSN 1099-128X.

43 BRO, R. Multi-way analysis in the food industry-models, algorithms, and applications. In: MRI, EPG AND EMA," PROC ICSLP 2000, 1998 1998, MRI, EPG and EMA," Proc ICSLP 2000. **Proceedings [...]** [S.l.: s.n.], 1998. Citeseer.

44 SMILDE, A.; BRO, R.; GELADI, P. **Multi-way analysis: applications in the chemical sciences**. [S.l.]: John Wiley & Sons, 2005.

45 COMON, P.; LUCIANI, X.; DE ALMEIDA, A. L. Tensor decompositions, alternating least squares and other tales. **Journal of Chemometrics: A Journal of the Chemometrics Society**, Wiley Online Library, v. 23, n. 7-8, p. 393–405, 2009.

46 DE LATHAUWER, L.; DE MOOR, B.; VANDEWALLE, J. A multilinear singular value decomposition. **SIAM journal on Matrix Analysis and Applications**, SIAM, v. 21, n. 4, p. 1253–1278, 2000.

47 VAN LOAN, C.; PITSIANIS, N. **Approximation with Kronecker Products**. [S.l.], 1992.

48 ROEMER, F.; HAARDT, M. Tensor-based channel estimation and iterative refinements for two-way relaying with multiple antennas and spatial reuse. **IEEE Trans. Signal Process.**, IEEE, v. 58, n. 11, p. 5720–5735, 2010.

49 ABEYWICKRAMA, S. et al. Intelligent Reflecting Surface: Practical Phase Shift Model and Beamforming Optimization. **IEEE Trans. Commun.**, v. 68, n. 9, p. 5849–5863, 2020. DOI: 10.1109/TCOMM.2020.3001125.

50 WU, Q. et al. Intelligent Reflecting Surface Aided Wireless Communications: A Tutorial. **IEEE Trans. Commun.**, p. 1–1, May 2021. DOI: 10.1109/TCOMM.2021.3051897.

51 GONG, S. et al. Toward Smart Wireless Communications via Intelligent Reflecting Surfaces: A Contemporary Survey. **IEEE Commun. Surveys Tuts.**, v. 22, n. 4, p. 2283–2314, June 2020. DOI: 10.1109/COMST.2020.3004197.

52 JIAN, M. et al. Reconfigurable intelligent surfaces for wireless communications: Overview of hardware designs, channel models, and estimation techniques. **Intelligent and Converged Networks**, v. 3, n. 1, p. 1–32, 2022.

53 ZHI, K. et al. Power Scaling Law Analysis and Phase Shift Optimization of RIS-Aided Massive MIMO Systems With Statistical CSI. **IEEE Transactions on Communications**, v. 70, n. 5, p. 3558–3574, 2022. DOI: 10.1109/TCOMM.2022.3162580.

54 BJÖRNSON, E.; ÖZDOGAN, Ö.; LARSSON, E. G. Intelligent reflecting surface versus decode-and-forward: How large surfaces are needed to beat relaying? **IEEE Wireless Commun. Lett.**, IEEE, v. 9, n. 2, p. 244–248, Oct. 2019.

55 KHALEEL, A.; BASAR, E. A novel NOMA solution with RIS partitioning. **IEEE J. Sel. Topics Signal Process**, IEEE, Nov. 2021.

56 YANG, Z. et al. Machine Learning for User Partitioning and Phase Shifters Design in RIS-Aided NOMA Networks. **IEEE Transactions on Communications**, v. 69, n. 11, p. 7414–7428, 2021. DOI: 10.1109/TCOMM.2021.3100866.

57 SARP, S.; TANG, H.; ZHAO, Y. Use of Intelligent Reflecting Surfaces For and Against Wireless Communication Security. In: 2021 IEEE 4TH 5G WORLD FORUM (5GWF), 2021 2021, 2021 IEEE 4th 5G World Forum (5GWF). **Proceedings [...]** [S.l.: s.n.], 2021. P. 374–377. DOI: 10.1109/5GWF52925.2021.00072.

58 TANG, Z. et al. A Novel Design of RIS for Enhancing the Physical Layer Security for RIS-Aided NOMA Networks. **IEEE Wireless Communications Letters**, v. 10, n. 11, p. 2398–2401, 2021. DOI: 10.1109/LWC.2021.3101806.

59 TANG, Z. et al. Physical Layer Security of Intelligent Reflective Surface Aided NOMA Networks. **IEEE Transactions on Vehicular Technology**, p. 1–1, 2022. DOI: 10.1109/TVT.2022.3168392.

60 YILDIRIM, I. et al. Hybrid RIS-Empowered Reflection and Decode-and-Forward Relaying for Coverage Extension. **IEEE Communications Letters**, v. 25, n. 5, p. 1692–1696, 2021. DOI: 10.1109/LCOMM.2021.3054819.

61 WANG, M. et al. On the Achievable Capacity of Cooperative NOMA Networks: RIS or Relay? **IEEE Wireless Communications Letters**, p. 1–1, 2022. DOI: 10.1109/LWC.2022.3169806.

62 BASAR, E. et al. Wireless communications through reconfigurable intelligent surfaces. **IEEE Access**, IEEE, v. 7, p. 116753–116773, Aug. 2019.

63 BASAR, E. Reconfigurable Intelligent Surface-Based Index Modulation: A New Beyond MIMO Paradigm for 6G. **IEEE Trans. Commun.**, v. 68, n. 5, p. 3187–3196, Feb. 2020.

64 TAHA, A.; ALRABEIAH, M.; ALKHATEEB, A. Enabling Large Intelligent Surfaces With Compressive Sensing and Deep Learning. **IEEE Access**, v. 9, p. 44304–44321, 2021. DOI: 10.1109/ACCESS.2021.3064073.

65 KHOSHAFA, M. H. et al. Active reconfigurable intelligent surfaces-aided wireless communication system. **IEEE Wireless Commun. Lett.**, IEEE, v. 25, n. 11, p. 3699–3703, Sept. 2021.

66 ALEXANDROPOULOS, G. C.; VLACHOS, E. A hardware architecture for reconfigurable intelligent surfaces with minimal active elements for explicit channel estimation. In: PROC. IN ICASSP 2020, May 2020, Barcelona, Spain. **Proceedings [...]** Barcelona, Spain: [s.n.], May 2020. IEEE, p. 9175–9179.

67 _____. A Hardware Architecture For Reconfigurable Intelligent Surfaces with Minimal Active Elements for Explicit Channel Estimation. In: ICASSP 2020 - 2020 IEEE INTERNATIONAL CONFERENCE ON ACOUSTICS, SPEECH AND SIGNAL PROCESSING (ICASSP), 2020 2020, ICASSP 2020 - 2020 IEEE International Conference on Acoustics, Speech and Signal Processing (ICASSP). **Proceedings [...]** [S.l.: s.n.], 2020. P. 9175–9179. DOI: 10.1109/ICASSP40776.2020.9053976.

68 HUANG, C. et al. Holographic MIMO surfaces for 6G wireless networks: Opportunities, challenges, and trends. **IEEE Wireless Commun.**, IEEE, v. 27, n. 5, p. 118–125, 2020.

69 DARDARI, D.; DECARLI, N. Holographic Communication Using Intelligent Surfaces. **IEEE Communications Magazine**, v. 59, n. 6, p. 35–41, 2021. DOI: 10.1109/MCOM.001.2001156.

70 PIZZO, A.; MARZETTA, T. L.; SANGUINETTI, L. Spatially-Stationary Model for Holographic MIMO Small-Scale Fading. **IEEE Journal on Selected Areas in Communications**, v. 38, n. 9, p. 1964–1979, 2020. DOI: 10.1109/JSAC.2020.3000877.

71 BJÖRNSON, Ö. T. D. E.; SANGUINETTI, L. Channel Modeling and Channel Estimation for Holographic Massive MIMO With Planar Arrays. **IEEE Wireless Communications Letters**, v. 11, n. 5, p. 997–1001, 2022. DOI: 10.1109/LWC.2022.3152600.

72 WAN, Z. et al. Terahertz massive MIMO with holographic reconfigurable intelligent surfaces. **IEEE Trans. Commun.**, IEEE, v. 69, n. 7, p. 4732–4750, 2021.

73 DASH, S. et al. Active Control of THz Waves in Wireless Environments using Graphene-based RIS. **IEEE Trans. Antennas Propag.**, IEEE, 2022.

74 ALAMZADEH, I. et al. A reconfigurable intelligent surface with integrated sensing capability. **Scientific reports**, Nature Publishing Group, v. 11, n. 1, p. 1–10, 2021.

75 MU, X. et al. Simultaneously transmitting and reflecting (STAR) RIS aided wireless communications. **IEEE Transactions on Wireless Communications**, IEEE, 2021.

76 XU, J. et al. STAR-RISs: Simultaneous transmitting and reflecting reconfigurable intelligent surfaces. **IEEE Communications Letters**, IEEE, v. 25, n. 9, p. 3134–3138, 2021.

77 LIU, Y. et al. STAR: Simultaneous Transmission and Reflection for 360º; Coverage by Intelligent Surfaces. **IEEE Wireless Communications**, v. 28, n. 6, p. 102–109, 2021. DOI: 10.1109/MWC.001.2100191.

78 ZHANG, H. et al. Intelligent omni-surfaces for full-dimensional wireless communications: Principles, technology, and implementation. **IEEE Communications Magazine**, IEEE, v. 60, n. 2, p. 39–45, 2022.

79 ZHANG, S. et al. Intelligent omni-surfaces: Ubiquitous wireless transmission by reflective-refractive metasurfaces. **IEEE Transactions on Wireless Communications**, IEEE, 2021.

80 POGAKU, A. C. et al. UAV-Assisted RIS for Future Wireless Communications: A Survey on Optimization and Performance Analysis. **IEEE Access**, v. 10, p. 16320–16336, 2022. DOI: 10.1109/ACCESS.2022.3149054.

81 REN, H. et al. Energy Minimization in RIS-Assisted UAV-Enabled Wireless Power Transfer Systems. **IEEE Internet of Things Journal**, p. 1–1, 2022. DOI: 10.1109/JIOT.2022.3150178.

82 ZHANG, X. et al. IRS Empowered UAV Wireless Communication with Resource Allocation, Reflecting Design and Trajectory Optimization. **IEEE Transactions on Wireless Communications**, p. 1–1, 2022. DOI: 10.1109/TWC.2022.3162704.

83 AGRAWAL, N. et al. Finite Block Length Analysis of RIS-Assisted UAV-Based Multiuser IoT Communication System With Non-Linear EH. **IEEE Transactions on Communications**, v. 70, n. 5, p. 3542–3557, 2022. DOI: 10.1109/TCOMM.2022.3162249.

84 RANJHA, A.; KADDOUM, G. URLLC Facilitated by Mobile UAV Relay and RIS: A Joint Design of Passive Beamforming, Blocklength, and UAV Positioning. **IEEE Internet of Things Journal**, v. 8, n. 6, p. 4618–4627, 2021. DOI: 10.1109/JIOT.2020.3027149.

85 LIU, X. et al. Throughput Maximization for RIS-UAV Relaying Communications. **IEEE Transactions on Intelligent Transportation Systems**, p. 1–6, 2022. DOI: 10.1109/TITS.2022.3161698.

86 CAI, W. et al. IRS-assisted Multi-cell Multi-band Systems: Practical Reflection Model and Joint Beamforming Design. **IEEE Transactions on Communications**, IEEE, 2022.

87 NI, W. et al. Resource allocation for multi-cell IRS-aided NOMA networks. **IEEE Transactions on Wireless Communications**, IEEE, v. 20, n. 7, p. 4253–4268, 2021.

88 QIU, J. et al. Joint Beamforming for IRS-Aided Multi-Cell MISO System: Sum Rate Maximization and SINR Balancing. **IEEE Transactions on Wireless Communications**, IEEE, 2022.

89 XIE, H.; XU, J.; LIU, Y.-F. Max-Min Fairness in IRS-Aided Multi-Cell MISO Systems With Joint Transmit and Reflective Beamforming. **IEEE Transactions on Wireless Communications**, v. 20, n. 2, p. 1379–1393, 2021. DOI: 10.1109/TWC.2020.3033332.

90 5G AMERICAS. **The 5G Evolution: 3GPP Releases 16-17**. [S.l.], Jan. 2020. Available from: <%7Bhttps://www.5gamericas.org/wp-content/uploads/2020/01/5G-Evolution-3GPP-R16-R17-FINAL.pdf%7D>.

91 3GPP. **TR 38.874 - Study on Integrated Access and Backhaul**. [S.l.], Dez. 2018.

92 _____. **TS 38.300 - NR and NG-RAN Overall Description**. [S.l.], Dez. 2021.

93 FIORE, P. et al. Boosting 5G mm-Wave IAB Reliability with Reconfigurable Intelligent Surfaces. In: 2022 IEEE WIRELESS COMMUNICATIONS AND NETWORKING CONFERENCE (WCNC), 2022 2022, 2022 IEEE Wireless Communications and Networking Conference (WCNC). **Proceedings [...]** [S.l.: s.n.], 2022. P. 758–763. DOI: 10.1109/WCNC51071.2022.9771934.

94 DIAMANTI, M. et al. The prospect of reconfigurable intelligent surfaces in integrated access and backhaul networks. **IEEE Transactions on Green Communications and Networking**, IEEE, v. 6, n. 2, p. 859–872, 2021.

95 AL-JARRAH, M. A. et al. Performance analysis of wireless mesh backhauling using intelligent reflecting surfaces. **IEEE Transactions on Wireless Communications**, IEEE, v. 20, n. 6, p. 3597–3610, 2021.

96 NGO, H. Q. et al. Cell-Free Massive MIMO Versus Small Cells. **IEEE Transactions on Wireless Communications**, v. 16, n. 3, p. 1834–1850, 2017. DOI: 10.1109/TWC.2017.2655515.

97 ELHOUSHY, S.; IBRAHIM, M.; HAMOUDA, W. Cell-Free Massive MIMO: A Survey. **IEEE Communications Surveys and Tutorials**, v. 24, n. 1, p. 492–523, 2022. DOI: 10.1109/COMST.2021.3123267.

98 ZHOU, T. et al. Achievable Rate Optimization for Aerial Intelligent Reflecting Surface-Aided Cell-Free Massive MIMO System. **IEEE Access**, v. 9, p. 3828–3837, 2021. DOI: 10.1109/ACCESS.2020.3047450.

99 HUANG, S. et al. Decentralized Beamforming Design for Intelligent Reflecting Surface-Enhanced Cell-Free Networks. **IEEE Wireless Communications Letters**, v. 10, n. 3, p. 673–677, 2021. DOI: 10.1109/LWC.2020.3045884.

100 ZHANG, Y. et al. Beyond Cell-Free MIMO: Energy Efficient Reconfigurable Intelligent Surface Aided Cell-Free MIMO Communications. **IEEE Transactions on Cognitive Communications and Networking**, v. 7, n. 2, p. 412–426, 2021. DOI: 10.1109/TCCN.2021.3058683.

101 ARAÚJO, G. T. de et al. Semi-Blind Joint Channel and Symbol Estimation in IRS-Assisted Multi-User MIMO Networks. **IEEE Wireless Communications Letters**, IEEE, 2022.

102 CHEN, J. et al. Channel Estimation for Reconfigurable Intelligent Surface Aided Multi-User MIMO Systems. [Online]. Available: https://arxiv.org/pdf/1912.03619.pdf. [S.l.], 2019.

103 HU, C. et al. Two-Timescale Channel Estimation for Reconfigurable Intelligent Surface Aided Wireless Communications. **IEEE Trans. Commun.**, v. 69, n. 11, p. 7736–7747, Apr. 2021. DOI: 10.1109/TCOMM.2021.3072729.

104 LI, B. et al. Joint Array Diagnosis and Channel Estimation for RIS-Aided mmWave MIMO System. **IEEE Access**, IEEE, v. 8, p. 193992–194006, 2020.

105 AN, J. et al. Low-complexity channel estimation and passive beamforming for RIS-assisted MIMO systems relying on discrete phase shifts. **IEEE Trans. Commun.**, IEEE, Nov. 2021.

106 WEI, L. et al. Channel Estimation for RIS-Empowered Multi-User MISO Wireless Communications. **IEEE Trans. Commun.**, p. 1–1, Mar. 2021. DOI: 10.1109/TCOMM.2021.3063236.

107 BENICIO, K. B. d. A.; SOKAL, B.; ALMEIDA, A. L. F. de. Channel estimation and joint beamforming design for multi-IRS MIMO systems. In: 2021 BRAZILIAN SYMPOSIUM ON TELECOMMUNICATIONS AND SIGNAL PROCESSING (SBRT), 2021 2021, Fortaleza, Brazil. **Proceedings [...]** Fortaleza, Brazil: [s.n.], 2021. P. 1–5.

108 ARDAH, K. et al. TRICE: A channel estimation framework for RIS-aided millimeter-wave MIMO systems. **IEEE Signal Process. Lett.**, IEEE, v. 28, p. 513–517, Feb. 2021.

109 ZHOU, L. et al. Sparse Channel Estimation for Intelligent Reflecting Surface Assisted Massive MIMO Systems. **IEEE Transactions on Green Communications and Networking**, v. 6, n. 1, p. 208–220, 2022. DOI: 10.1109/TGCN.2022.3146188.

110 WAN, Z.; GAO, Z.; ALOUINI, M.-S. Broadband Channel Estimation for Intelligent Reflecting Surface Aided mmWave Massive MIMO Systems. In: ICC 2020 - 2020 IEEE INTERNATIONAL CONFERENCE ON COMMUNICATIONS (ICC), 2020 2020, ICC 2020 - 2020 IEEE International Conference on Communications (ICC). **Proceedings [...]** [S.l.: s.n.], 2020. P. 1–6. DOI: 10.1109/ICC40277.2020.9149146.

111 WAN, Z. et al. Terahertz Massive MIMO With Holographic Reconfigurable Intelligent Surfaces. **IEEE Transactions on Communications**, v. 69, n. 7, p. 4732–4750, 2021. DOI: 10.1109/TCOMM.2021.3064949.

112 WU, Q.; ZHANG, R. Intelligent Reflecting Surface Enhanced Wireless Network via Joint Active and Passive Beamforming. **IEEE Trans. Wireless Commun**, v. 18, n. 11, p. 5394–5409, 2019. DOI: 10.1109/TWC.2019.2936025.

113 ZHANG, S.; ZHANG, R. Capacity characterization for intelligent reflecting surface aided MIMO communication. **IEEE Journal on Selected Areas in Communications**, IEEE, v. 38, n. 8, p. 1823–1838, 2020.

114 YIGIT, Z.; BASAR, E.; ALTUNBAS, I. Low complexity adaptation for reconfigurable intelligent surface-based MIMO systems. **IEEE Communications Letters**, IEEE, v. 24, n. 12, p. 2946–2950, 2020.

115 JUNG, M. et al. On the optimality of reconfigurable intelligent surfaces (RISs): Passive beamforming, modulation, and resource allocation. **IEEE Transactions on Wireless Communications**, IEEE, v. 20, n. 7, p. 4347–4363, 2021.

116 ZAPPONE, A. et al. Overhead-Aware Design of Reconfigurable Intelligent Surfaces in Smart Radio Environments. **IEEE Trans. Wireless Commun**, v. 20, n. 1, p. 126–141, Sept. 2020. DOI: 10.1109/TWC.2020.3023578.

117 YANG, Y. et al. Intelligent reflecting surface meets OFDM: Protocol design and rate maximization. **IEEE Trans. Commun.**, IEEE, Mar. 2020.

118 CHO, Y. S. et al. **MIMO-OFDM wireless communications with MATLAB**. [S.l.]: John Wiley & Sons, 2010.

119 LEE, T.-J.; KO, Y.-C. Channel estimation and data detection in the presence of phase noise in MIMO-OFDM systems with independent oscillators. **IEEE Access**, IEEE, v. 5, p. 9647–9662, 2017.

120 TAROKH, V.; SESHADRI, N.; CALDERBANK, A. R. Space-time codes for high data rate wireless communication: Performance criterion and code construction. **IEEE Trans. Inf. Theory**, IEEE, v. 44, n. 2, p. 744–765, 1998.

121 HUANG, H.; WANG, W. G.; HE, J. Phase noise and frequency offset compensation in high frequency MIMO-OFDM system. In: PROC. IEEE INTERNATIONAL CONFERENCE ON COMMUNICATIONS (ICC), 2015 2015, Proc. IEEE International Conference on Communications (ICC). **Proceedings [...]** [S.l.: s.n.], 2015. P. 1280–1285.

122 KIM, K. Y. et al. An efficient carrier phase synchronization technique for high-order M-QAM–OFDM. **EEE Trans. Signal Process.**, IEEE, v. 56, n. 8, p. 3789–3794, 2008.

123 NGEBANI, I. et al. Joint channel and phase noise estimation in MIMO-OFDM systems. In: PROC. IEEE RADIO AND ANTENNA DAYS OF THE INDIAN OCEAN (RADIO), 2016 2016, Proc. IEEE Radio and Antenna Days of the Indian Ocean (RADIO). **Proceedings [...]** [S.l.: s.n.], 2016. P. 1–2.

124 ISHAQUE, A.; ASCHEID, G. On the efficient mitigation of phase noise in MIMO-OFDM receivers. In: PROC. INTERNATIONAL SYMPOSIUM ON SIGNALS, SYSTEMS, AND ELECTRONICS (ISSSE), 2012 2012, Proc. International Symposium on Signals, Systems, and Electronics (ISSSE). **Proceedings [...]** [S.l.: s.n.], 2012. IEEE, p. 1–6.

125 HADASCHIK, N. et al. Improving MIMO phase noise estimation by exploiting spatial correlations. In: PROCEEDINGS IN (ICASSP'05). IEEE INTERNATIONAL CONFERENCE ON ACOUSTICS, SPEECH, AND SIGNAL PROCESSING, 2005. 2005 2005, Proceedings in (ICASSP'05). IEEE International Conference on Acoustics, Speech, and Signal Processing, 2005. **Proceedings [...]** [S.l.: s.n.], 2005. v. 3. IEEE, p. iii–833.

126 PETROVIC, D.; RAVE, W.; FETTWEIS, G. Effects of phase noise on OFDM systems with and without PLL: Characterization and compensation. **IEEE Trans. Commun.**, IEEE, v. 55, n. 8, p. 1607–1616, 2007.

127 ZOU, Q.; TARIGHAT, A.; SAYED, A. H. Compensation of phase noise in OFDM wireless systems. **IEEE Trans. Signal Process.**, IEEE, v. 55, n. 11, p. 5407–5424, 2007.

128 MEHRPOUYAN, H. et al. Joint estimation of channel and oscillator phase noise in MIMO systems. **IEEE Trans. Signal Process.**, IEEE, v. 60, n. 9, p. 4790–4807, 2012.

129 ZHANG, Y.-P. et al. Pilot design for phase noise mitigation in millimeter wave MIMO-OFDM systems. In: PROC. IEEE 85TH VEHICULAR TECHNOLOGY CONFERENCE (VTC SPRING), 2017 2017, Proc. IEEE 85th Vehicular Technology Conference (VTC Spring). **Proceedings [...]** [S.l.: s.n.], 2017. P. 1–6.

130 SOKAL, B.; ALMEIDA, A. L. de; HAARDT, M. Semi-blind receivers for MIMO multi-relaying systems via rank-one tensor approximations. **Signal Processing**, Elsevier, v. 166, p. 107254, 2020.

131 FAVIER, G. et al. Tensor space–time (TST) coding for MIMO wireless communication systems. **Signal Processing**, v. 92, n. 4, p. 1079–1092, 2012.

132 LIU, K. et al. Semi-blind receivers for joint symbol and channel estimation in space-time-frequency MIMO-OFDM systems. **IEEE Trans. Signal Process.**, v. 61, n. 21, p. 5444–5457, 2013.

133 ALMEIDA, A. L. F. de; FAVIER, G.; XIMENES, L. R. Space-time-frequency (STF) MIMO communication systems with blind receiver based on a generalized PARATUCK2 model. **IEEE Trans. Signal Process.**, v. 61, n. 8, p. 1895–1909, 2013.

134 ROEMER, F.; HAARDT, M. Tensor-Based Channel Estimation and Iterative Refinements for Two-Way Relaying with Multiple Antennas and Spatial Reuse. **IEEE Trans. Signal Process.**, v. 58, n. 11, p. 5720–5735, Nov. 2010.

135 FERNANDES, C. A. R.; ALMEIDA, A. L. F. de; COSTA, D. B. da. Unified tensor modeling for blind receivers in multiuser uplink cooperative systems. **IEEE Signal Process. Lett**, IEEE, v. 19, n. 5, p. 247–250, 2012.

136 RONG, Y.; KHANDAKER, M. R. A.; XIANG, Y. Channel Estimation of Dual-Hop MIMO Relay System via Parallel Factor Analysis. **IEEE Trans. Wireless Commun**, v. 11, n. 6, p. 2224–2233, June 2012. ISSN 1536-1276. DOI: 10.1109/TWC.2012.032712.111251.

137 ALMEIDA, A. L. F. de; FERNANDES, C. A.; COSTA, D. B. da. Multiuser Detection for Uplink DS-CDMA Amplify-and-Forward Relaying Systems. **IEEE Signal Process. Lett.**, IEEE, v. 20, n. 7, p. 697–700, 2013.

138 ARAÚJO, D. C. et al. Tensor-based channel estimation for massive MIMO-OFDM systems. **IEEE Access**, IEEE, v. 7, p. 42133–42147, 2019.

139 LIN, Y. et al. Tensor-Based Channel Estimation for Millimeter Wave MIMO-OFDM with Dual-Wideband Effects. **IEEE Trans. Commun.**, IEEE, 2020.

140 CHEN, X. et al. Phase noise effect on MIMO-OFDM systems with common and independent oscillators. **Wireless Communications and Mobile Computing**, Hindawi, v. 2017, 2017.

141 WANG, K.; JALLOUL, L.; GOMAA, A. Phase noise compensation using limited reference symbols in 3GPP LTE downlink. **arXiv preprint arXiv:1711.10064**, 2017.

142 SUN, W. et al. Orthogonal tubal rank-1 tensor pursuit for tensor completion. **Signal Processing**, Elsevier, v. 157, p. 213–224, 2019.

143 AHLBERG, J. et al. **The theory of splines and their applications**. [S.l.]: Academic press, 1967.

144 DI RENZO, M. et al. Smart radio environments empowered by reconfigurable intelligent surfaces: How it works, state of research, and the road ahead. **IEEE J. Sel. Areas Commun.**, IEEE, v. 38, n. 11, p. 2450–2525, July 2020.

145 ÖZDOGAN, Ö.; BJÖRNSON, E.; LARSSON, E. G. Intelligent reflecting surfaces: Physics, propagation, and pathloss modeling. **IEEE Wireless Commun. Lett**, IEEE, v. 9, n. 5, p. 581–585, Dec. 2019.

146 RAJATHEVA, N. et al. Scoring the terabit/s goal: Broadband connectivity in 6G. **arXiv preprint arXiv:2008.07220**, 2020.

147 TAHA, A.; ALRABEIAH, M.; ALKHATEEB, A. **Enabling Large Intelligent Surfaces With Compressive Sensing and Deep Learning**. v. 9. [S.l.: s.n.], Mar. 2021. P. 44304–44321. DOI: 10.1109/ACCESS.2021.3064073.

148 HUANG, C. et al. Reconfigurable Intelligent Surfaces for Energy Efficiency in Wireless Communication. **IEEE Trans. Wireless Commun**, v. 18, n. 8, p. 4157–4170, June 2019.

149 GUO, H. et al. Dynamic Blockage Pre-Avoidance using Reconfigurable Intelligent Surfaces. **arXiv preprint arXiv:2201.06659**, 2022.

150 SOKAL, B. et al. IRS Phase-Shift Feedback Overhead-Aware Model Based on Rank-One Tensor Approximation. [Online]. Available: https://arxiv.org/pdf/2205.12024v1.pdf. [S.l.], 2022.